LITHOSPHERIC STRUCTURE OF THE ARABIAN PLATE AND SURROUNDING REGIONS

A Dissertation
Presented to the Faculty of the Graduate School
of Cornell University
in Partial Fulfillment of Requirement for the Degree of
Doctor of Philosophy

by
Khaled Sulaiman Al-Damegh
May 2004

LITHOSPHERIC STRUCTURE OF THE ARABIAN PLATE AND SURROUNDING REGIONS

Khaled Sulaiman Al-Damegh, Ph.D.

Cornell University 2004

Continuous waveform recording from a newly established broadband seismic network in Saudi Arabia, in addition to data produced by other stations in the region, were used to map regional seismic wave propagation (Lg and Sn) and Pn attenuation. Moreover, crustal thickness in the Arabian plate was also estimated based on receiver function analysis.

Zone blockage and inefficient Sn propagation is observed along and to the east of the Dead Sea fault system and in the northern portion of the Arabian plate (south of the Bitlis suture)., We observed Sn blockage across some segments of the Red Sea. These regions of high Sn attenuation have anomalously hot and possibly thin lithospheric mantle (i.e., mantle lid). Consistent with our Sn attenuation findings, we also observed low Qpn along the western portion of the Arabian plate and along the Dead Sea fault system. Our results imply the presence of a major anomalously hot and thinned lithosphere in these regions that may be caused by the extensive upper mantle anomaly that appears to span most of east Africa and western Arabia. These mapped zones of high attenuation closely coincide with an extensive Neogene and Quaternary volcanic activity.

We found that the average crustal thickness of the Arabian shield is 39 km. The crust thins to about 23 km along the Red Sea coast and to about 25 km along the Gulf of Aqaba. We observed a dramatic change in crustal thickness between the topographic escarpment of the Arabian shield and the shorelines of the Red Sea. We compared our results in the Arabian shield to nine other Proterozoic and Archean

shields that include reasonably well-determined Moho depths. We do not observe a significant difference between Proterozoic and Archean crustal thickness. Our observations show that the transition from oceanic to continental crust along the Red Sea margin occurs over a relatively short distance compared to a typical west Atlantic continental margin.

We argue that the anomalous nature of the Red Sea margin may be one of the consequences of the presence of a mega plume that extends from the core-mantle boundary into the upper mantle beneath east Africa, the Red Sea, and the western portion of the Arabian plate. In addition, the site where the sea-floor spreading of the Red Sea occurred was a Proterozoic suture and a zone of weakness. These observations combined may explain the relatively abrupt breakup of the Arabian plate and the anomalous nature of the Red Sea margin.

BIOGRAPHICAL SKETCH

Khaled Sulaiman Al-Damegh was born in September 24, 1968. He finished his Bachelor Degree in Science from King Fahd University for Petroleum and Minerals (Dhahran, Saudi Arabia) majoring in Geophysics. After graduation he joined the Institute of Astronomical and Geophysical Research at King Abdulaziz City for Science and Technology (KACST) in Riyadh. Khaled then received a scholarship to finish his Master degree from Texas A&M University and graduated with a master degree in Geophysics in 1996. He then joined the staff of the Saudi National Seismic Network as a researcher where he contributed to the development of the network. Showing a keen interest in learning more about seismology he was honored by a scholarship from KACST to finish his Ph.D. studies in the field at the Department of Earth and Atmospheric Sciences at Cornell University. Khaled joined the research group of Professor Muawia Barazangi and worked on the analysis of seismic data from SNSN.

To my parents, my wife, and all my family

ACKNOWLEDGMENTS

I would like to express my gratitude and thankfulness to my committee chair, Professor Muawia Barazangi, and to Professor Eric Sandovl for their extended support and generosity in the long hours and efforts in brining about this dissertation. I am thankful to my other committee members Professors Larry Brown and William Philpot for their assistance throughout my studies at Cornell University. This research is also the result of the generous exchange of information and ideas from instructors and colleagues at the Department of Earth and Atmospheric Sciences at Cornell University. My sincere gratitude to the many people I met throughout my stay here at Cornell University and in other places who contributed in one way or another to this research. In particular, I am thankful to Alex Calvert, Christine Orgren Sandvol, Dogan Seber, Steve Gallow, Francisco Gomez, Carrie Brindisi, George Hade, and Ali Al-Lazki. I would also like to thank King Abdulaziz City for Science and Technology for providing me with the scholarship to Cornell University. I also thank Dr. Mohammed Al-Suwaiyel and many others at KACST. This research has been partially supported by the National Science Foundation (Grants No. EAR-9804780 and EAR – 0106238 to Cornell University.).

TABLE OF CONTENTS

LIST OF TABLES

LIST OF FIGURS

CHAPTER ONE

REGIONAL SEISMIC WAVE PROPAGATION (Lg AND Sn) AND Pn ATTENUATION IN THE ARABIAN PLATE AND SURROUNDING REGIONS*

ABSTRACT

Continuous recordings of 17 broadband and short period digital seismic stations from a newly established seismological network in Saudi Arabia, along with digital recordings from the broadband stations of the GSN, MEDNET, GEOFON, a temporary array in Saudi Arabia, and a temporary short period stations in Oman, were analyzed to study the lithospheric structure of the Arabian plate and surrounding regions. The Arabian plate is surrounded by a variety of types of plate boundaries: continental collision (Zagros belt and Bitlis suture), continental transform (Dead Sea fault system), young sea floor spreading (Red Sea and Gulf of Aden), and oceanic transform (Owen fracture zone). Also, there are many intraplate Cenozoic processes such as volcanic eruptions, faulting, and folding that are taking place.

We used this massive waveform database of more than 6200 regional seismogram to map zones of blockage, inefficient, and efficient propagation of the Lg and Sn phases in the Middle East and East Africa. We observed Lg blockage across the Bitlis suture and Zagros fold and thrust belt, corresponding to the boundary between the Arabian and Eurasian plates. This is probably due to a major lateral change in the Lg crustal wave-guide. We also observed inefficient Lg propagation along the Oman mountains. Blockage and inefficient Sn propagation is observed along and for a considerable distance to the east of the Dead Sea fault system and in the northern portion of the Arabian plate (south of the Bitlis suture). These mapped

---

* Accepted for publication by Geophysical Journal International on January 12, 2004 as "Regional seismic propagation (Lg and Sn) and Pn attenuation in the Arabian Plate and surrounding regions" by Khaled Al-Damegh, Eric Sandvol, Ali Al-Lazki, and Muawia Barazangi.

zones of high Sn attenuation, moreover, closely coincide with extensive Neogene and Quaternary volcanic activity. We have also carefully mapped the boundaries of the Sn blockage within the Turkish and Iranian plateaus. Furthermore, we observed Sn blockage across the Owen fracture zone and across some segments of the Red Sea. These regions of high Sn attenuation most probably have anomalously hot and possibly thin lithospheric mantle (i.e., mantle lid). A surprising result is the efficient propagation of Sn across a segment of the Red Sea; an indication that active sea floor spreading is not continuous along the axis of the Red Sea. We also investigated the attenuation of Pn phase (Q_{Pn}) for 1-2 Hz along the Red Sea, Dead Sea fault system, within the Arabian shield, and in the Arabian platform. Consistent with the Sn attenuation, we observed low Q_{Pn} values of 22 and 15 along the western coast of the Arabian plate and along the Dead Sea fault system, respectively, for a frequency of 1.5 Hz. Higher Q_{Pn} values on the order of 400 were observed within the Arabian shield and platform for the same frequency. Our results based on Sn and Pn observations along the western and northern portions of the Arabian plate imply the presence of a major anomalously hot and thinned lithosphere in these regions that may be caused by the extensive upper mantle anomaly that appears to span most of east Africa and western Arabia.

INTRODUCTION

The Arabian plate is surrounded by diverse plate boundaries (Figure 1.1). To the southwest and south the Arabian plate is bounded by sea floor spreading along the Red Sea, the Gulf of Aden, and the Arabian Sea (McKenzie *et al.* 1970). To the east and north, the Arabian plate is colliding with the Eurasian plate along the Zagros and Bitlis sutures (McKenzie 1976). The Dead Sea fault system is located along the northwestern boundary of the plate. The fault is left-lateral with a minor component of rotation that results in the development of pull-apart basins, such as the Dead Sea rift basin (Garfunkel 1981). The interior of the plate is dominated by the late Proterozoic Arabian shield and the Arabian Phanerozoic platform. The platform is affected by numerous intraplate tectonism throughout the Mesozoic and Cenozoic time, such as the Palmyrides and Euphrates fault system within the northern part of the platform (Brew *et al.* 2001; Hempton 1987).

Though the surface geology of the Arabian plate and surrounding plate boundaries have been well studied, there are relatively few studies concerning the crustal and upper mantle structure of the Arabian plate. This study focuses on understanding the propagation characteristics of the regional seismic waves Pn, Pg, Sn and Lg. In particular, Lg is shown to be sensitive to lateral variations in the crustal thickness as well as the rheology of the crustal rocks. Sn, however, is very sensitive to lateral variations in the mantle lid and/or to the presence of asthenospheric material very close or immediately below the crust. Few studies are available in the literature concerning the propagation of Sn and Lg in the Middle East (Kadinsky-Cade *et al.* 1981; Rodgers *et al.* 1997; Mellors *et al.* 1999; Gok *et al.* 2000; Sandvol *et al.* 2001). This study, however, makes use of a massive new waveform database produced by the recently established broadband seismic array in Saudi Arabia. This database provided us with the opportunity to extend our study to the whole Arabian plate and the surrounding regions; i.e., this study is by far the most comprehensive and complete that can be accomplished at present.

Tectonic setting

The Arabian plate consists of a Precambrian shield bounded by a sedimentary platform (see Figure 1.1). The eastern part of the shield is overlapped unconformably by Phanerozoic sedimentary layers dipping eastward and reaching over 10 km in

Figure 1.1. A simplified tectonic map showing the main tectonic features of the Arabian plate and only surrounding regions. AP: Anatolian plateau; NAF: North Anatolian Fault; EAF: East Anatolian Fault; BS: Bitlis Suture; DSF: Dead Sea Fault; DND: Danakil Depression.

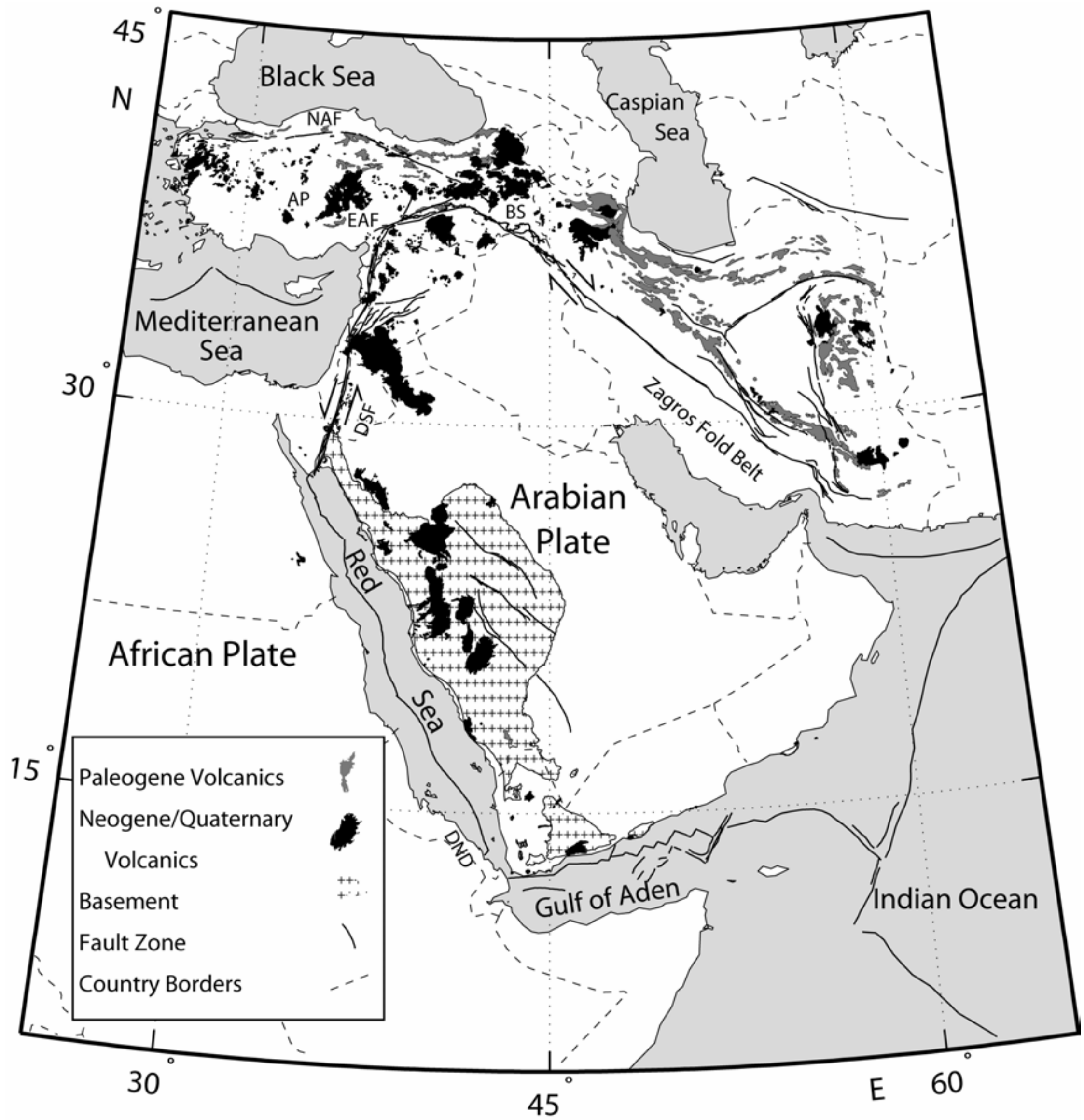

45°
N
Black Sea
Caspian Sea
NAF
AP
EAF
BS
Mediterranean Sea
30°
DSF
Zagros Fold Belt
Arabian Plate
Red Sea
African Plate
15°
DND
Gulf of Aden
Indian Ocean
Paleogene Volcanics
Neogene/Quaternary Volcanics
Basement
Fault Zone
Country Borders
30°
45°
E
60°

thickness (Powers *et al.* 1966; Sandvol *et al.* 1998; Mokhtar *et al.* 2001). The Arabian shield was part of the Nubian shield until the Oligocene, during which a rifting process started in Afar and later propagated eastward creating the Gulf of Aden and northward creating the Red Sea (Cochran and Martinez 1988). Assuming purely active rifting, some researchers argued that the crust of the Red Sea is oceanic and extending from the shorelines of Africa to Arabia (e.g. McKenzie *et al.* 1970; Le Pichon and Girdler 1988). Assuming purely passive rifting, on the other hand, other researchers argued that the Red Sea crust consists of extended 'transitional' continental crust (Cochran 1983). Neogene and Quaternary volcanics were observed along the western part of the Arabian plate (Camp and Roobol 1992).

Before the rifting of the Red Sea, the Afro-Arabian and the Eurasian plates were separated by the Neo-Tethys, which was being subducted under the Eurasian plate (Stocklin 1974). The Arabian plate collided with the Eurasian plate in the early Miocene (Dewey *et al.* 1973; Dewey and Sengor 1979). The Bitlis suture, the Zagros fold and thrust belt, and the East Anatolian left-lateral strike slip fault mark the collision zone (e.g. Sengor and Kidd 1979). North of the Bitlis suture and east of the Zagros lies the Iranian-Anatolian plateau. This plateau is a major topographic feature in the region, which was uplifted in Pliocene and characterized by pervasive late Tertiary-Quaternary basalts (Sengor and Kidd 1979). Recent GPS measurements over the Anatolian block (Barka and Reilinger 1997) show that the block is escaping to the west. Most of the Lesser and Greater Caucasus are believed to have formed within the same time frame of the Arabian-Eurasian collision during the middle to late Pliocene (e.g. Phillip *et al.* 1989).

The South Caspian Sea is a remnant Paleo-tethys lithosphere (Zonenshain and LePichon 1986). The crust of the Gulf of Oman is also believed to be oceanic and being subducted in a northerly direction beneath the Makran region (e.g. Farhoudi and Karig 1977; Jacob and Quittmeyer 1979).

The Mesopotamian foredeep, which is located to the west of the Zagros fold and thrust belt, consists of thick sediments that increase in thickness eastward (Seber *et al.* 1997). The Dead Sea fault system is a transcontinental boundary between the Arabian and African plates. It is considered a leaky left lateral transform fault with several portions of the fault system producing pull-apart basins such as the Dead Sea trough and the Gulf of Aqaba (Garfunkel 1981). Garfunkel (1981) suggested that spreading centers located in the middle of the pull-apart basins probably extend into the lithospheric mantle and are indicative of considerable lithospheric thinning.

Regional seismic waves Pn, Pg, Sn and Lg

Regional seismic phases have been essential in exploring regional crustal and mantle lid structure and rheology. Lg is a crustal guided wave that usually can be found within velocity and frequency windows of 3.1 to 3.6 km/sec and 0.5 to 5.0 Hz, respectively. The Lg phase has been modeled as higher-mode Love and Rayleigh waves and also as a sequence of wide angle multiply reflected S waves trapped in the crustal wave-guide (Bouchon 1982; Kennett 1986; Bostock and Kennett 1990). Observations of Lg propagation have demonstrated that Lg is blocked for paths in oceanic or very thin continental crust (Press and Ewing 1952; Searle 1975; Zhang and Lay 1995). Observational as well as theoretical studies indicate that the crustal wave-guide plays a primary role in Lg propagation characteristics (Kennett 1986; Bostock and Kennett 1990; Baumgardt and Der 1997; Rodgers *et al.*1997); rapid changes in the crustal thickness block or weaken Lg propagation (Bostock and Kennett 1990; Fan and Lay 1998; Mitchell *et al.* 1997); and Lg propagation can be severely weakened by deep sedimentary basins and intrinsic attenuation (e.g. Nuttli 1980; Baumgardt and

Der 1997). Recent Lg propagation studies utilize the Lg/Pg ratio to reflect changes in the ray path (e.g. Baumgardt 1996; Fan and Lay 1998; Hartse *et al.* 1998; Sandvol *et al.* 2001). Unlike the Lg phase, the Pg phase is reasonably insensitive to crustal structure. Consisting of direct P-wave energy from crustal earthquakes, the Pg seismic phase is usually found in a velocity window between 5.0 and 6.5 km/sec.

The Sn phase is a high-frequency guided seismic wave that travels in the lithospheric mantle with a typical frequency of 1 to 4 Hz or more. The typical velocity for Sn is around 4.7 km/sec in stable continental and oceanic lithosphere and less than that in more tectonically active regions (Huestis *et al.* 1973; Kadinsky-Cade *et al.* 1981). The Sn wave train can last up to 2 minutes and has been recorded for distances up to 35° (e.g. Molnar and Oliver 1969; Huestis *et al.* 1973). The first prominent phase on the seismic record for regional distances is Pn, a mantle lid guided wave with a velocity window of 7.8 to 8.1 km/sec.

Previous studies of regional waves in the Middle East have found a number of important regions of anomalous propagation characteristics. Kadinsky-Cade *et al.* (1982) found a zone of Lg blockage across the Zagros fold and thrust as well as a continuous zone of Sn attenuation extending from the northern Iranian plateau to central and western Turkey. Using more data from several broadband stations and the Iranian Long Period Array (ILPA), Rodger *et al.* (1997) extended these zones of Sn and Lg attenuation. They also found good correlation between Sn attenuating zones and the low Pn velocities published by Hearn and Ni (1994). An Sn and Lg tomography study by Sandvol *et al.* (2001) indicated that the South Caspian Sea crust is an oceanic lithosphere. In addition, that study outlined the main tectonic features such as the Zagros and Bitlis sutures, the Arabian shield, the Arabian platform, the Dead Sea fault system, and areas correlated with Neogene/Quaternary volcanics.

SEISMIC DATA

The data set used for this study is by far the most recent and complete one. This study integrated new data from more than 6 different networks, temporary stations, and a global permanent station (see Figure 1.2a). The main part of the data set came from the Saudi National Seismic Network (SNSN), which consists of 13 broadband stations and 4 short period one-component stations. Data from 4 temporary short period three component stations in Oman and data from the RAYN, an IRIS broadband permanent station, were also used. Data from two GEOSCOPE stations (ATD and AAE in Djibouti and Addis Ababa, respectively) were requested through IRIS and used in this study. In total more that 15000 regional seismograms were checked for quality of signal to noise, and electronic noise. Seismograms with low signal/noise ratio or electronic noise that can not be removed were discarded. Only regional earthquakes with distances between 175 km and 2000 km were used (see Figure 1.2b). Earthquakes with depth of more than 35 km were not used for the Lg/Pg analysis. In total about 2400 seismograms were found to be suitable for this study and were combined with the archived regional data set from the Cornell Middle East Project database.

QUALITATIVE EFFICIENCIES AND WAVEFORM EXAMPLES

For Lg observations, only seismograms with clear Pg phase arrival were used. Lg observations were classified according to the amplitude of the Lg phase relative to the Pg phase. When the Lg amplitude was approximately twice the Pg amplitude, the seismogram was classified as efficient. Seismograms were classified as inefficient when the relative amplitudes were approximately equal. In the case of Lg amplitudes smaller than Pg amplitudes, seismograms were classified as blocked or absent.

Figure 1.2. Maps showing the seismic stations (a) and earthquakes (b) used in this study**.**

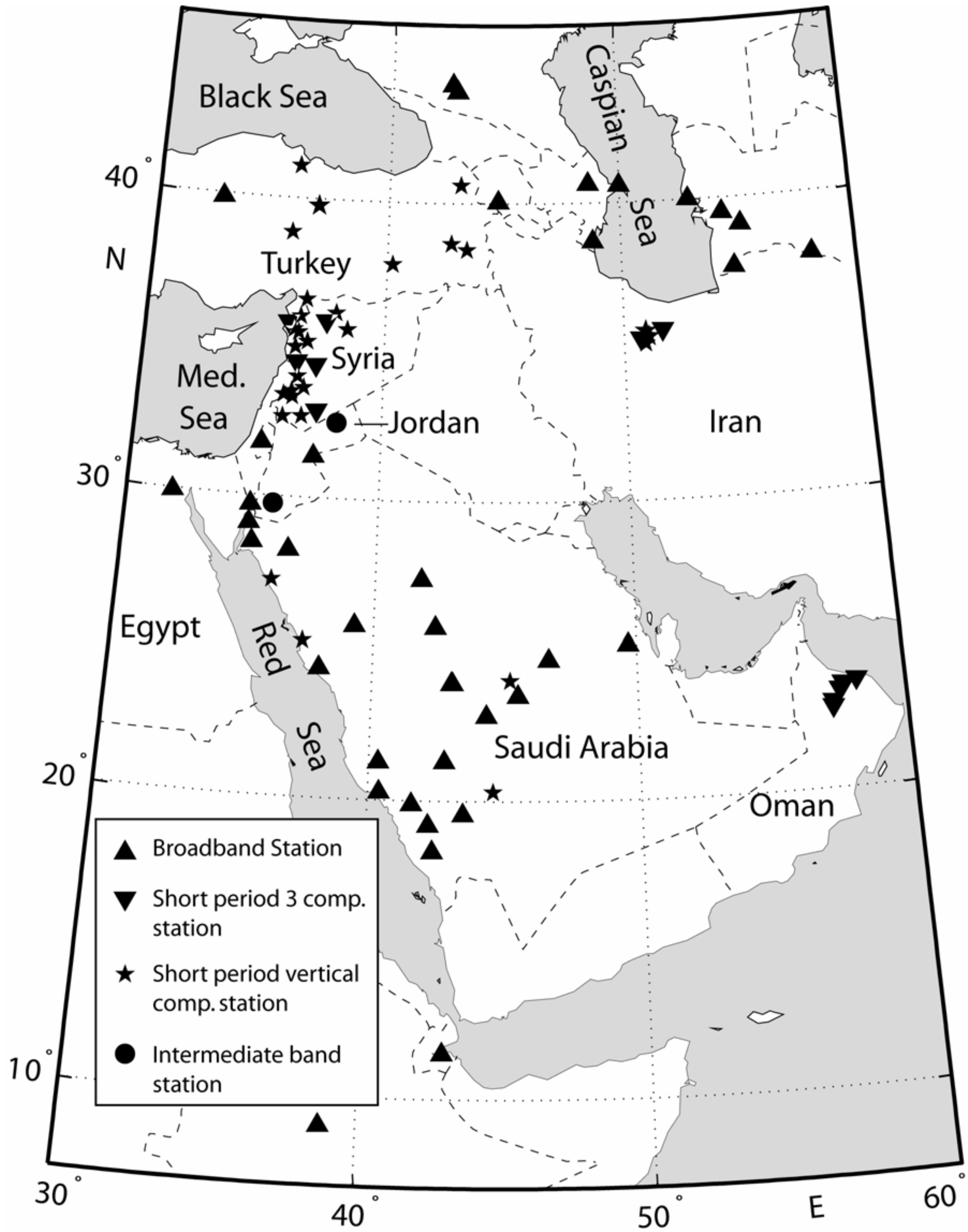
Black Sea
Caspian
Sea
40°
N
Turkey
Syria
Med.
Sea
Jordan
Iran
30°
Egypt
Red
Sea
Saudi Arabia
20°
Oman
Broadband Station
Short period 3 comp.
station
Short period vertical
comp. station
Intermediate band
station
10°
30°
40°
50°
E
60°

Figure 1.2. (continued)

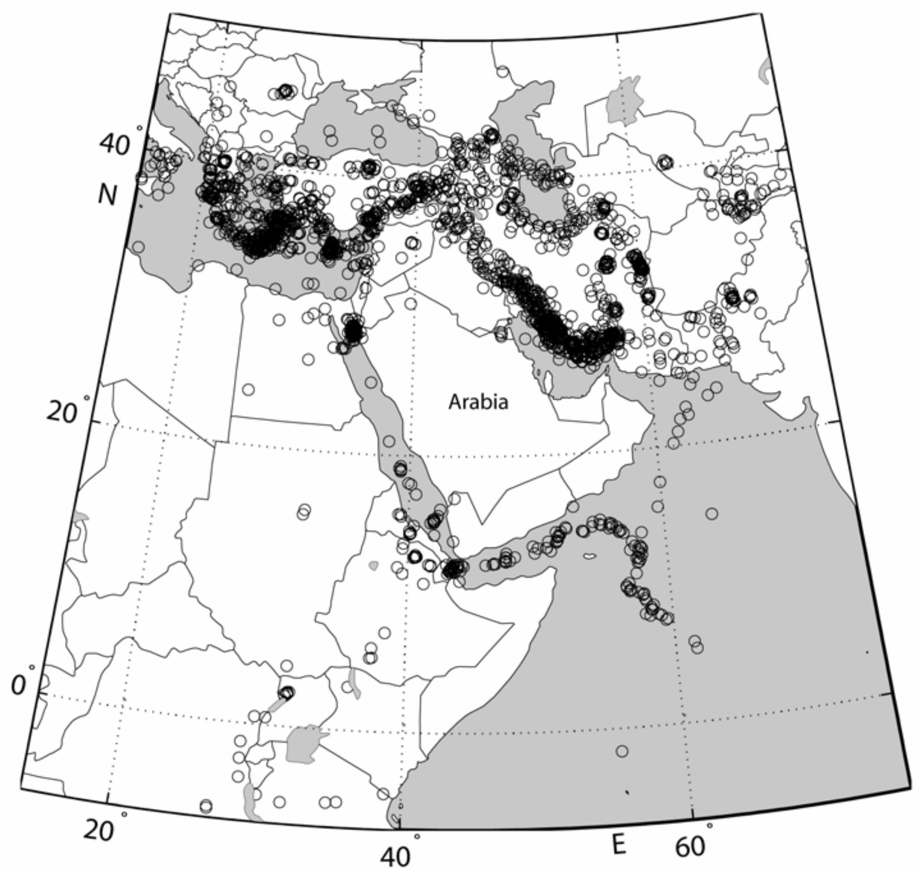

Figure 1.3. Map showing more than 6200 Lg ray path efficiencies. Each ray path corresponds to an earthquake-station pair. The seismograms corresponding to these rays were classified by visible inspection by the authors as efficient, inefficient, or blocked. The Arabian plate is well covered by mostly efficient Lg ray paths. Ray paths from Zagros to Oman stations are mostly inefficient. Fewer ray paths coverage is available across the Red Sea and Afar. Efficient as well as blocked and inefficient Lg ray paths were observed in the Red Sea region.

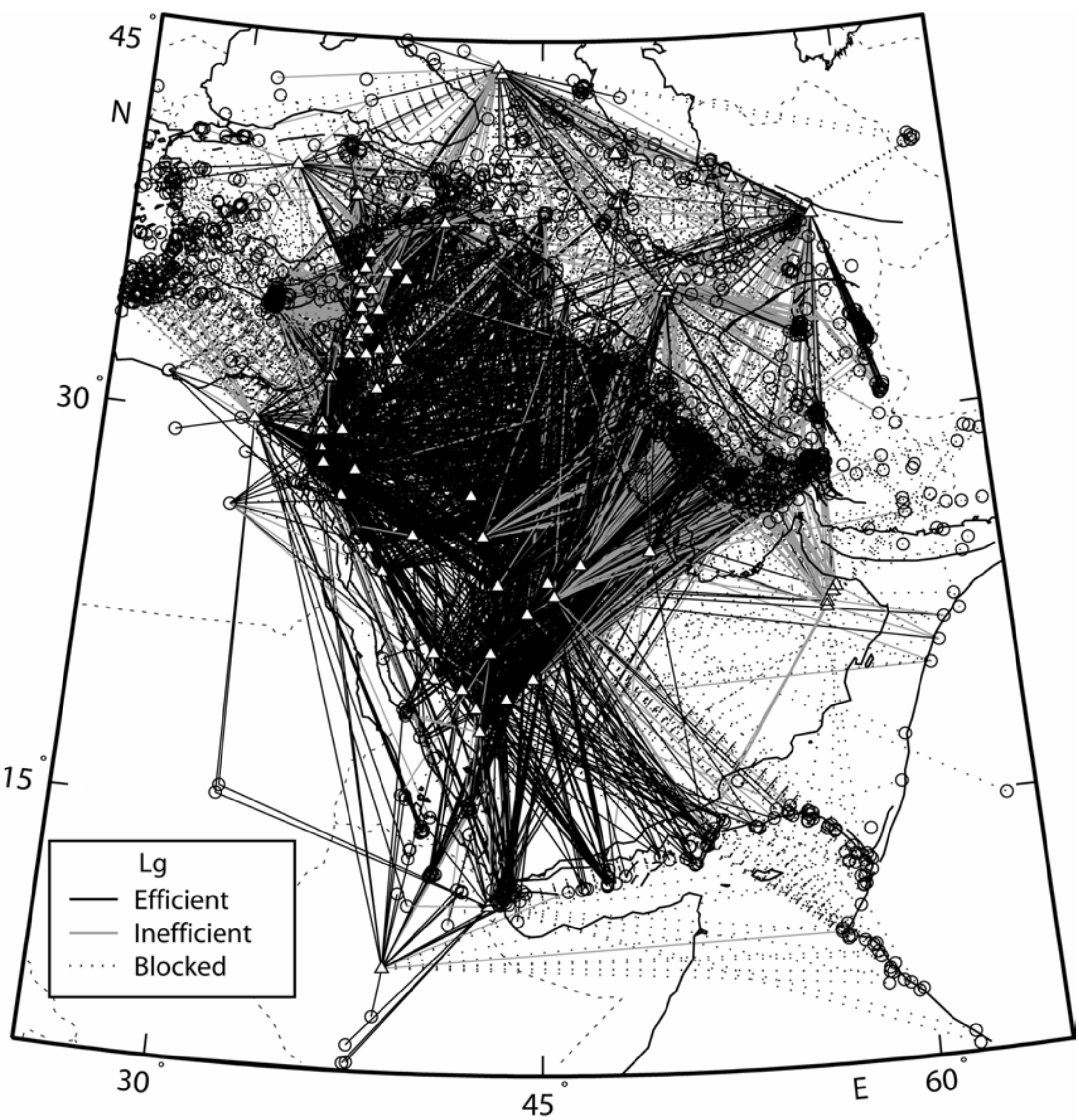
45°
N
30°
15°
30°
45°
E
60°
Lg
Efficient
Inefficient
Blocked

Figure 1.4. Map showing more than 6200 Sn ray paths efficiencies. Each ray path corresponds to an earthquake-station pair. The seismograms corresponding to these rays were classified by visible inspection by the authors as efficient, inefficient, or blocked. Inefficient and Sn blockage have been observed along the Dead Sea fault system, Iranian/Turkish plateau, Afar, and south of the Arabian plate. Efficient Sn propagation dominates within most of the Arabian plate. Efficient as well as blocked and inefficient Sn ray paths were observed across the Red Sea.

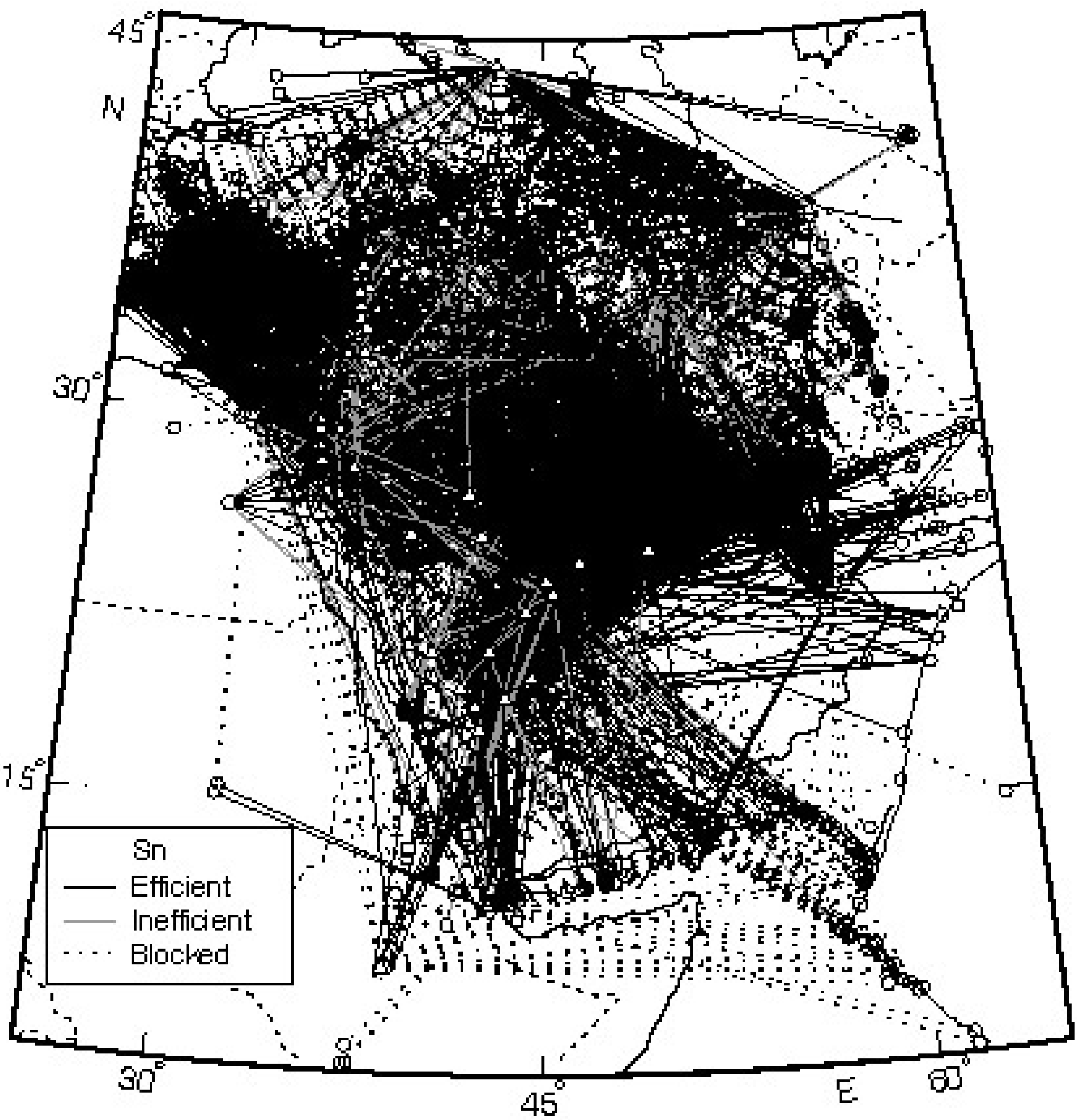

45°
N
30°
15°
30°
45°
E
60°
Sn
Efficient
Inefficient
Blocked

Clearly the above criteria are qualitative in nature, and for most ray paths considered in this study the details of the propagation of Pg does not significantly affect our observations. To avoid errors in timing and event mislocation, Lg and Pg windows were determined according to the picked first arrival. Crustal thickness and velocity do not influence this procedure. (Figure 1.3) is a ray map showing the classified Lg ray paths for all the data used in this study.

The Sn observations were classified into three groups: (1) efficient, (2) inefficient, and (3) blocked. We classified Sn, which arrives within a velocity window of 4.3 – 4.7 km/sec, as efficient if it contained high frequency (> 2 Hz) wave train and the average Sn amplitude is twice that of the average noise prior to the first arrival. An inefficient Sn lacks one or more features of efficient Sn. When no Sn signal is observed, the seismogram is classified as blocked. (Figure 1.4) shows all the classified Sn ray paths for all the data used in this study. We also show (Figures 1.3 and 1.4) in more details as an electronic supplemental figures for the paper and in Appendix A of the thesis (see Appendix A Figures A.1 and A.2).

Different filters were used to identify Sn, Lg, and Pg phases. Crustal velocities of 5.2 - 6.2km/sec for Pg, 4.1 - 4.6 km/sec for Sn, and 3.1 - 3.6 km/sec for Lg were assumed. Windows for Pg, Sn and Lg were determined based on first arrival picking and crustal thickness of 35 km.

Lg observations

Our Lg efficiency ray map is shown in Figure 1.3 and some examples from our data set are shown in (Figures 1.5 and 1.6). In our Lg ray map the Arabian plate is mostly well covered by Lg ray paths, except in the southeastern part. In general the Lg observations shown in Figure 1.3 are consistent, where most regions can be classified as regions of blockage, inefficient or efficient. For example, paths from earthquakes in the Zagros to stations in Saudi Arabia and Jordan show efficient Lg (Figure 1.6b-1, 2, 4, and 5). However, stations in Oman recorded inefficient Lg (Figure 1.6c. For earthquakes east of the Zagros to the same regions, Lg becomes mostly blocked or inefficient (Figure 1.6b-3 and 6, Figure 1.6c-3). Lg was mostly blocked (Figure 1.6a-5 and 6) for paths in the Mediterranean Sea. We observed very few earthquakes along and west of the Red Sea. Interestingly, for most of these events Lg was efficient and occasionally inefficient or blocked (Figure 1.5b-1, 2 and 3). Earthquakes along the Gulf of Aden show efficient Lg propagation along the Arabian plate (Figure 1.5c-1, and 2). Lg was blocked for earthquakes along Owen fracture zone. Few ray paths were observed in the African plate and were recorded at KEG, AAE, and ATD stations. The paths corresponding to these events show efficient Lg propagation (e.g. Figure 1.5b-5). In the Afar, Lg is generally efficient except when a path is mostly oceanic (Figure 1.5b-4, and 6).

Although we occasionally observed clear Sn to Lg converted phases, for example, Mediterranean Sea earthquakes recorded at HILS station in central Arabia, converted phases were not included in our study. Lg blockage was observed through eastern Turkey, the Anatolian plateau, the southern Black Sea, and across the Zagros thrust belts (Figure 1.3).

Sn observations

Our Sn efficiency ray map is shown in (Figure 1.4). Our Sn observations are dense except along the edges and in southeastern Arabia, where limited stations and ray paths were available. In general, our efficient, inefficient and blocked ray path observations were consistent over the efficiency map. We observed efficient Sn propagation in the Mediterranean and the Arabian platform (Figure 1.6a-5, 6 and Figure 1.6b-1, 2, 3, and 6). Efficient Sn propagation across the Red Sea was observed at some stations in Saudi Arabia (Figure 1.5a-1, 2, 3, and 4) as well as Sn blockage (Figure 1.5a-5 and Figure 1.5b-1, and 2). Our Sn observations in the northern part of the Red Sea (north of 24° latitude) have high frequency content (Figure 1.5a-3 and 4). Sn was blocked along the Afar depression, the Dead Sea fault system, and the Anatolian-Iranian plateau. Also, efficient Sn was observed across the Zagros (Figure 1.6b-3, 4, 5 and 6). We observed inefficient Sn propagation for paths crossing southern Yemen (Figure 1.5c-2). We have also observed a region of Sn attenuation between eastern Iraq to Jordan and northwestern Saudi Arabia (Figure 1.5c-4 and 6).

TOMOGRAPHIC IMAGING OF LG AND SN

Lg tomography

Lg/Pg amplitude ratio tomography method

The Lg/Pg ratio tomography method used in this study is based on Sandvol *et al.* (2001). This technique is an objective method to map regional phase attenuation. Also, by using the ratio method the values of the ratios are not discrete and therefore contain more information concerning the details of Lg attenuation relative to Pg.

Based on the derivation of Phillips *et al.* (2001) with slight modification, and the convolution model of Cong *et al.* (1996), the amplitude of a given phase as a function of frequency can be expressed by:

$$a_{ijk}(w) = a_{0i}(w)s_{jk}(w)c_{ik}(w)x^{(-\beta k)}{}_{ij}(w)\exp(-\alpha_k(w)x_{ij}), \qquad (1.1)$$

where i,j, and k are the event, station, and phase-type indices, respectively; a_{0i} is the total amplitude of the source; s_{jk} is the response of the station and site; c_{ik} is the partitioning of the amplitude into a particular phase-type; x_{ij} is the event-station separation; β_k is the spreading coefficient; and α_k is the attenuation factor. The natural log of the amplitude ratios of the two phases Lg and Pg (labeled 1 and 2) that follow the same path at a given frequency is:

$$\Delta A_{ij} = \Delta S_j + \Delta C_i - \Delta\beta\log(x_{ij}) - \Delta\alpha x_{ij}, , \quad (1.2)$$

where:

$\Delta A_{ij} = \log(a_{ij1} / a_{ij2})$; $\Delta S_j = \log(s_{j1} / s_{j2})$; $\Delta C_i = \log (C_{i1} / C_{i2})$; $\Delta\beta = (\beta_1-\beta_2)$; $\Delta\alpha = (\alpha_1 - \alpha_2)$.

Assuming the event-station separation x_{ij} to consist of a number of line segments x_{ijm} with a differential attenuation constants $\Delta\alpha_m$ the equation (2) can be rewritten as:

$$\Delta A_{ij} = \Delta S_j + \Delta C_i - \Delta\beta\log(x_{ij}) - \Sigma_m\Delta\alpha_m x_{ijm}, \quad (1.3)$$

To invert for the variables in eq. (1.3) two assumptions were made. First, the site and seismometer response to the two phases is absorbed in the ΔC term. Second, the relative ratio of the two phases is independent of the source size, depth, and location and thus ΔC is constant. For this study a 35 km cut off in depth for the Lg/Pg ratio tomography was applied to reduce the effect of the second assumption. Substituting

$\Delta\alpha_m = \Delta\underline{\alpha} + \Delta\alpha'_m \Delta\alpha,$

in eq. (1.3) where $\Delta\underline{\alpha}$ is the mean differential attenuation and $\Delta\alpha'_m$ is the perturbation in differential attenuation along ray segment m, Eq. (1.3) can be rewritten as:

$$\Delta A_{ij} = \Delta C - \Delta\beta\log(x_{ij}) - \Delta\underline{\alpha}\text{-}x_{ij} - \Sigma_m\Delta\alpha'_m x_{ijm}, \quad (1.4)$$

The distance dependence of Lg/Pg amplitude ratios have been accounted for in our study by the variable $\Delta\beta$. Figure 1.7 shows all the Lg/Pg amplitude ratios versus distance for all the data used in this study. Only weak distance dependence in our data set was found, primarily because of substantial blockage attenuation that both Lg and Pg undergo over the study area. By solving for ΔC, $\Delta\beta$, and $\Delta\underline{\alpha}$ using nonlinear curve fitting and applying these corrections, eq. (1.4) can be rewritten as:

$$\Delta A'_{ij} = \Delta A_{ij} - \Delta C - \Delta\beta\log(x_{ij}) + \Delta\underline{\alpha}x_{ij} = \Sigma_m\Delta\alpha'_m x_{ijm}, \quad (1.5)$$

Figure 1.5. Representative vertical seismograms from our data set used in this study and classified efficiencies. Earthquakes marked by (circles) and stations by (triangles). All wave forms were band passed from 0.5 to 5.0 Hz. Waveforms are numbered and labeled by station name, observed Lg and Sn efficiencies, $\log_{10}$ of (Lg amplitude/Pg amplitude), depth, and the distance from the station. Picked P_n is shown in solid line. The predicted Sn arrival time relative to the first arrival assuming a crustal thickness of 35 km and a crustal S velocity of 3.6 km/sec and a mantle S velocity of 4.5 km/sec is marked by the dotted line. Velocity windows of 5.2 – 6.2 km/sec for Pg and 3.1 – 3.6 km/sec for Lg are shown. (a) Rays crossing the Red Sea showing the diverse pattern in Sn and Lg efficiencies. (b) Rays along the Red Sea and across East Africa showing Sn blockage along the Red Sea and Gulf of Aden. Lg rays were efficient along the Red Sea. The travel time for these Lg phases correspond to direct ray path propagation. Lg blockage was observed along the Gulf of Aden. (c) Ray paths for an event in northern Iraq and in the Gulf of Aden at different stations within the Arabian plate. Inefficient and Sn blockage was observed in a region southeast of Syria and northwest of Jordan, and west of Yemen. Inefficient Lg was observed along the Mesopotamian fordeep.

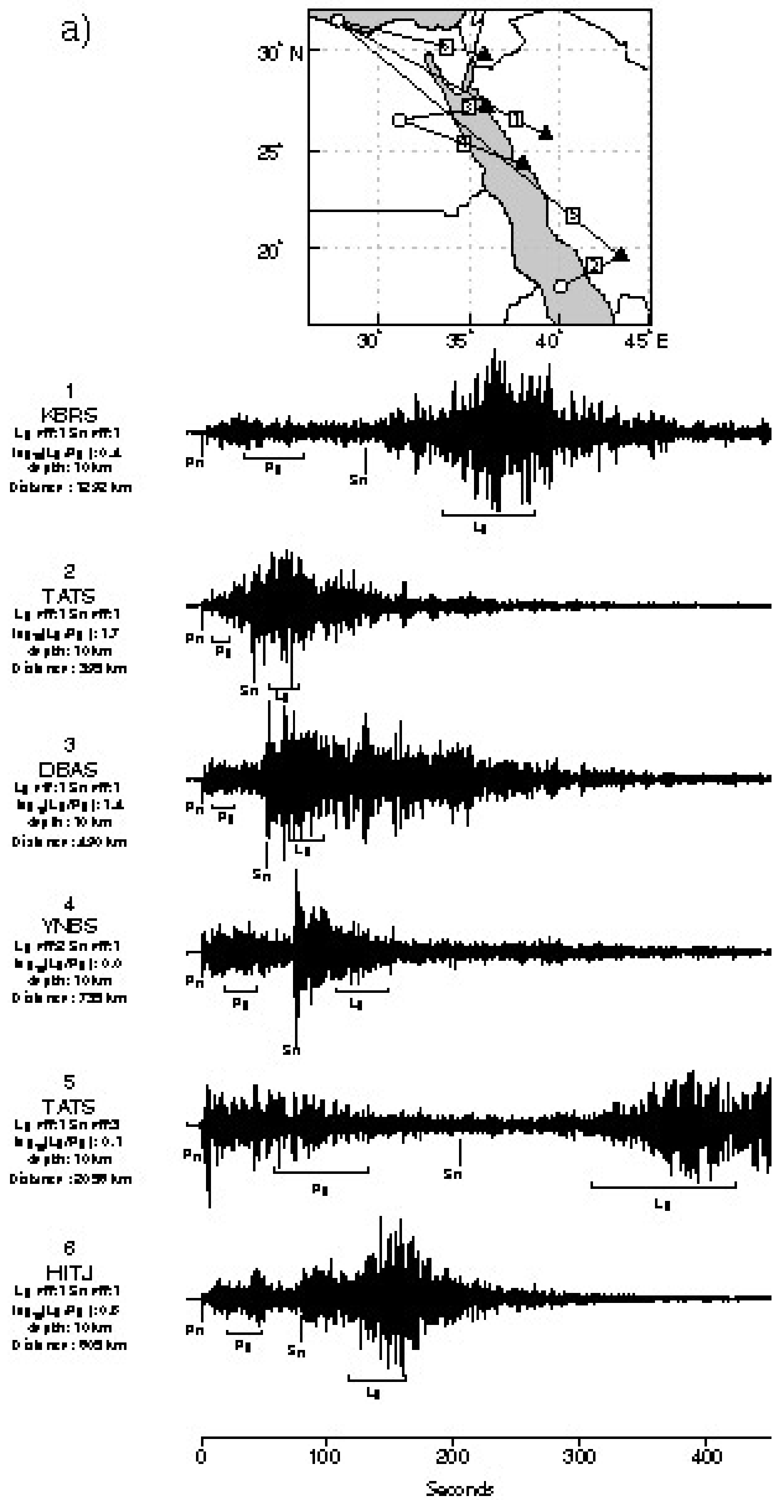
a)
30° N
25°
20°
30°
35°
40°
45° E
1
KBRS
2
TATS
3
DBAS
4
YNBS
5
TATS
6
HITJ
Pn
Pg
Sn
Lg
0
100
200
300
400
Seconds

Figure 1.5. (continued)

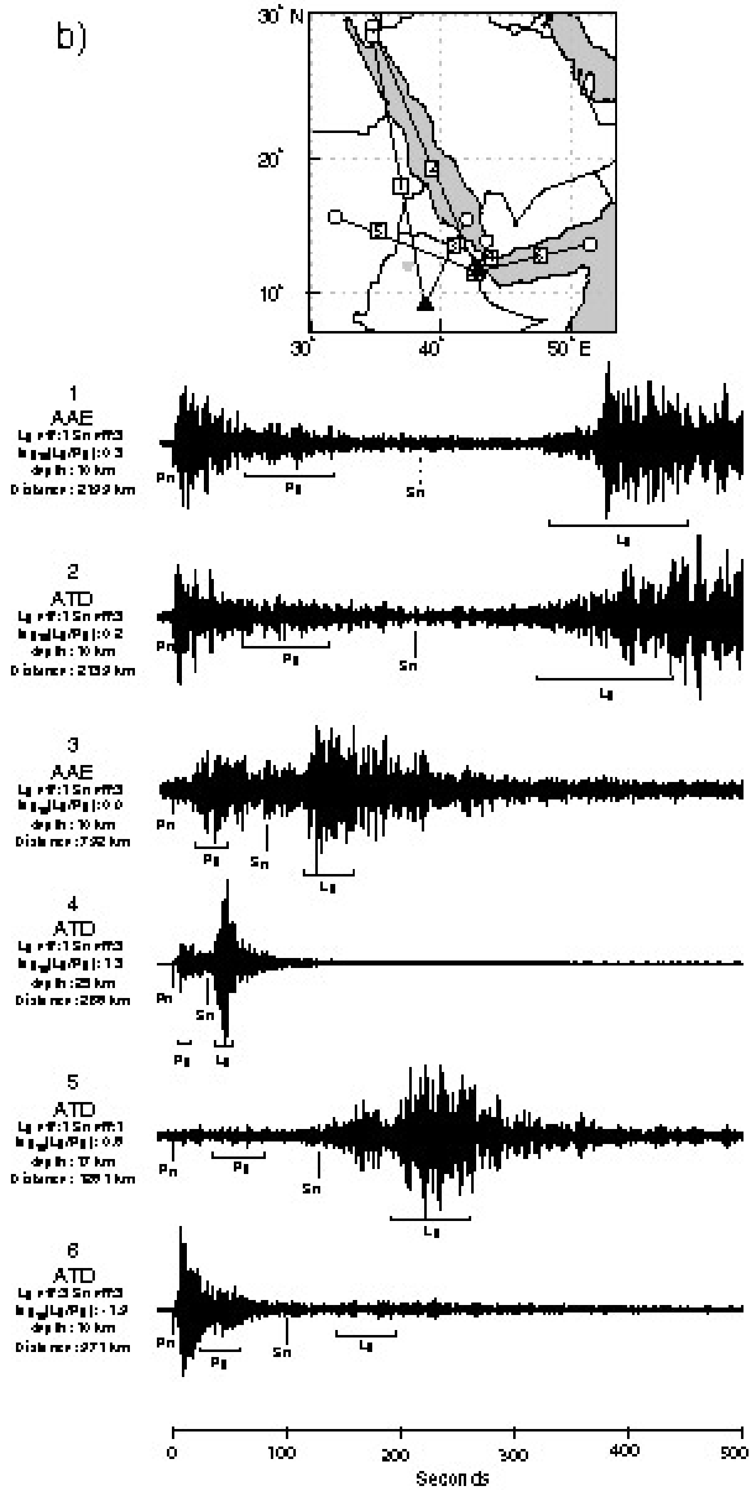

Figure 1.5. (continued)

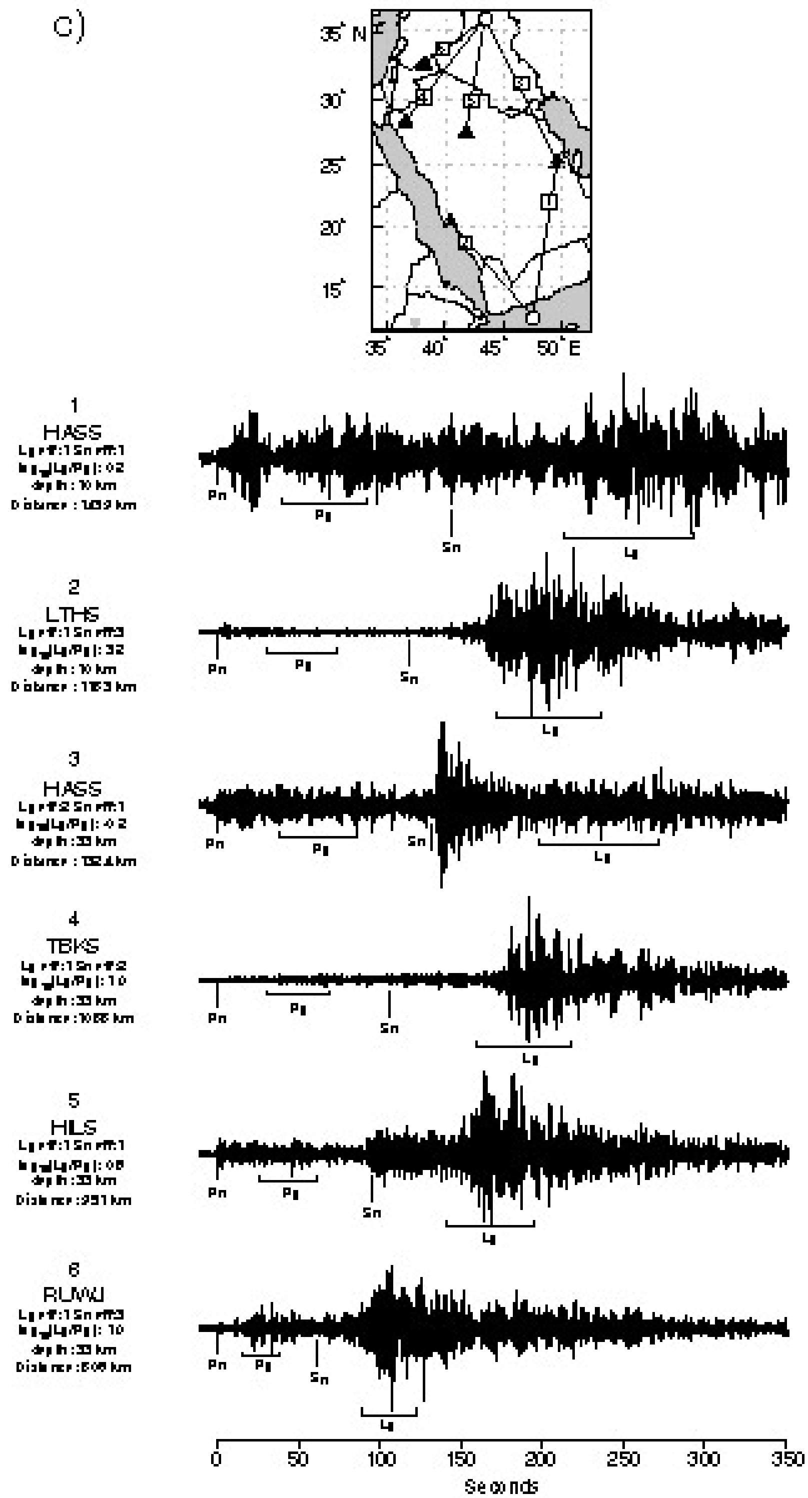

Figure 1.6. Representative vertical seismograms from our data set used in this study and classified efficiencies. Earthquakes marked by (circles) and stations by (triangles). All wave forms were band passed from 0.5 to 5.0 Hz. Waveforms are numbered and labeled by station name, observed Lg and Sn efficiencies, $\log_{10}$ of (Lg amplitude/Pg amplitude), depth, and the distance from the station. Picked P_n is shown in solid line. The predicted Sn arrival time relative to the first arrival assuming a crustal thickness of 35 km and a crustal S velocity of 3.6 km/sec and a mantle S velocity of 4.5 km/sec is marked by the dotted line. Velocity windows of 5.2 – 6.2 km/sec for Pg and 3.1 – 3.6 km/sec for Lg are shown. (a) Inefficient Lg was observed in the Mediterranean Sea. Efficient Lg was observed for ray paths from Zagros crossing Iraq. Low frequency efficient Sn was observed in eastern Jordan. (b) Efficient Sn and Lg paths from Zagros to Jordan and Saudi stations. Lg blockage was observed for paths crossing Zagros. (c) Lg was mostly blocked or attenuated at Oman stations, however, efficient Sn was observed at the same stations.

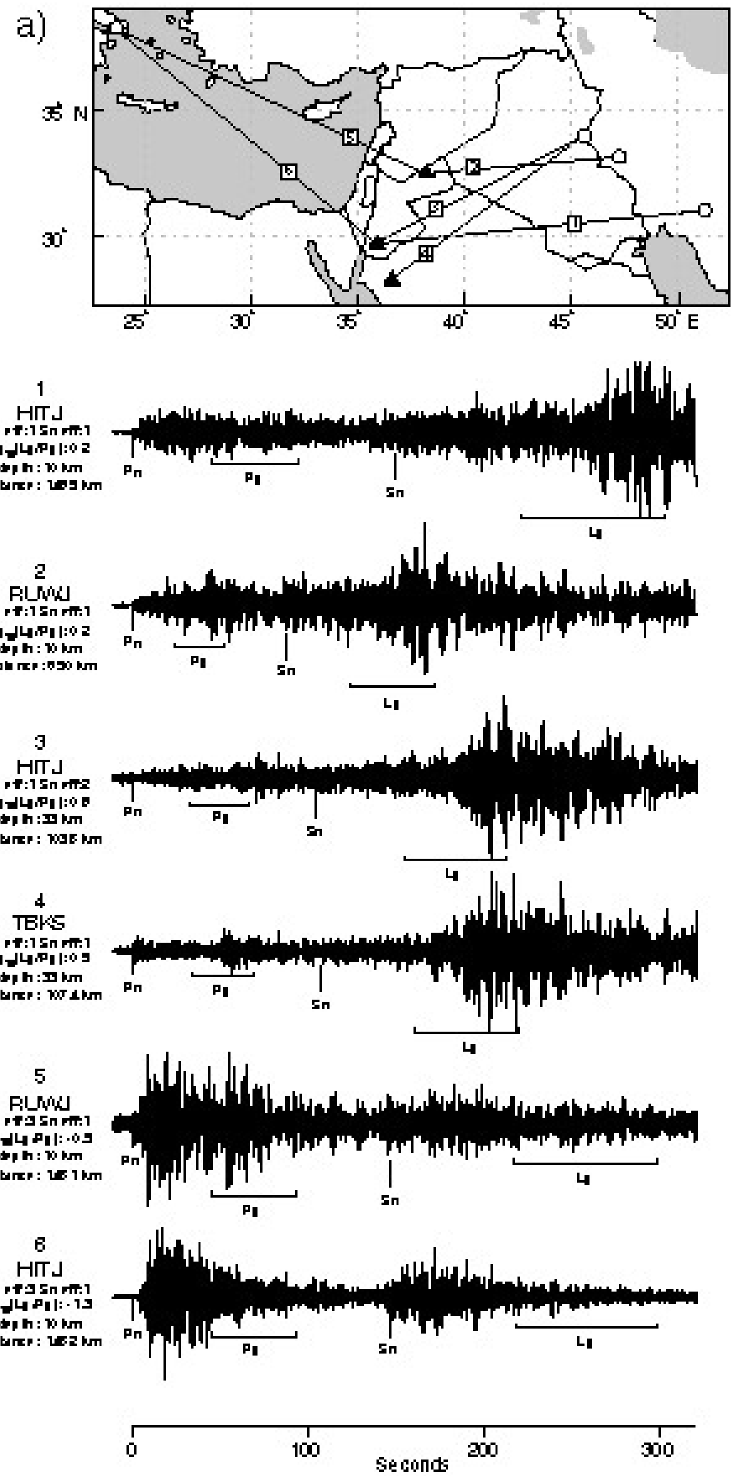
a)
35° N
30°
25°
30°
35°
40°
45°
50° E
1
HITJ
2
RUWJ
3
HITJ
4
TBKS
5
RUWJ
6
HITJ
Pn
Pg
Sn
Lg
0
100
200
300
Seconds

Figure 1.6. (continued)

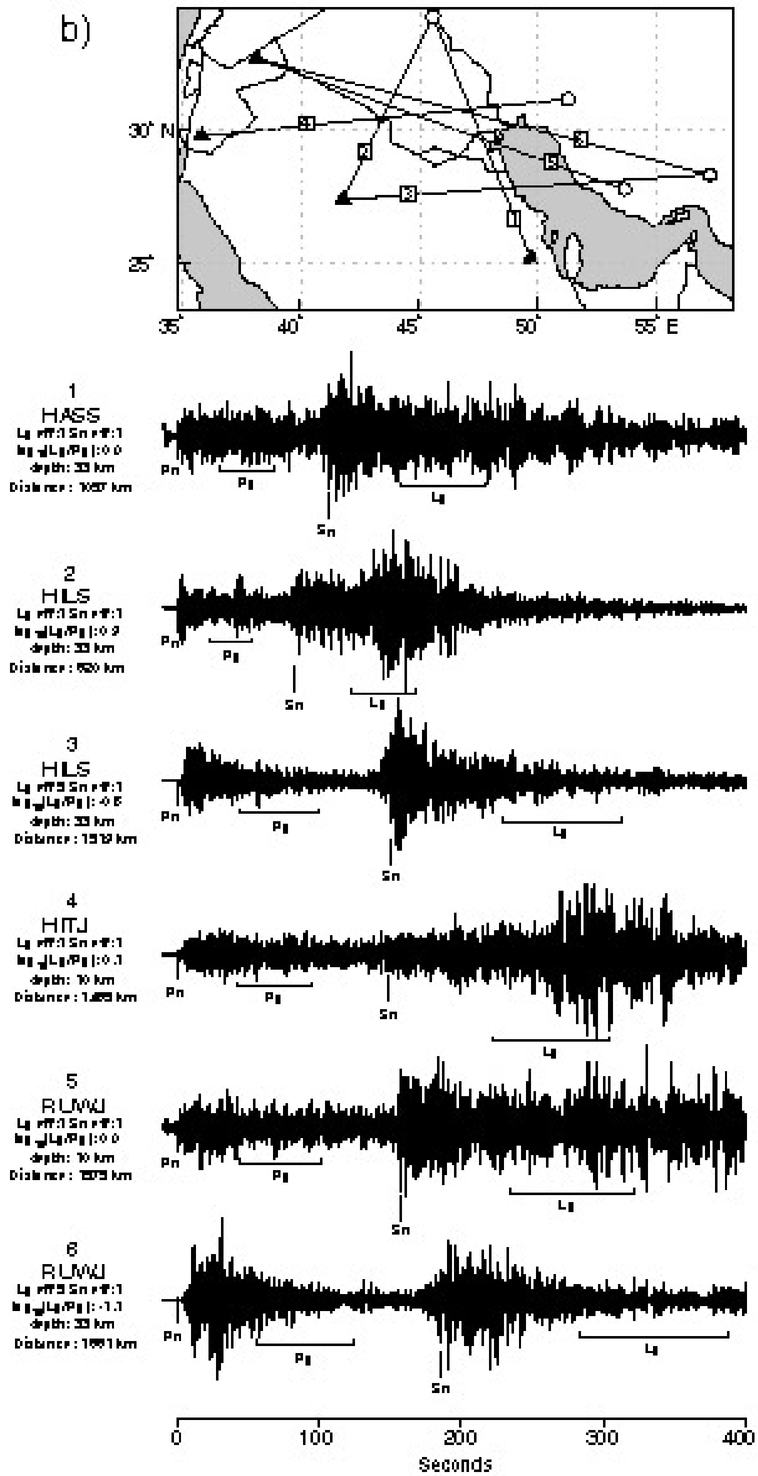

Figure 1.6. (continued)

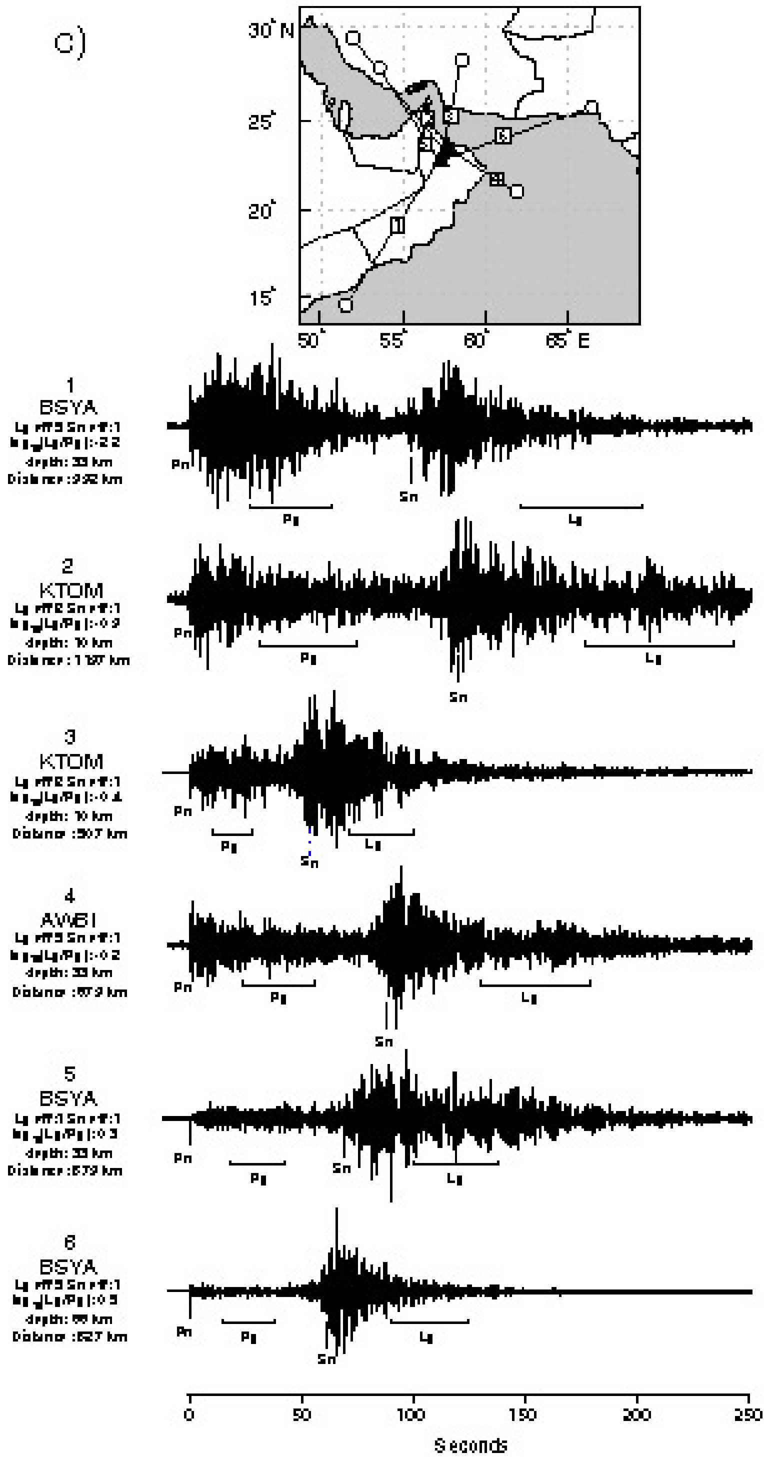

where $\Delta A'_{ij}$ is the corrected log amplitude ratio. Based on eq. (5) we applied a linear tomographic inversion for the corrected amplitude ratios to determine the lateral variation in $\Delta\alpha'_m$. The programs for solving the inversion were originally written for Pn velocity tomography by Hearn and Ni (1994) and modified by Sandvol *et al.* (2001) to solve for Lg/Pg ratio tomography. The equations were solved using the LSQR algorithm (Paige and Saunders 1982). The inversion steps are detailed in Calvert *et al.* (2000).

Results

Our Lg propagation relative to Pg for a cell size of 0.5° depicted in (Figure 1.8a) outlines areas where Lg is efficient, inefficient, or blocked. The model is dominated by regions of efficient and blocked Lg, buffered by regions of inefficient Lg. The main tectonic area where efficient Lg propagation is clearly observed is along the Arabian shield, consistent with other studies (e.g. Sandvol *et al.* 2001; Mellors *et al.* 1999; Cong and Mitchell 1998). In general, Lg is less efficient in the platform than in the shield. In our Lg/Pg model, Lg is efficient along the DSFS and in Jordan, Syria and Iraq. An inefficient Lg region was observed in Oman. West of the Arabian shield and across the Red Sea we observed another Lg efficient zone spreading from southern Egypt to northern Ethiopia and connected to the Arabian shield across the Red Sea. Two main regions of inefficient Lg propagation can be identified in the Red Sea. The first one is along the northwestern shoreline of the Red Sea, and the second one is in the southwestern part of the Red Sea along the Danakil depression. This anomaly is connected to the Afar depression and Gulf of Aden. Southwest of Afar efficient Lg propagation was observed. In general, we observed Lg/Pg blockage across the Mediterranean, Turkish and Iranian plateaus, the Zagros thrust belt, south of the Caspian Sea, Makran, and in the Gulf of Oman. These constitute a continuous region of Lg attenuation. Lg was efficient in the northern part of the Caspian Sea.

SN PROPAGATION EFFICIENCY TOMOGRAPHY

Method

In mapping the Sn propagation, we were required to use a modified version of the amplitude ratio tomography due to the fundamental difference in Sn propagation in continental and oceanic lithosphere. Amplitude ratios of the Sn phase to Pn, Pg or the whole P window were less successful in mapping variation in lithospheric attenuation structure than the Sn efficiency tomography (Rodger *et al.* 1997; Calvert *et al.* 2000). Our Sn efficiency tomography is based on our qualitative observations mentioned in section 3.2. The tomography method uses a modified version of eq. 4 above with the main assumption that phase 1 is the observed Sn amplitude and phase 2 is the Sn amplitude that would be observed if there was a constant attenuation factor of α_2 along the path. In essence, by categorizing the phases into qualitative bins, we are attempting to correct for ΔS_j, ΔC_i, and $\Delta\beta$ terms, which lead to the following equation:

$$\Delta A_{ij} = \log(a_{ij1}/a_{ij2}) = \Sigma_m(\alpha_2 - \alpha_{1m})x_{ijm} = \Sigma_m\alpha_m x_{ijm} \quad (1.6)$$

If we assume α_2 to correspond to the attenuation for an efficient path, ΔA would be zero since Log (1) = 0. For a blocked paths of $\Delta A^{obs}{}_{ijblock}$, an arbitrary log amplitude ratio was assumed, as well as, a variable value $k\Delta A^{obs}{}_{ijblock}$ $[0 < k < 1]$ for the inefficient paths. If we normalize the model parameters by dividing by $\Delta A^{obs}{}_{ijblock}$ (eq. 7) the model parameter α_m would be independent of the choice of $A^{obs}{}_{ijblock}$.

$$\alpha_m{}^{norm} = (\alpha_m)/(\Delta A^{obs}{}_{ijblock}) \quad (1.7)$$

In general, k is a parameter by which the inefficient observation can be weighted more closely to efficient or blocked to get the best possible representation of the data. Since the inefficient paths are small in number compared to the efficient and blocked paths, the k parameter has small and limited impact on the resulting model. We have rigorously tested the effect of k on our model; the effect is largest in regions

Figure 1.7. (a) $\log_{10}$ of the Lg amplitude/Pg amplitude versus distance for each path in Figure 1.3. The line in panel (a) is the best fit for the logarithm of the distance. (b) Shows the residual after 12 iteration using a Laplacian damped LSQR algorithm. There is a reduction in the variance of Lg/Pg ratio using our tomographic model.

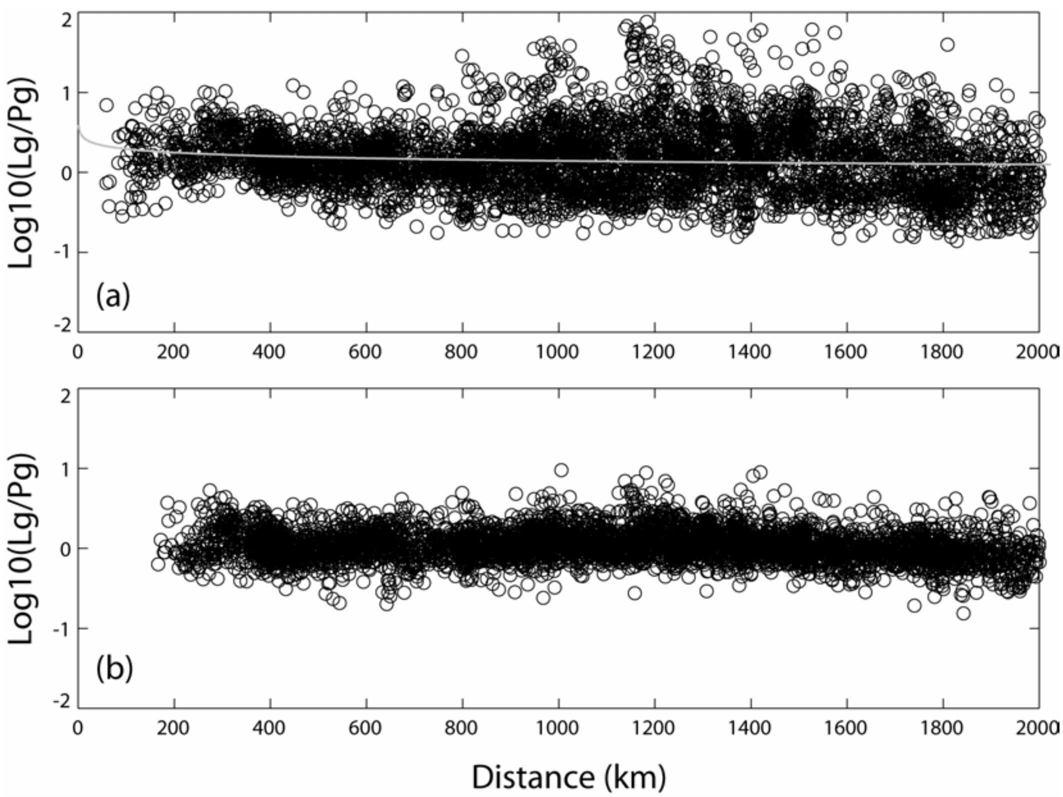

Log10(Lg/Pg)
(a)
Log10(Lg/Pg)
(b)
Distance (km)

Figure 1.8. Two maps showing our Lg/Pg ratio tomography and Sn tomography overlaid by the main faults and tectonic boundaries in the region. (a) Map showing the Lg/Pg ratio tomography for the Arabian plate and surrounding regions. Lg is efficient in the Arabian plate and some parts of the Red Sea. Lg blocked across Zagros, Turkish and Iranian plateaus, Mediterranean Sea, Gulf of Aden and Afar region. The southeastern part of the Arabian platform is dominated by a leakage in tomography due to blockage in the Arabian Sea (see Figure 1.3). (b) Map showing the Sn tomography for the same region. Inefficient Sn and blockage are mostly along the Dead Sea fault system and nearby regions, Turkish and Iranian plateaus, part of the Red Sea, eastern Yemen, Gulf of Aden and Afar region. The tomography also shows smaller regions of inefficient Sn in the margins of the Arabian shield. Sn is efficient in the Mediterranean Sea, Black Sea, and in Caspian Sea.

a)

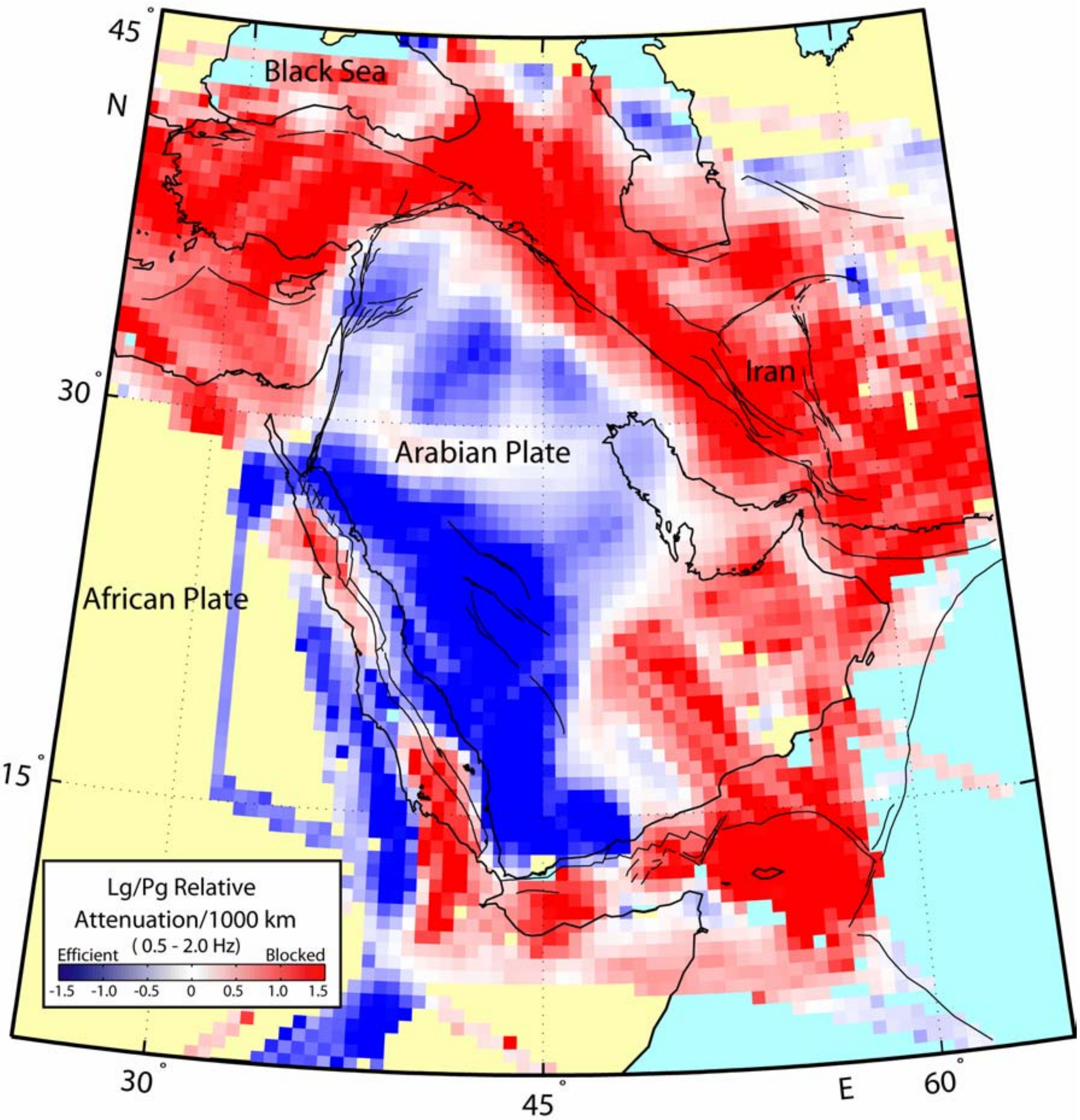
45°
N
30°
15°
30°
45°
E
60°
Black Sea
Iran
Arabian Plate
African Plate
Lg/Pg Relative
Attenuation/1000 km
(0.5 - 2.0 Hz)
Efficient
Blocked
-1.5 -1.0 -0.5 0 0.5 1.0 1.5

Figure 1.8. (continued)

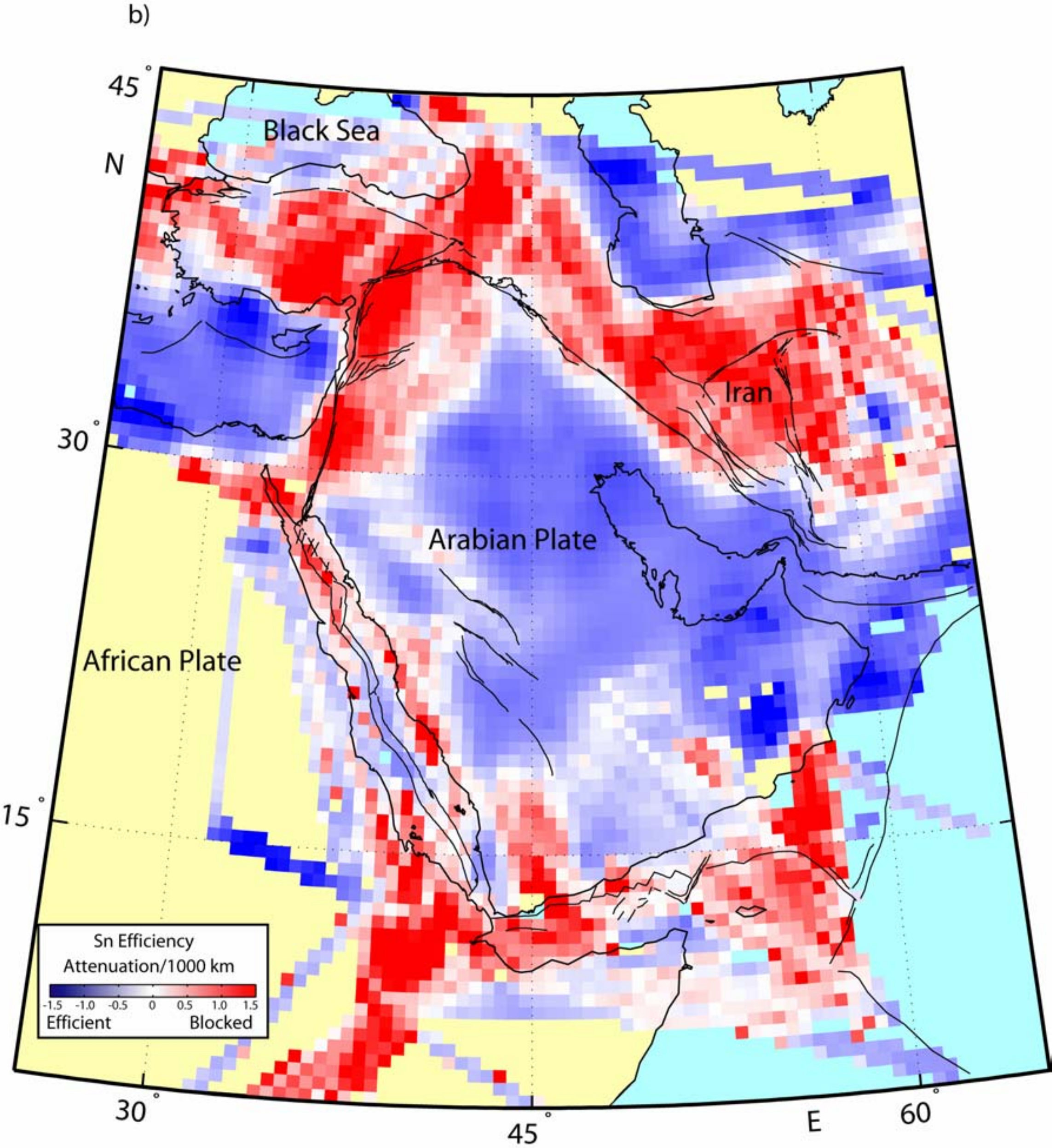

with poor ray coverage. In Figure 1.8b we have chosen a cell size of 0.5°, a k = 0.6, and a damping of 0.6 after several trials that for the sake of brevity have not been included.

Results

Sn propagation or blockage reflects the rheology of the mantle lid. At very short distances, however, the crustal legs of Sn may also affect Sn phase amplitude. The Sn tomography model presented in Figure 1.8b clearly corresponds to the major tectonic boundaries in the study region. Sn is inefficient or blocked along the Dead Sea fault system, Turkey, the Iranian plateau, the Arabian Sea, the Gulf of Aden, and the Afar depression. Sn is efficient, however, in the Mediterranean Sea, the southern part of the Caspian Sea, most of the Arabian platform, and most of the Arabian shield. Inefficient Sn propagation was observed in the northwestern part of the Arabian platform, for example in Syria, Jordan, and northwestern Iraq. Also, inefficient Sn propagation was observed in areas correlating well with Neogene/Quaternary volcanic activity in the Arabian shield. Along the Red Sea we observed a variable pattern of Sn efficiency. Regions of blocked or inefficient Sn were observed in the northern part, along the eastern coastlines, and between the Danakil depression and western coastlines of the Red Sea. Efficient Sn was observed across the central Red Sea.

Two continuous regions of high Sn attenuation were observed. The first region extends along the Afar depression and the Gulf of Aden leading to the Owen fracture zone. The second region is along the Dead Sea fault system, Turkey, and the Iranian plateau. In comparison to Lg propagation, Sn is efficient along the northern Zagros thrust belt down to the western part of Makran and the Gulf of Oman. The eastern edge of the Sn efficient zone correlates well with the mapped Zagros suture zone.

North of the Iranian plateau efficient Sn propagation was observed in Kopet Dagh, the Caspian Sea, and the northeastern part of the Caucasus mountains.

RESOLUTION AND UNCERTAINTIES

The distribution of stations and sources plays an important role in resolving the seismic characteristics of the ray paths in-between. A good ray path distribution is needed to accurately map propagation in a region. Unfortunately, control over the source and station distribution is fairly limited when passive seismic sources are used, resulting in variation of imaging quality over the imaged area. Two resolution tests have been applied to our tomography models, the synthetic checkerboard and spike tests. For the Lg/Pg ratio study we added Gaussian noise of ±15% of the maximum synthetic Lg/Pg ratio. We used the bootstrap resampling technique to further test the stability of our model. In this statistical analysis technique we simply resample our data until we reach the same number of observations as in our original inversion and then we invert the resampled data for a model. We repeated this process 100 times to draw a variance to detect any regions of the model that are dependant on only a few inconsistent observations (Hearn and Ni 1994).

Our Lg hit map, which shows the number of rays passing through each cell of our tomography, was shown as an electronic supplement for the paper and included in Appendix A of the thesis. The map shows cells of dense ray coverage and cells having limited or no ray coverage. In general, most regions covered by our Lg model are well covered except in the southeastern part of the Arabian platform and the Red Sea. We also performed the bootstrap test on our Lg/Pg data set following a method similar to that used by Sandvol et al. (2001) and Calvert et al. (2000). Our 2 σ bootstrap (see Appendix A) shows high uncertainty along the model edges, such as the Red Sea, the Gulf of Aden, Egypt, and eastern Iran. We also observed high uncertainty in Afar and in the southeastern part of the Arabian platform. Regions with high uncertainty mostly coincide with regions of limited ray coverage. The main goal of the checkerboard test is to point weaknesses in the model by generating synthetic efficiency data. In this procedure we divide the study area into squares of blockage and efficient areas in a pattern similar to a checkerboard (Figure 1.9). The initial checkerboard model for the Lg/Pg ratio study is shown in Figure 1.9 and our test model is shown in Figure 1.10. We used 5° X 5° checkerboard cells covering all the regions where ray paths were available. Our Lg/Pg checkerboard test results in Figure 1.10 show areas where ray paths were limited in number, for example ray coverage density is low, or confined to one direction. These two conditions resulted in smearing or a poor recovery of the original model. We observed leakage in areas lacking dense coverage (see Figure 1.9) such as the southeastern part of the Arabian platform, Afar, and along the Red Sea. We also observed smearing in regions where most ray paths were confined to one direction, such as the Arabian platform, Yemen, eastern Iran, Afar, and in the Mediterranean Sea. We observed good recovery in the Arabian shield, the Iranian plateau, Anatolia, the southern Caspian Sea, and in Syria. We performed similar tests on our Sn data set. Our Sn hit map (see Appendix A) shows limited ray coverage in the southeastern part of the Arabian platform and along the Red Sea. In our 2 σSn bootstrap results (see Appendix A) we observed regions with high uncertainty along the model edges, such as the Red Sea, the Gulf of Aden, Egypt, and eastern Iran. We also observed high uncertainty in Afar and in southeastern part of the Arabian platform. We performed the spike test on our Sn data set. Our initial spike test model is shown in Figure 1.11 and the test result is shown in Figure 1.12. We used 4° X 4° cells covering all the regions where ray paths were available. A 300 km blockage path length was assigned to our Sn test attenuation zones. We used the same ray paths used in our tomographic model to generate

Figure 1.9. Map showing the original checkerboard input used to generate the Lg/Pg synthetic ratios.

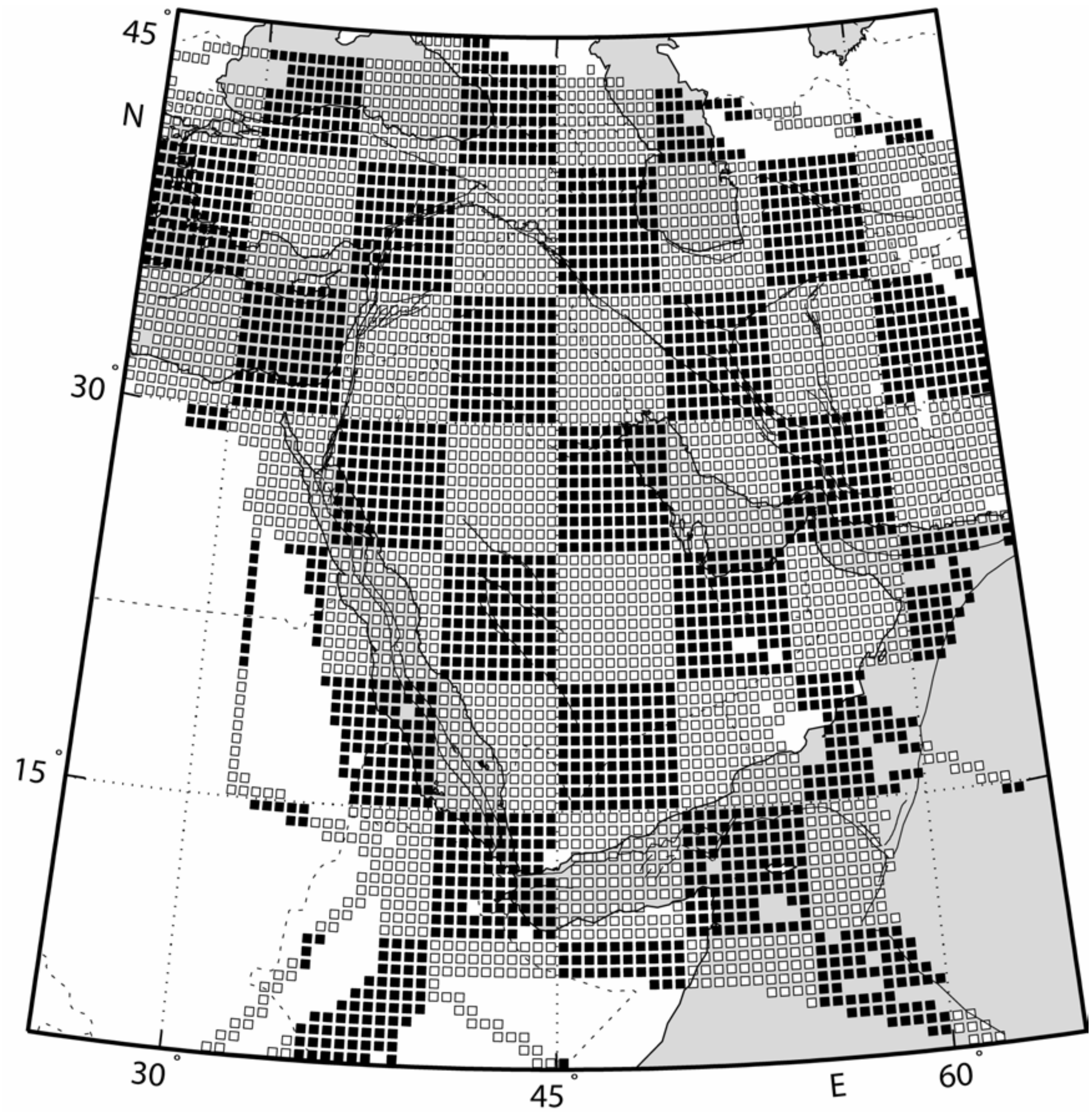
45°
N
30°
15°
30°
45°
E
60°

synthetic data. If a ray spent more than the blockage extension path length in a blockage area it was marked as blocked. Only efficient and blocked synthetics were generated. By switching 10% of the blocked to efficient and vice versa, we added noise to our synthetic test. Our Sn spike test results in Figure 1.12 shows regions of good recovery and poor recovery in our Sn model. We observed leakage in areas lacking dense coverage (see Figure 1.4) such as the southeastern part of the platform. We also observed smearing in regions where most ray paths were confined to one direction, such as Afar, the Gulf of Aden, the northern part of the Arabian shield, Yemen, eastern Iran, and the Mediterranean Sea. We observed good recovery in the Arabian platform, the Iranian plateau, Anatolia, the southern Caspian Sea, and in Syria.

PN ATTENUATION

Pn phase is a mantle lid guided wave and it is the first arriving phase when the distance between a station and an earthquake exceeds about 150 km in continental regions with a Moho depth of about 35 km. The velocity, amplitude, and frequency of the Pn phase depend on the rheology of the sampled path. The Reverse Two-Station Method (RTSM) (see inset in Figure 1.13) isolates the effect of upper mantle leg from the effect of the crustal leg and station response. In this study the attenuation factor Q_{pn} has been determined in four regions (see Figure 1.13). The RTSM has been used to estimate Q_{pn} in three different regions, namely Syria, eastern part of the Arabian shield, and western part of the Arabian shield. In the Arabian platform, where stations and azimuthal data coverage are limited, we used the simple Two-Station Method (TSM) (see inset in Figure 1.13).

Figure 1.10. The recovered checkerboard showing well-recovered regions and regions vulnerable for leakage or smearing in our Lg/Pg model. Smearing or leakage occurs due to limitation in the distribution of earthquakes and stations. Regions vulnerable for smearing are Zagros, Arabian platform, eastern Turkey, and the Mediterranean Sea. Regions vulnerable for leakage are Afar, southeastern Arabian platform. Well recover regions are Arabian shield, Iranian/Turkish plateau, and the northern Arabian platform.

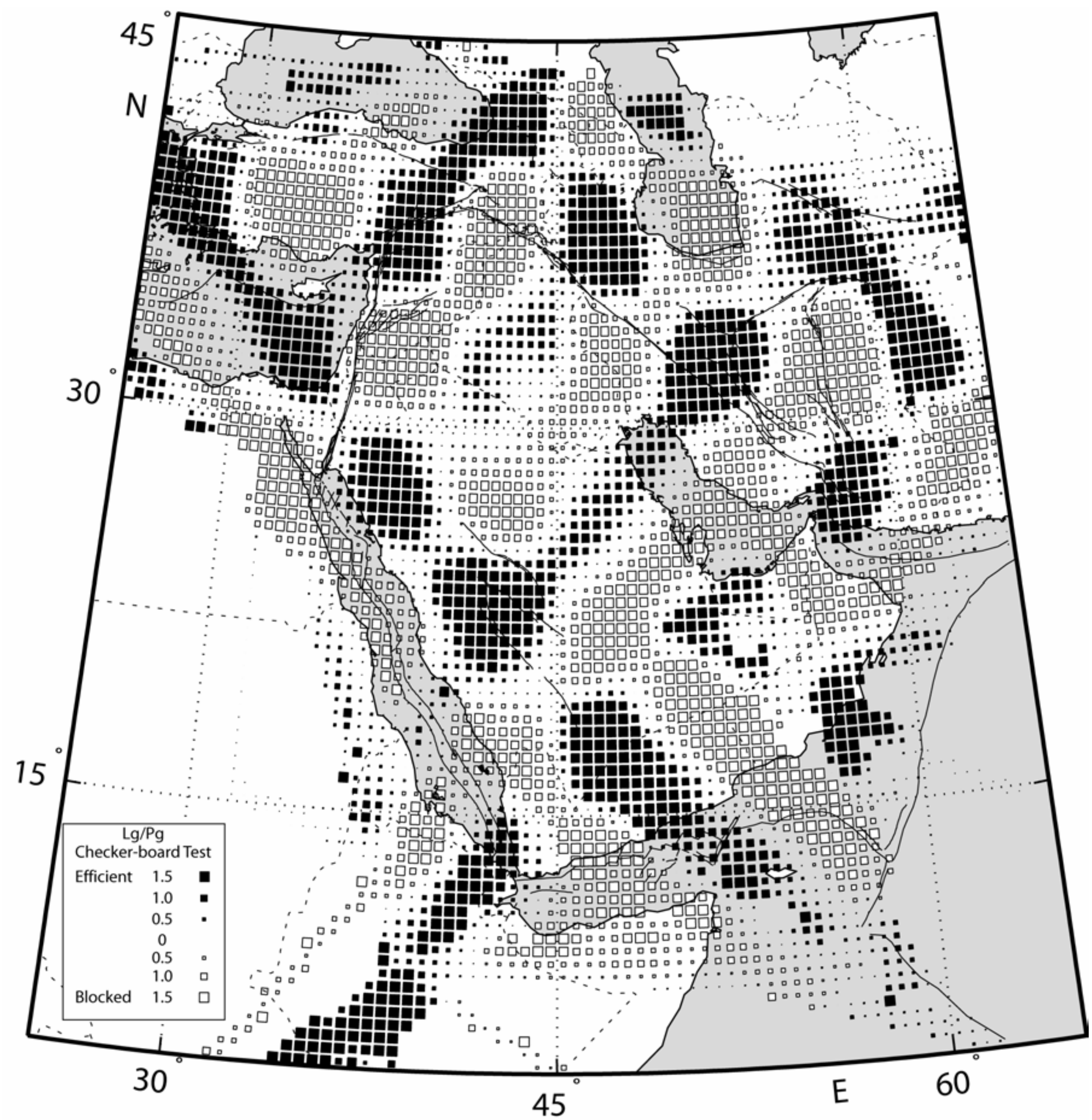
45°
N
30°
15°
30°
45°
E
60°
Lg/Pg
Checker-board Test
Efficient 1.5
1.0
0.5
0
0.5
1.0
Blocked 1.5

Figure 1.11. Map showing the original checkerboard input used to generate Sn synthetic efficiencies.

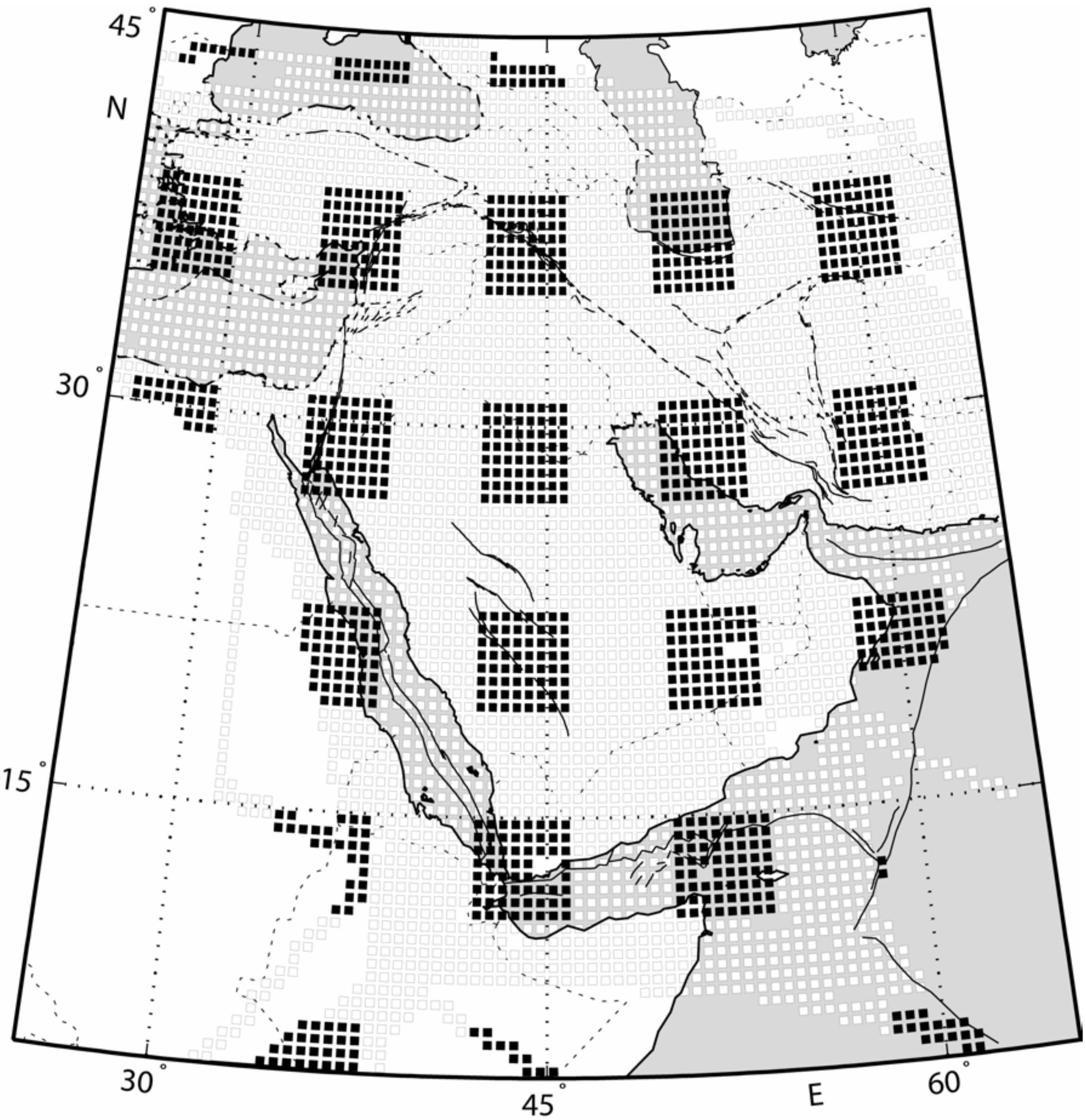

45°
N
30°
15°
30°
45°
E
60°

Figure 1.12. The Recovered checkerboard showing well-recovered regions and regions vulnerable for leakage or smearing in our Sn model. Regions vulnerable for smearing are south of the Arabian shield, and the Mediterranean Sea. Regions vulnerable for leakage are Afar, southeastern Arabian platform. Well-recovered regions are Zagros, Arabian platform, Turkish-Iranian plateau.

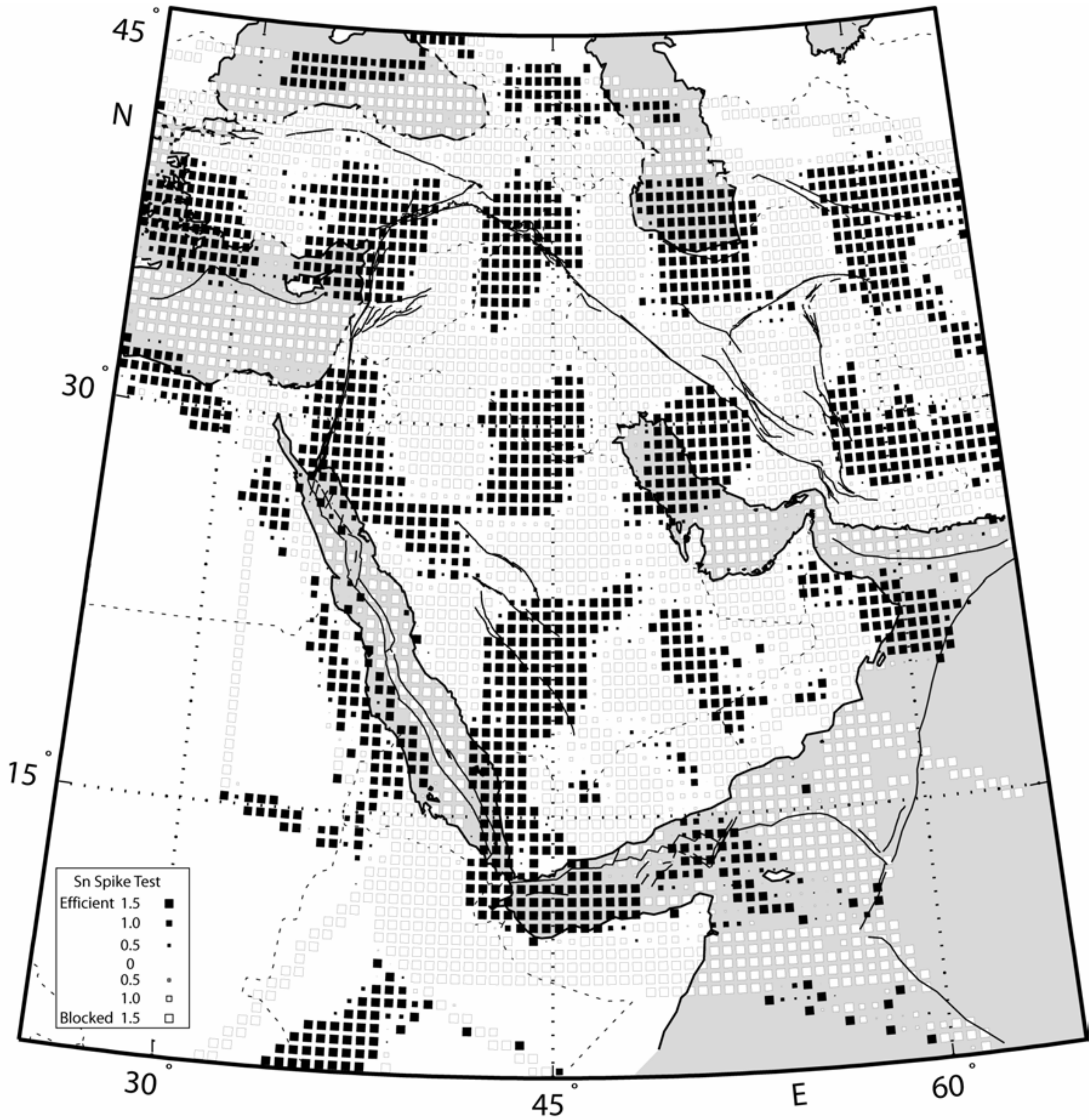

45°
N
30°
15°
30°
45°
E
60°
Sn Spike Test
Efficient 1.5
1.0
0.5
0
0.5
1.0
Blocked 1.5

The Reverse Two-Station Method

The RTSM was first introduced by Chun *et al.* (1986; 1987) to estimate Q_{Lg} for eastern Canada. The method was based on a pre-assumed value for the geometrical spreading rate coefficient. This assumption would jeopardize the accuracy of the results if the method were used to estimate Q_{pn} (Hill 1973; Sereno 1989). By developing a method to solve for the spreading rate coefficient and Q_{pn} simultaneously, Zhu *et al.* (1991) used the RTSM method to determine Q_{pn}. The method is based on the availability of four recordings of two earthquakes lining up with two stations, where the stations fall between the earthquakes (Zhu *et al.* 1991). To solve for Q_{pn} we used the following equation of Zhu *et al.* (1991):

$$\gamma(f) = \pi f / V_p\, Q_{pn}(f),$$

where γ is the attenuation coefficient, f is frequency, and V_p is the assumed velocity for Pn. We assumed a Pn velocity of 7.9 km/sec.

Data

The waveform data used to estimate Q_{Pn} were selected from the database for the Lg and Sn attenuation. The data were selected according to signal to noise ratio, alignment with two recording stations separated by a distance of more than 100 km, and the availability of another event corresponding to a reversed path. Also, we allowed a 6° or less azimuthal variance. The signal, which consists of 10 seconds of Pn window starting from the first arrival, and the noise, which consists of a 10 second window before the onset of the Pn, was cut after filtering and the ratio of the Root Mean Square (RMS) of the amplitudes was taken. The combination was used only when the RMS ratio of the signal to noise exceeded 2. We used a Multi Tapering Technique to estimate the power spectral density of the time series and in determining the Q_{pn} (Park 1987). To apply the RTSM, an earthquake in the opposite direction from the stations and satisfying the same above criteria is required. Figure 1.13 shows all the earthquake combinations used to estimate Q_{pn} values for this study. Figure 1.14 shows examples of Pn waveforms using the RTSM approach.

Results for Q_{pn}

The Q_{pn} values estimated using RTSM and TSM (Figure 1.15) were in good agreement with our Sn attenuation results. In the Arabian shield, the Q_{pn} values in the western part were lower than the Q_{pn} values in the eastern part, reflecting higher attenuation in the western part as was shown by the Sn tomography model. For example, for a frequency of 1.5 Hz, we observed Q_{pn} values of 22 and 465 for the western Arabian shield and the eastern Arabian shield, respectively. The Q_{pn} values of the Arabian platform were slightly lower than the Q_{pn} values of the eastern part of the shield. The lowest observed Q_{pn} values were in Syria, where Q_{pn} was 15 for a frequency of 1.5 Hz. This is also consistent with the low Pn velocity values reported by Al-Lazki *et al.* (2003) and our Sn attenuation model.

For the Arabian shield, our estimated Q_{pn} values are comparable to the Q_{pn} results for eastern Canada estimated by Zhu *et al.* (1991) using RTSM. For a frequency of 1.5 Hz the Q_{pn} value for eastern Canada was 269. Averaging our Q_{pn} values for the shield for the same frequency, we would obtain a Q_{pn} value of 244, which is comparably close to the Q_{pn} value in eastern Canada. Using the spectral amplitude ratio and pulse broadening techniques the Q_{pn} values determined by Badri and Sinno (1991) in the eastern Arabian Shield range from 475 to nearly 1560 for the frequency range between 2 and 12 Hz. Considering our frequency window (1 – 2 Hz) our Q_{pn} results for the eastern part of the shield are comparable with their Q_{pn} values.

Figure 1.13. Map showing all the earthquakes (circles) and stations (triangles) combinations used to estimate Q_{Pn} (attenuation factor). Q_{Pn} have been estimated along the lines connecting stations. In the inset, schematic cartoons show the Reverse Two Stations Method and the Two Stations Method used to estimate Q_{Pn}.

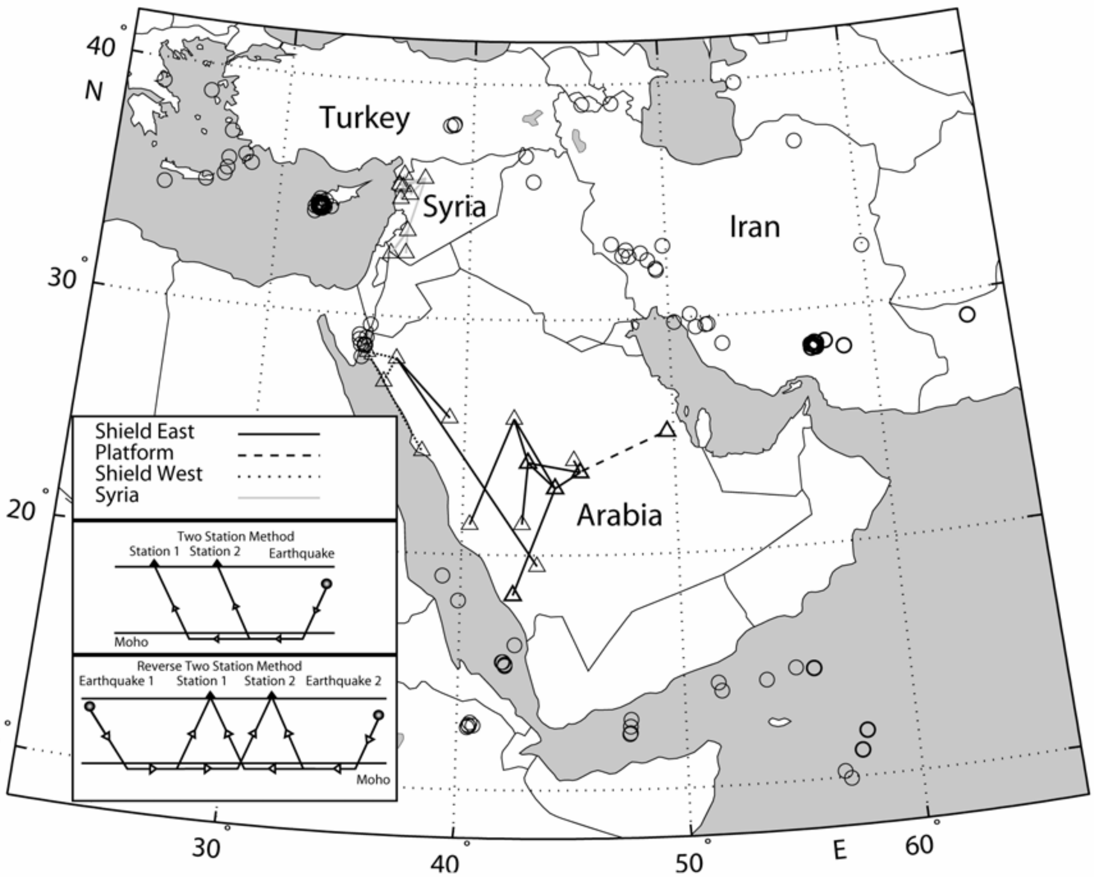

Turkey
Syria
Iran
Arabia
Shield East
Platform
Shield West
Syria
Two Station Method
Station 1
Station 2
Earthquake
Moho
Reverse Two Station Method
Earthquake 1
Station 1
Station 2
Earthquake 2
Moho
40°
N
30°
20°
10°
30°
40°
50°
E
60°

Figure 1.14. Sample seismograms (vertical component) used to estimate Q_{Pn} for the eastern part of the Arabian shield (see inset map for location).

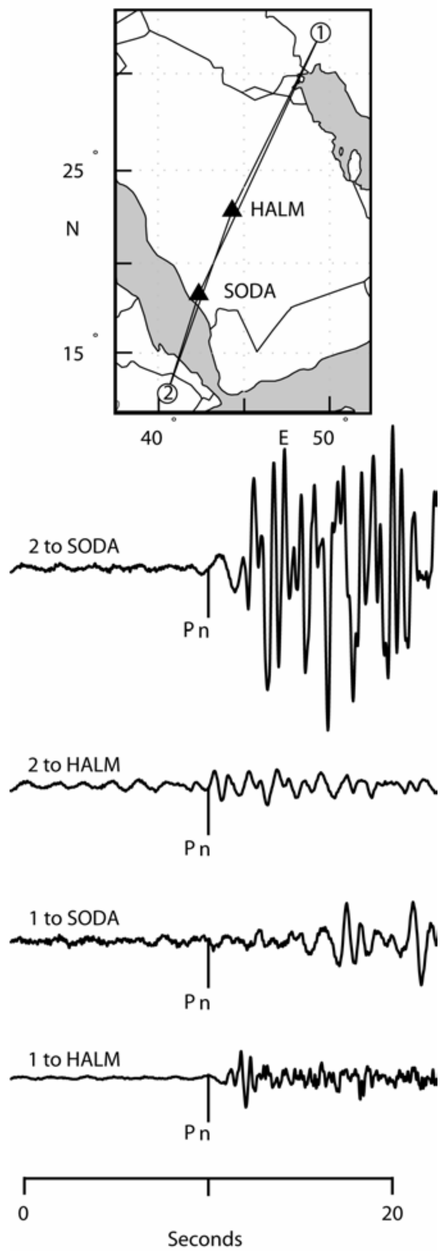

1
2
25°
N
15°
40°
E
50°
HALM
SODA
2 to SODA
Pn
2 to HALM
Pn
1 to SODA
Pn
1 to HALM
Pn
0
20
Seconds

Figure 1.15. Plot showing Q_{Pn} estimate versus frequency for western Arabian shield, eastern Arabian shield, Arabian platform, and in Syria.

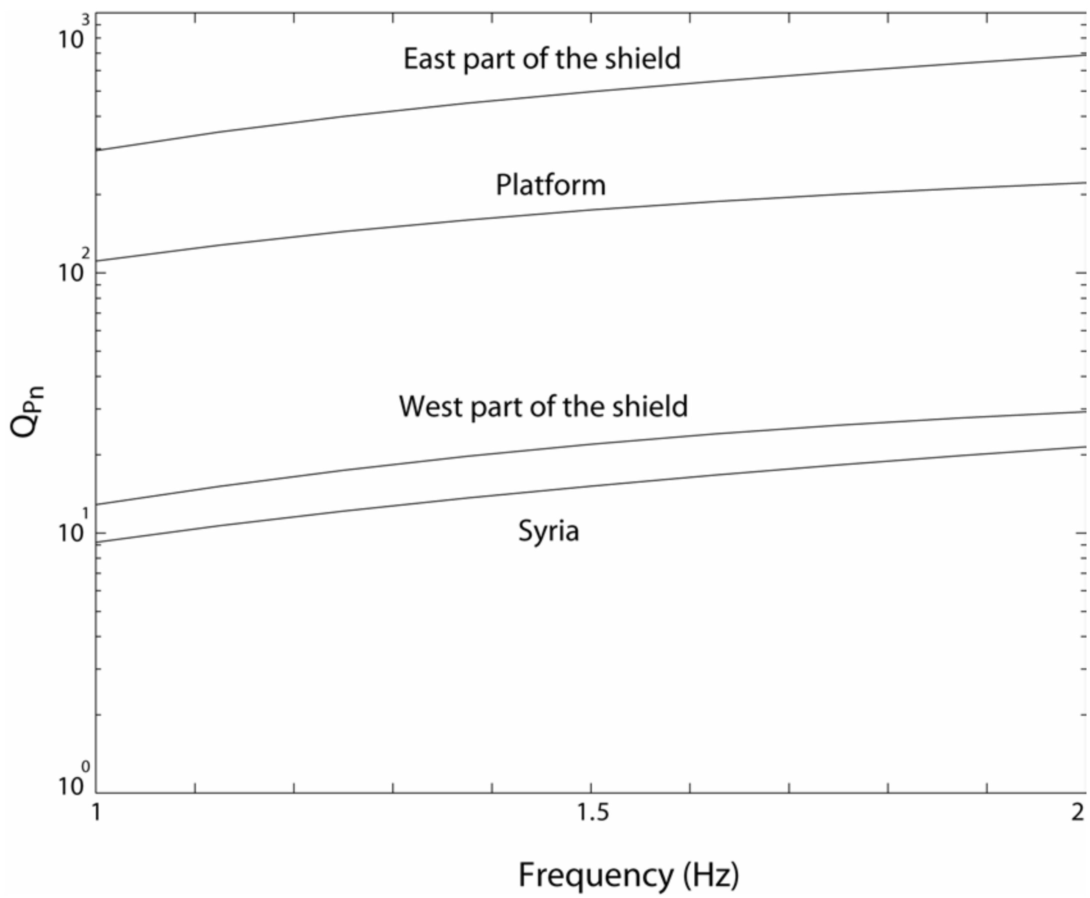

East part of the shield
Platform
West part of the shield
Syria
Q_{Pn}
10^3
10^2
10^1
10^0
1
1.5
2
Frequency (Hz)

DISCUSSION AND CONCLUSIONS

Using a large number of regional seismograms we have been able to map regional seismic wave (Lg and Sn) attenuation in the Arabian plate and the surrounding regions (Figures 1.8a, b). The results shown on Figure 1.8a, b represent the most comprehensive and complete mapping of Lg and Sn. The Lg seismic phase is a crustal guided wave sensitive to crustal thickness variations and/or intrinsic attenuation. In our Lg tomography model (Figure 1.8a), a distinctive Lg blockage zone extends from Makran, southeast of the Arabian plate, along the Zagros fold and thrust belt, to Anatolia bounding the Arabian plate from east to north. This blockage zone coincides well with the Arabian-Eurasian continent-continent collision, which is characterized by the uplift of the Zagros mountains and the Turkish-Iranian plateau. The thick sedimentary cover of the Mesopotamian Foredeep (or Zagros foreland) and the reported crustal root beneath the Zagros (Snyder and Barazangi 1986) are typical crustal attenuating environment for Lg paths across the Zagros. We observed approximately 100 to 200 km offset in the location of minimum Lg/Pg differential attenuation in comparison to the location of the crustal root. The shift could be due to a lack of stations in the Zagros making the east-west ray paths dominant and smearing the blockage zone westward in the model. Lg propagation in the Turkish-Iranian plateau is mostly blocked or attenuated, which could be due to the intrinsic attenuation in the crustal wave-guide caused by partial melts in this region. This inference is supported by the widespread young volcanism in the region. Finally, the observed Lg blockage in the Mediterranean is consistent with the oceanic nature of most of the region.

The Lg phase was more efficient in the Arabian shield than in the Arabian platform. The shield (dark blue) mapped in our Lg/Pg model matches extremely well the basement map of Figure 1.1. In general, the Arabian plate in our tomography

Lg/Pg model is mainly an efficient region; the fading of the Lg/Pg ratio in the platform could be associated with the thick sedimentary cover of the platform becoming attenuating for Lg. Our limited observations in Oman show inefficient Lg propagation, which could be associated with a change in crustal thickness, for example, the existence of a crustal root under the Oman mountains (Al-Lazki *et al*. 2002). The Lg blockage in the Gulf Oman can be attributed to the existence of oceanic crust up to the entrance of the Arabian/Persian Gulf. This result is consistent with the entire Gulf of Oman consisting of oceanic crust.

Lg blockage in oceanic or very thin continental crust has been documented in several studies (e.g. Press and Ewing 1952; Searle 1975; Zhang and Lay 1995; Sandvol *et al.* 2001). Along the Red Sea we observed some lateral variation in the Lg/Pg ratio tomography indicating a possible change in crustal characteristics. In the northern part of the Red Sea along the Egypt coastline, a zone of Lg blockage was observed in agreement with crustal studies indicating the presence of oceanic crust along the Red Sea coast (Makris and Rhim 1991). The second main area of Lg blockage extends from about latitude 17° south to the southern end of the Red Sea and across to the Afar depression. This region is mainly centered on the Danakil island and the Danakil depression and extends to Afar. The existence of oceanic crust between 15.9° and 26° along the Red Sea axis has been confirmed by magnetic profiles analyzed by Chu *et al.* (1998). Also, Afar is a region of thinned crust (Sandvol *et al.* 1998) and active volcanics. The crust in this whole region could be either thin (oceanic) or thinned continental crust due to the process of stretching and the opening of the Red Sea. An important new result is that Lg efficiently propagate across the central sector of the Red Sea. This suggests major lateral variations in the crust along Red Sea. The Lg blockage zone in Afar continues to the east along the

Gulf of Aden down to the Owen fracture zone, where seismic and magnetic studies of this region found an oceanic crust with an age of about 10 Ma (Cochran 1981).

Sn attenuation is more susceptible to the upper mantle anomalous change in temperature and/or partial melts. In our tomography Sn model (Figure 1.8b) we observed a major Sn blockage zone in the Turkish-Iranian plateau and along and to the east of the Dead Sea fault system. Low Pn velocities were observed in central and eastern Turkey as well as the Caucasus and east of the DSFS (Hearn and Ni 1994; Al-Lazki *et al.* 2003). Sn blockage coupled with low Pn velocities points to the existence of partial melt in the uppermost mantle (i.e., the mantle lid) of the Anatolian plateau as a possible source of blockage and attenuation. To some degree this is substantiated by the existence of widespread Neogene/Quaternary volcanics and active volcanoes (see Figure 1.16). We observed Sn blockage in the Iranian plateau; however, our observations consist predominantly of relatively long propagation paths, that limits our resolution of the extent of Sn attenuation. On the other hand, low Pn velocities observed in the region (Hearn and Ni 1994; Al-Lazki *et al.* 2003), coupled with high Sn attenuation could indicate an anomalously hot lithosphere. The presence of anomalously attenuating and slow uppermost mantle beneath most of the Turkish-Iranian plateau is consistent with localized mantle upwelling caused by the detachment of the subducted Neo Tethys slab during the late Miocene. A large zone of Sn blockage extending from the eastern Mediterranean coast to Jordan, Syria and northwestern Iraq was imaged. The region is characterized by widespread Neogene/Quaternary volcanics as well as very low Pn velocities (Figure 1.16) (Hearn and Ni 1994; Al-Lazki *et al.* 2003) and very low Q_{Pn} (Figure 1.15).

We also observed a region of extensive Sn blockage along the eastern edge of the Dead Sea fault system (DSFS) and farther to the east beneath most of Syria and Jordan (Figure 1.8b). We argue for a possible absence of the lithospheric mantle in this region where the asthenosphere could be in direct contact with the lower crust. This regional anomaly cannot be attributed to continental rifting, since with the exception of the localized pull-apart basins, the DSFS is primarily a transform plate boundary with little, if any, extension, (e.g. McClusky *et al.* 2003; Joffe *et al.* 1987). The scale of the pull-apart basins is not significant to produce such an anomaly. Instead this high attenuation and low Pn velocities may be connected with the hot uppermost mantle from the Gulf of Aqaba, Red Sea, Afar triangle, and east Africa (e.g. Daradich *et al.* 2003). We observed evidence that these lithospheric mantle anomalies may all be connected given the similar nature of their seismic signal and the geochemistry of the basaltic rocks (e.g. Camp and Roobol 1992). We suggest that the DSFS is not responsible for this outstanding major uppermost mantle anomaly, and that this anomaly may predate the development of the DSFS. In fact, it is possible that the location of the DSFS is a result of this upper mantle anomaly.

In most of the Arabian platform, the Zagros, Makran, and the Gulf of Oman, we observed efficient Sn. Sn is more attenuated in the Arabian shield than in the platform, specifically in regions of Neogene/Quaternary volcanics, in Yemen, and along the Red Sea coastal lines. Based on our observations we infer that the lithosphere is not hot or thinned across the entire Arabian shield. The efficient Sn propagation zone in the Arabian platform extends eastward to Zagros, where a clear change to inefficient or blocked Sn occurs along the suture or the thrust line. A region of efficient Sn propagation in the central Red Sea is observed. This is a new and important result. In the northern part of the Red Sea (north of latitude 22°) and along both the Gulf of Aqaba and the Gulf of Suez, Sn is inefficient or blocked. These regions of efficient Sn and blockage indicate that the early stages of opening and sea floor spreading are not simple and uniform along the Red Sea. In general, along the Red Sea, regions of inefficient Sn propagation correlate well with regions of

Figure 1.16. Map showing Sn tomographic model overlain by the tectonic map of the region and the Pn contour lines corresponding to low Pn velocity (Al-Lazki *et al.* 2003). Regions of high Sn attenuation correlate well with regions of low Pn velocities. Also, regions of Sn attenuation correlates with regions of Cenozoic volcanics. See Figure 1.8b for explanation of color-coded bar for Sn efficiency.

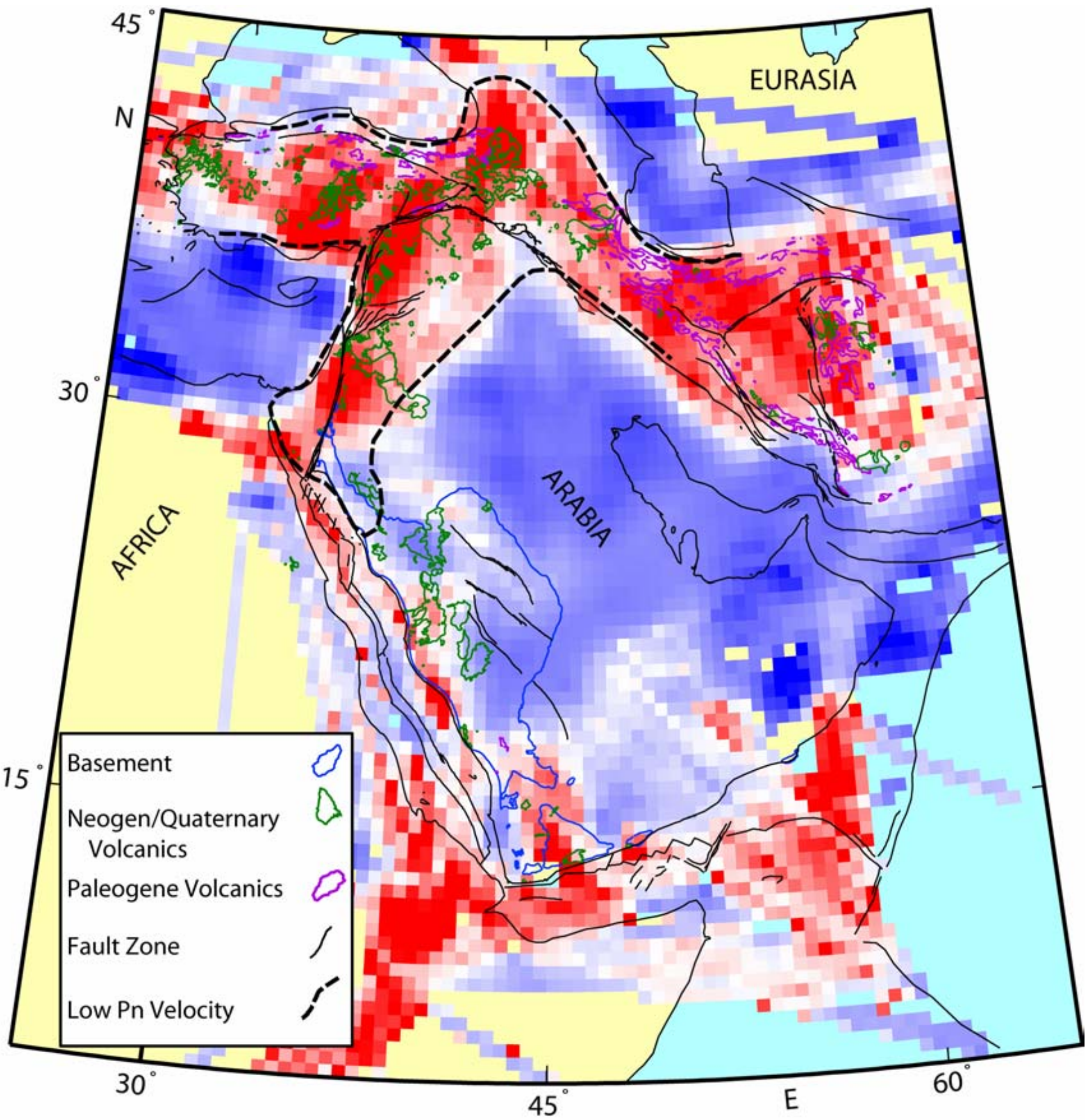
45°
N
30°
15°
30°
45°
E
60°
EURASIA
ARABIA
AFRICA
Basement
Neogen/Quaternary Volcanics
Paleogene Volcanics
Fault Zone
Low Pn Velocity

inefficient Lg propagation. A region of Sn attenuation in Afar extending north along the Danakil depression, east along the Gulf of Aden, and southwest along the east African rift has been clearly mapped by our Sn tomography model that is consistent with the presence of active volcanism and continental rifting.

ACKNOWLEDGEMENTS

The authors would like to thank King Abdulaziz City for Science and Technology (KACST) for providing us with the digital recordings of the Saudi National Seismic Network and providing a scholarship for the first author. We would like also to thank Waris Warsi, Khalfan AL-Tobi, and Salam AL-Hashmi of Sultan Qaboos University for their help in acquiring the Oman temporary network data. We are also grateful to A. Calvert for his help in MATLAB, C. Sandvol, S. Gallow, C. Brindisi, D. Seber, F. Gomez and G. Brew for their help in GIS, computer questions, and helpful comments. We also thank R. Mellors for a careful review of this manuscript. This research is partially supported by the National Science Foundation (Grant No. EAR-9804780).

APPENDIX A

Supplementary Figures

Figure A.1. Map showing more than 6200 Lg ray path efficiencies. Each ray path corresponds to an earthquake-station pair. The seismograms corresponding to these rays were classified by visible inspection by the authors as efficient (map above), inefficient, or blocked (map below).

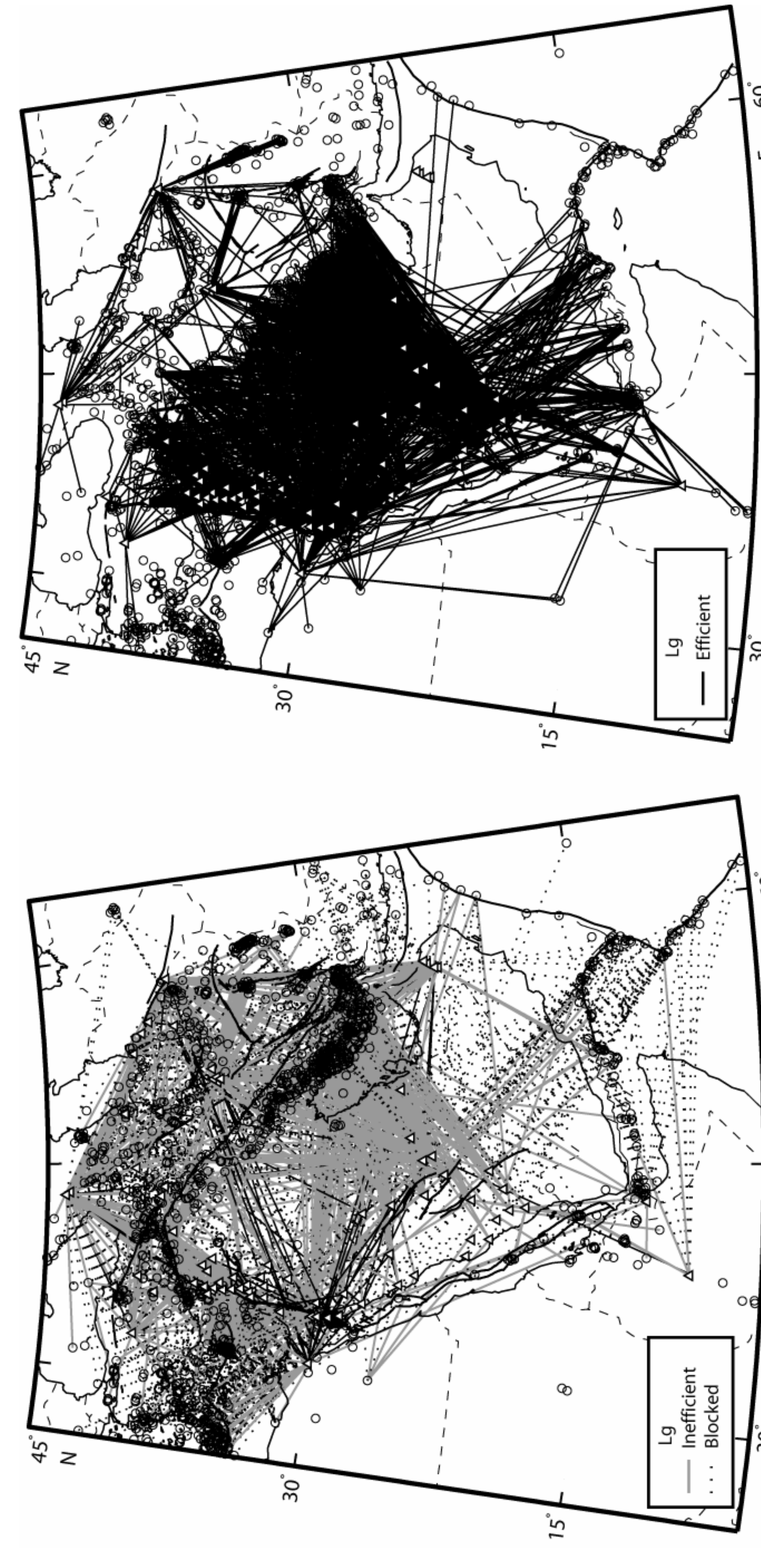
Lg
Efficient
Lg
Inefficient
Blocked
45°
N
30°
15°
30°
45°
60°
E

Figure A.2. Map showing more than 6200 Sn ray paths efficiencies. Each ray path corresponds to an earthquake-station pair. The seismograms corresponding to these rays were classified by visible inspection by the authors as efficient (map above), inefficient, or blocked (map below).

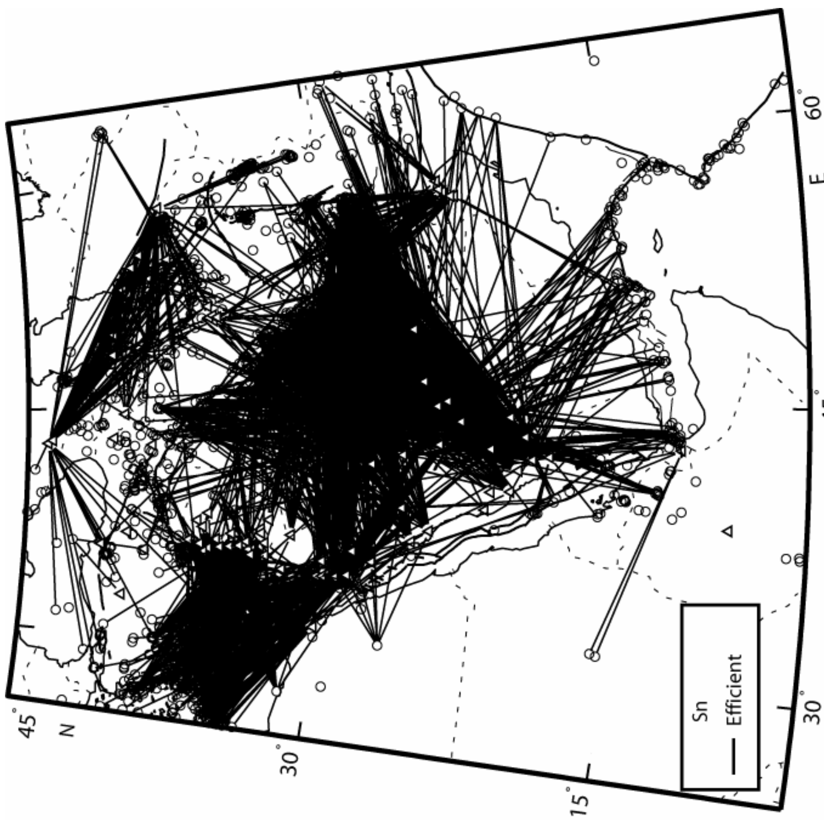
Sn
Efficient
45°
N
30°
15°
30°
45°
60°
E

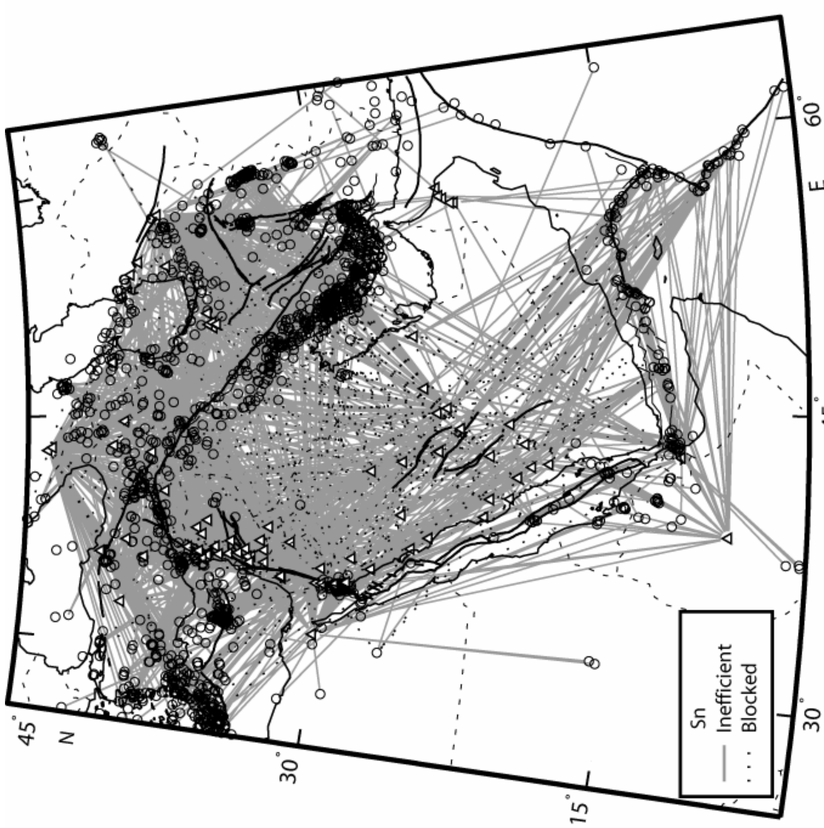
Sn
Inefficient
Blocked
45°
N
30°
15°
30°
45°
60°
E

Figure A.3. Map showing the number of ray hits per cell used in the Lg/Pg ratio tomography.

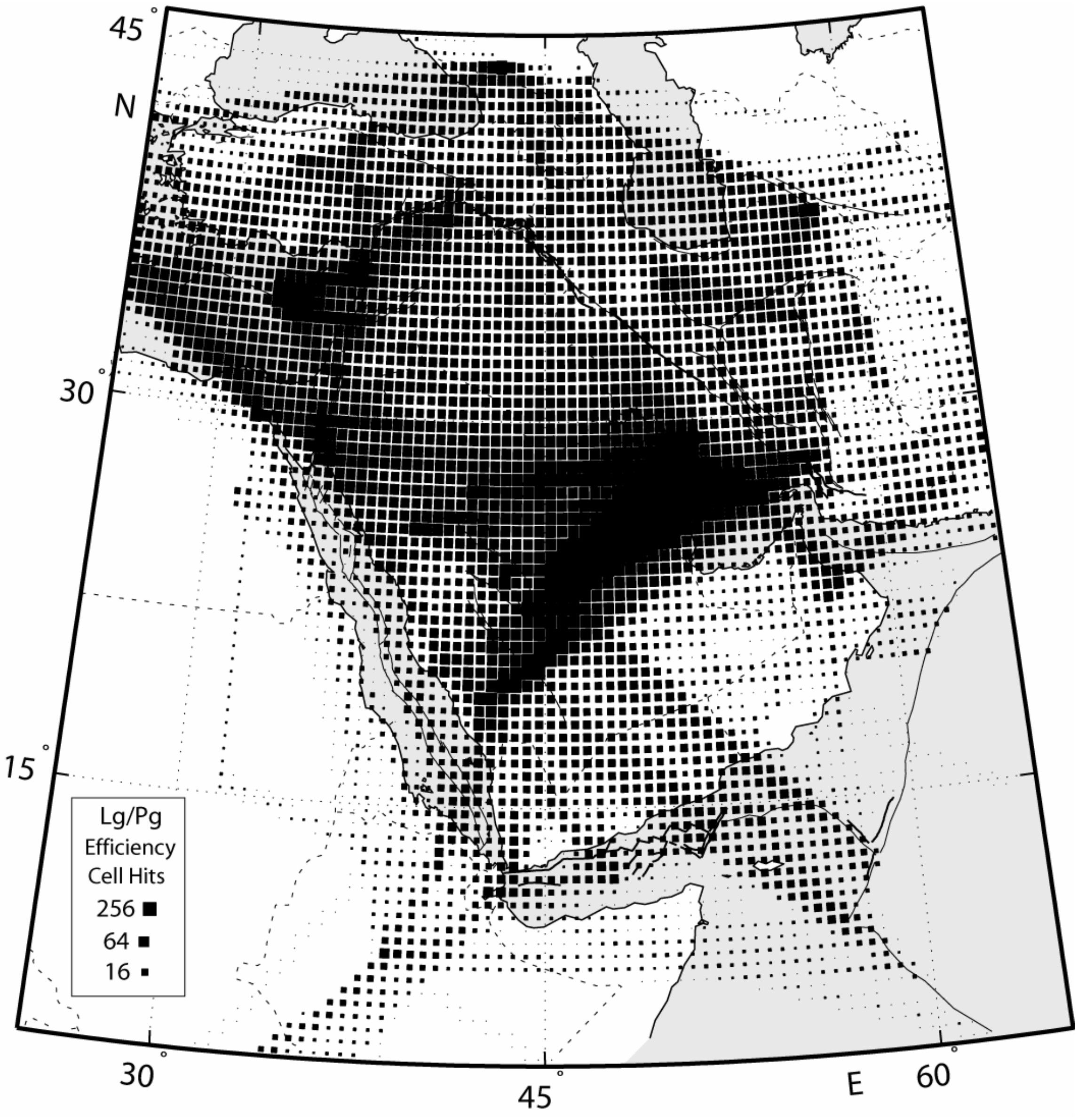
45°
N
30°
15°
Lg/Pg
Efficiency
Cell Hits
256
64
16
30°
45°
E
60°

Figure A.4. Map showing the boot strap uncertainty test (2σ) for the Lg data. High uncertainty values are along the model edges, in southeast of Iran, southeast of Arabian platform, south of the Red Sea, the Gulf of Aden, and Afar region.

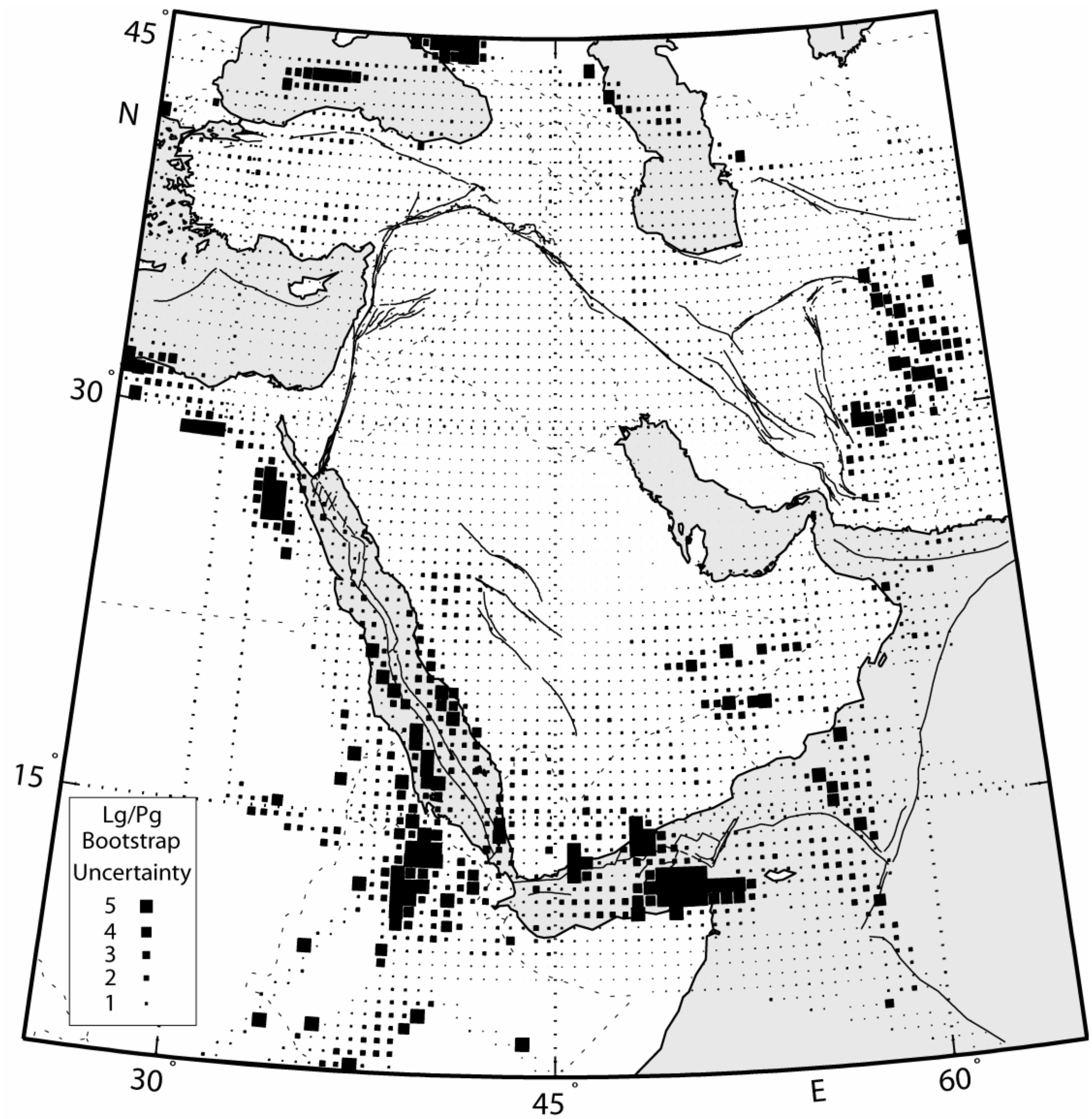
45°
N
30°
15°
30°
45°
E
60°
Lg/Pg
Bootstrap
Uncertainty
5
4
3
2
1

Figure A.5. Map showing the number of ray hits per cell used in the Sn tomography.

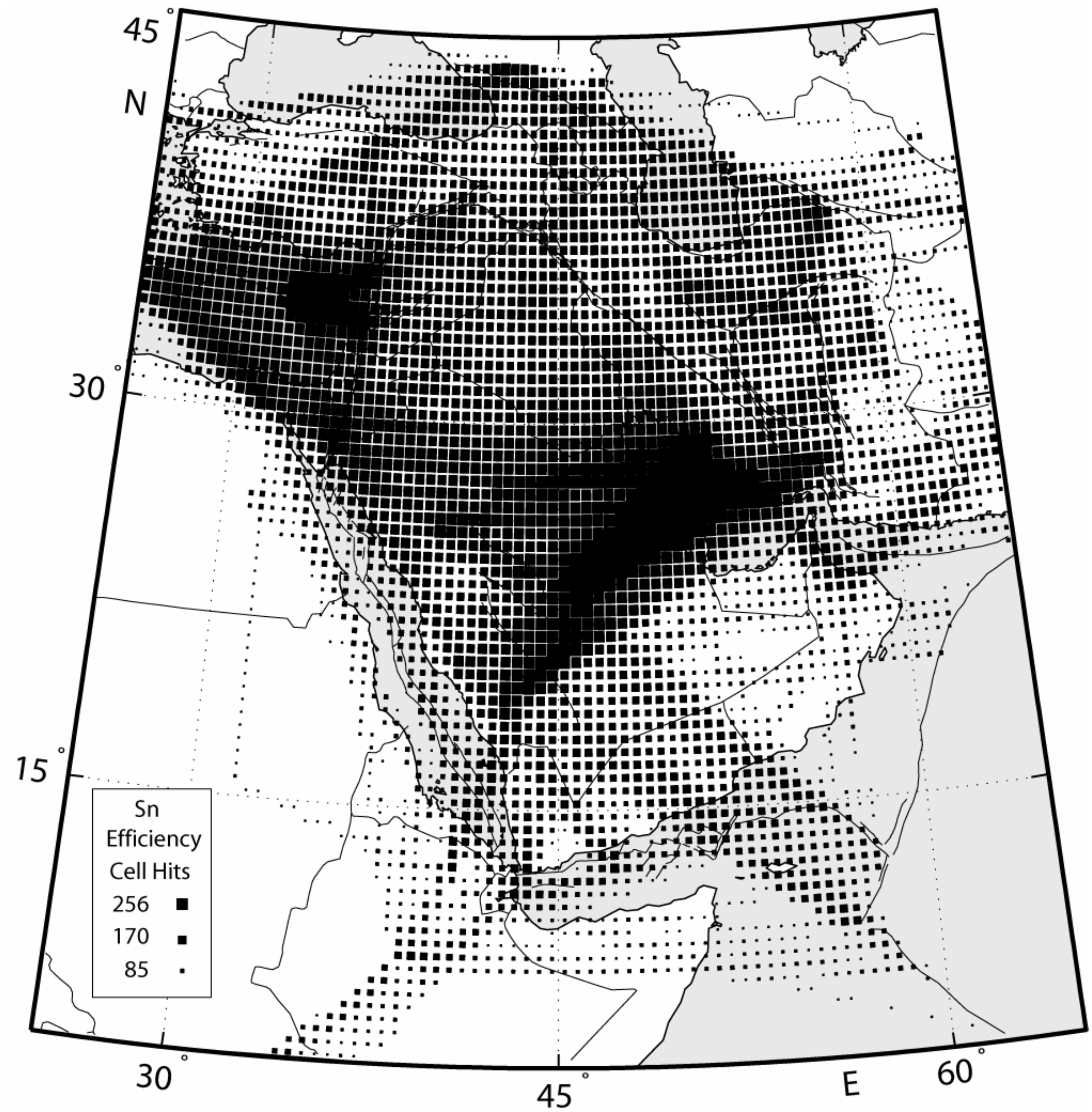
45°
N
30°
15°
30°
45°
E
60°
Sn
Efficiency
Cell Hits
256
170
85

Figure A.6. Map showing the boot strap uncertainty test (2σ) for the Sn data. Similar to the Lg boot strap test, high uncertainty values are along the model edges, in southeast of Iran, southeast of Arabian platform, south of the Red Sea, the Gulf of Aden, and Afar region.

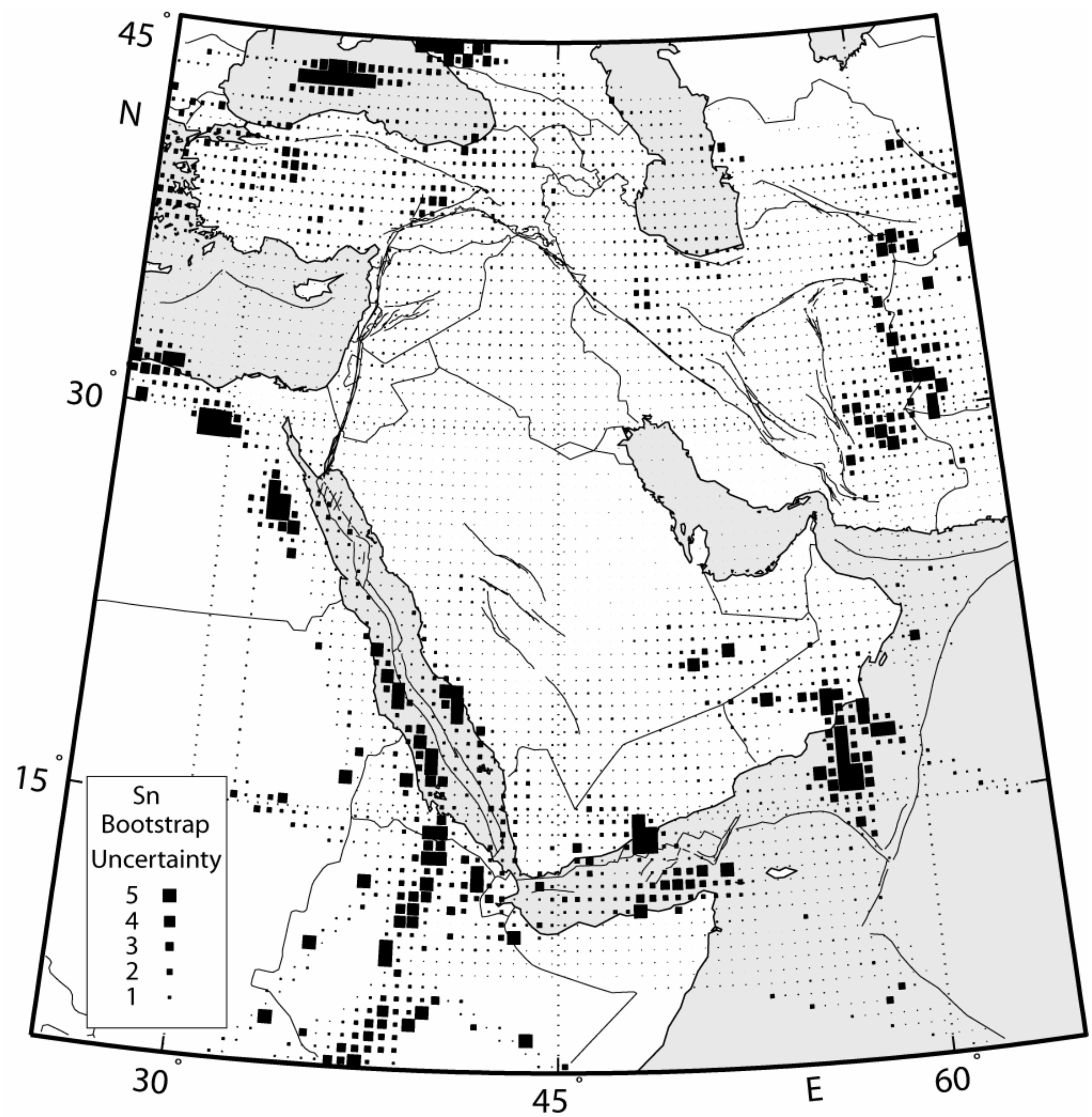

45°
N
30°
15°
Sn
Bootstrap
Uncertainty
5
4
3
2
1
30°
45°
E
60°

REFERENCES

Al-Lazki, A. I., Seber, D., Sandvol, E. and Barazangi, M., 2002. A crustal transect across the Oman mountains of the eastern margin of Arabia, *GeoArabia*, **7**, 47-78.

Al-Lazki, A. I., Sandvol, E., Seber, D., Barazangi, M., Turkelli, N. and Mohamad, R., 2003. Pn tomographic imaging of mantle lid velocity and anisotropy at the junction of the Arabian, Eurasian, and African plates, submitted to Geophys. J. Int.

Badri, M. and Sinno, Y., 1991. Qp crustal structure in central Saudi Arabia, *Journal of African Earth Sciences*, **12**, 561-568.

Barka, A. and Reilinger, R., 1997. Active tectonics of the eastern Mediterranean region: deduced from GPS, neotectonic and seismicity data, *Annali Di Geofisica*, **40**, 587-610.

Baumgardt, D.R., 1996. Investigations of Lg blockage and transportability of regional discriminations in the Middle East, *Sci. Report 1, PL-TR-96-2294, ENSCO Inc.*, Springfield, Virginia.

Baumgardt, D.R. and Der, Z., 1997. Investigation of the transportability of the P/S ratio discriminate to different tectonic regions, *Sci. Report 1, PLT-TR-94-229*, *ENSCO, Inc.*, Springfield, Virginia.

Bostock, M. and Kennett, B.L.N., 1990. The effect of 3-D structure on Lg propagation patterns, *Geophys. J. Int.*, **101**, 355-365.

Bouchon, M., 1982. Complete synthesis of seismic crustal phases at regional distances, *J. Geophys. Res.*, **87**, 1,735-1,741.

Brew, G., Barazangi, M., Al-Maleh, A.K. and Sawaf, T., 2001. Tectonic and geologic evolution of Syria, *GeoArabia*, **6**, 573-616.

Calvert, A., Sandvol, E., Seber, D., Barazangi, M., Vidal, F., Alguacil, G. and Jabour, N., 2000. Propagation of regional seismic phases (Lg and Sn) and Pn velocity structure along the Africa-Iberia plate boundary zone: Tectonic implications, *Geophys. J. Int.*, **142**, 384-408.

Chu, D. and Gordon, R., 1998. Current plate motion across the Red Sea*, Geophys. J. Int.*, **135**, 313-328.

Chun, K.Y., 1986. One-parameter approach to surface wave γ measurement, *Earthquake Notes*, **57**, 4, 111.

Chun, K.Y., West, G.F., Kokoski, R.J. and Samson, C., 1987. A novel technique for measuring Lg attenuation: results from eastern Canada between 1 to 10 Hz, *Bull. Seism. Soc. Am.*, **77**, 398-419.

Camp, V.E. and Roobol, M.J., 1992. Upwelling asthenosphere beneath western Arabia and its regional implications, *J. Geophys. Res.*, **97**, 15255-15271.

Cochran, J.R., 1981. The Gulf of Aden, structure and evolution of a young ocean basin and continental basin, *J. Geophys. Res.*, **86**, 263-288.

Cochran, J.R., 1983. Model for development of the Red Sea, *Am. Assoc. Pet. Geol. Bull.*, **67**, 41-69.

Cochran, J.R. and Martinez, F., 1988. Structure and tectonics of the northern Red Sea: Catching a continental margin between rifting and drifting, *Tectonophysics*, **150**, 1-32.

Cong, L. and Mitchell, B., 1998. Lg coda Q and its relation to the geology and tectonics of the Middle East, *Pure appl. Geophys.*, **153**, 563-585.

Cong, L.L., Xie, J.K. and Mitchell, B., 1996. Excitation and propagation of Lg from earthquakes in Central Asia with implications for explosion/earthquake discrimination, *J. Geophys. Res.*, **101**, 27,779-27,789.

Daradich, A., Mitrovica, J.X., Pysklywec, R.N., Willett, S.D., and Forte, A.M., 2003. Mantle flow, dynamic topography, and rift-flank uplift of Arabia, *Geology*, **31**, 901-904.

Dewey, J.F. and Sengor, A., 1979. Aegean and surrounding regions: Complex multiplate and continuum tectonics in a convergence zone, *Geol. Soc. Am. Bull.*, **90**, 84-92.

Dewey, J.F., Pitman, W., Ryan, W. and Bonnin, J., 1973. Plate tectonics and the evolution of the Alpine system, *Geol. Soc. Am. Bull.*, **84**, 3137-3180.

Fan, G. and Lay, T., 1998. Statistical analysis of irregular waveguide influences on regional seismic discriminates in China, *Bull. Seism. Soc. Am.*, **88**, 74-88.

Farhoudi, G. and Karig, D., 1977. Makran of Iran and Pakistan as an active arc system, *Geology*, **5**, 664-668.

Garfunkel, Z., 1981. Internal structure of the Dead Sea leaky transform (rift) in relation to plate kinematics, *Tectonophysics*, **80**, 81-108.

Gok, R., Turkelli, N., Sandvol, E., Seber, D. and Barazangi, M., 2000. Regional wave propagation in Turkey and surrounding regions, *Geophys Res. Lett.*, **27**, 429-432.

Hartse, H., Flores, R. and Johnson, P., 1998. Correcting regional seismic discriminants for path effect in western China, *Bull. Seismol, Soc. Am.*, **88**, 596-608.

Hearn, T.M. and Ni, J.F., 1994. Pn velocity beneath continental collision zones: the Turkish-Iranian Plateau, *Geophys. J. Int.*, **117**, 273-283.

Hempton, M., 1987. Constraints on Arabian plate motion and extensional history of the Red Sea, *Tectonics*, **6**, 2, p. 687-705.

Hill, D.P., 1973. Critically refracted waves in a spherically symmetric radially heterogeneous earth model, *Geophys. J. R. Astr. Soc.*, **46**, 407-432.

Huestis, S., Molnar, P. and Oliver, J., 1973. Regional Sn velocities and shear velocity in the uppermost mantle, *Bull. Seismol. Soc. Am.*, **63**, 469.

Jacob, k. and Quittmeyer, R., 1979. The Makran region of Pakistan and Iran: Trench-arc system with active plate subduction, in *Geodynamics of Pakistan*, pp. 305-317, ed. Farah, A. and DeJong, K., Geological Survey of Pakistan, Quetta.

Joffe, S. and Garfunkel, Z., 1987. Plate kinematics of the circum Red Sea; a re-evaluation, *Tectonophysics*, **141**, 5-22.

Kadinsky-Cade, K., Barazangi, M., Oliver, J. and Isacks, B., 1981. Lateral variation in high frequency seismic wave propagation at regional distances across the Turkish and Iranian plateaus, *J. Geophys. Res.*, **86**, 9377-9396.

Kadinsky-Cade, K. and Barazagni, M., 1982. Seismotectonics of southern Iran: The Oman line, *Tectonics*, **1**, 389-412.

Kennett, B, L.N., 1986. Lg waves and structural boundaries, *Bull. Seismol. Soc. Am.*, **76**, 1,133-1,141.

Le Pichon, X. and Girdler, J.M., 1988. The rotation of Arabia and the Levant fault system, *Tectonophysics*, **153**, 271-294.

Makris, M.J. and Rhim, R., 1991. Shear-controlled evolution of the Red Sea: pull-apart model, *Tectonophysics*, **198**, 441-446.

McClusky, S., Reilinger, R., Mahmoud, S., Sari, D. B. and Tealeb, A., 2003. GPS constraints on Africa (Nubia) and Arabian plate motion, *Geophys. J. Int.*, 155, 126-138.

McKenzie, D., 1976. The East Anatolian fault; a major structure in eastern Turkey, *Earth Planet. Sci. Lett.*, **29**, 189-193.

McKenzie, D.P., Davies, D. and Molnar, P., 1970. Plate tectonics of the Red Sea and East Africa, *Nature*, **226**, 242-248.

Mellors, R., Vernon, F., Camp, V., AL-Amri, A., Ghalib, A. and AL-Dail, M., 1999. Regional wave propagation in the Saudi Arabian peninsula, *Geophys. Res. Lett.*, 104, 20,221-20,235.

Mitchell, B.J., Pan, Y., Xie, J. and Cong, L., 1997. Lg coda Q variation across Eurasia and its relation to crustal evolution, *J. Geophys. Res.,* **102,** 22,767-22,779.

Mokhtar, T.A., Ammon, C.A., Herrmann, R.B. and Ghalib, A.A., 2001. Surface wave velocity across Arabia, *Pure Appl. Geophys.*, **158**, 1425-1444.

Molnar, P. and Oliver, J., 1969. Lateral variation of attenuation in the uppermost mantle and discontinuities in the lithophsere, *J. Geophys. Res.*, **74**, 2,648-2,683.

Nuttli, O., 1980. The excitation and attenuation of seismic crustal phases in Iran, *Bull. Seismol. Soc. Am.*, **70**, 469-480.

Paige, C.C. and Saunders, M.A., 1982. LSQR: An algorithm for sparse linear equations and sparse least squares, *ACM Trans. Math. Software*, **8**, 43-71.

Park, J., 1987. Multitaper spectral analysis of high-frequency seismograms, *J. Geophys. Res.*, **92**, 12,675-12,684.

Phillip, H., Cisternas, A., Gvishiani, A. and Gorshkov, A., 1989. The Caucasus: an actual example of the initial stages of continental collision, *Tectonophysics*, **161**, 393-398.

Phillips, W. S., Hartse, H. E., Taylor, S., Velasco, A. A. and Randall, G. E., 2001. Application of regional phase amplitude tomography to seismic verification, *Pure appl. Geophys.*, **158**, 1189-1206.

Powers, R.W., Ramirez, L.F., Redmond, C.P. and Elberg, E.L., 1966. Geology of the Arabian Peninsula: Sedimentary Geology of Saudi Arabia, *U.S. Geol. Surv. Prof. Pap.*, **560-D**, 91-96.

Press, F., and Ewing, M., 1952. Two slow surface waves across North America, *Bull. Seismol. Soc. Am.*, **42**, 219-228.

Rodgers, A., Ni, J. and Hearn , T., 1997. Propagation characteristics of short-period Sn and Lg in the Middle east, *Bull. Seism. Soc. Am.*, **87**, 396-413.

Sandvol, E., Al-Damegh, K., Calvert, A., Seber, D., Barazangi, M., Mohamad, R., Gok, R., Turkelli, N. and Gurbuz, C., 2001. Tomographic imaging of observed regional wave propagation in the Middle East, *Pure appl. Geophys.*, **158**, 1121-1163.

Sandvol, E., Seber, D., Barazangi, M., Vernon, F., Mellors, R. and Al-Amri, A., 1998. Lithospheric seismic velocity discontinuities beneath the Arabian shield, *Geophs. Res. Lett*., **25**(15), 287-2876.

Searle, R.C. 1975. The dispersion of surface waves across the Afar. In *Afar Depression of Ethiopia*, pp. 113-120, eds. Pilgerand, A. and Roesler, A., Schweizerbart, Stuttgart, Germany.

Seber, D., Vallve, M., Sandvol, E., Steer, D. and Barazangi, M., 1997. Middle East tectonics: applications of geographic information system (GIS), *GSA Today,* **7**, 1-6.

Sengor, A.M.C. and Kidd, W.S.F., 1979. Post-collisional tectonics of the Turkish-Iranian Plateau and a comparison with Tibet, *Tectonophysics*, **55**, 361-376.

Sereno, T.J., 1989. Numerical modeling of Pn geometric spreading and empirically determination attenuation of Pn and Lg phases recorded in eastern Kazakhstan, *Technical Report of Science Application International Corporation*, SAIC 89/1555, San Diego.

Snyder, D. and Barazangi, M., 1986. Deep crustal structure and flexure of the Arabian plate beneath the Zagros collisional mountain belt as inferred from gravity observations, *Tectonics*, **5**, 361-373.

Stocklin, J., 1974. Possible ancient continental margins in Iran, in *Geology of Continental Margins*, ed. Burk, C. and Drake, C., pp. 873-877, Springer-Verlag, New York.

Zhang, T.R. and Lay, T., 1995. Why the Lg phase does not traverse oceanic crust, Bull. seism. Soc. Am., **85**, 1665-1678.

Zhu, T., Chun, K. and West, G.F., 1991. Geometrical spreading and Q of Pn waves: an investigative study in eastern Canada, *Bull. Seism. Soc. Am.*, **81**, 882-896.

Zonenshain, L. and LePichon, X. 1986. Deep basins of the Black Sea and Caspian Sea as remnants of Mesozoic back-arc basins, *Tectonophysics*, **123**, 181-211.

CHAPTER TWO

CRUSTAL STRUCTURE OF THE ARABIAN PLATE: NEW CONSTRAINTS FROM THE ANALYSIS OF TELESEISMIC RECEIVER FUNCTIONS*

ABSTRACT

Receiver functions for numerous teleseismic earthquakes recorded at 23 broadband and mid–band stations in Saudi Arabia and Jordan were analyzed to map crustal thickness within and around the Arabian plate. We used spectral division as well as time domain deconvolution to compute the individual receiver functions and receiver function stacks. The receiver functions were then stacked using the slant stacking approach to estimate Moho depths and Vp/Vs for each station. The errors in the slant stacking were estimated using a bootstrap re-sampling technique. We also employed a grid search waveform modeling technique to estimate the crustal velocity structure for seven stations. A jackknife re-sampling approach was used to estimate errors in the grid search results for three stations. In addition to our results, we have also included published receiver function results from two temporary networks in the Arabian shield and Oman as well as three permanent GSN stations in the region.

The average crustal thickness of the late Proterozoic Arabian shield is 39 km. The crust thins to about 23 km along the Red Sea coast and to about 25 km along the margin of the Gulf of Aqaba. In the northern part of the Arabian platform, the crust varies from 33 – 37 km thick. However, the crust is thicker (41 – 53 km) in the southeastern part of the platform. There is a dramatic change in crustal thickness between the topographic escarpment of the Arabian shield and the shorelines of the Red Sea. We compared our results in the Arabian shield to nine other Proterozoic and

* Submitted for publication to Earth and Planetary Science Letters on April 06, 2004 as "Crustal structure of the Arabian plate: New constraints from the analysis of teleseismic receiver functions" by Khaled S. Al-Damegh, Eric Sandvol, and Muawia Barazangi.

Archean shields that include reasonably well-determined Moho depths, mostly based on receiver functions. The average crustal thickness for all shields is 39 km, while the average for Proterozoic shields is 40 km, and the average for Archean shields is 38 km. We found the crustal thickness of Proterozoic shields to vary between 33 and 44 km, while Archean shields vary between 32 and 47 km. Overall, we do not observe a significant difference between Proterozoic and Archean crustal thickness.

We observed a dramatic change in crustal thickness along the Red Sea margin that occurs over a very short distance. We projected our results over a cross section extending from the Red Sea ridge to the shield escarpment and contrasted it with a typical Atlantic margin. The transition from oceanic to continental crust of the Red Sea margin occurs over a distance of about 250 km, while the transition along a typical portion of the western Atlantic margin occurs at a distance of about 450 km. This important new observation highlights the abruptness of the breakup of Arabia. We argue that a preexisting zone of weakness coupled with anomalously hot upper mantle could have initiated and expedited the breakup.

INTRODUCTION

The Arabian plate consists of a late Proterozoic shield bounded to the east by a Phanerozoic platform and separated from the African plate by a very young spreading center located within the Red Sea and the Gulf of Aden (Figure 2.1). The shield consists of a series of Proterozoic accreted island arc terrains that were assembled during several subduction episodes (Greenwood *et al.*, 1980). The Arabian/Nubian shields were separated by a rifting process that started in Afar and propagated eastward and northward creating the Gulf of Aden and the Red Sea, respectively (Cochran and Martinez, 1988). The Arabian shield is generally elevated with respect to the Arabian platform and is marked along its western boundary by an escarpment reaching more than 2000 m in some places. The platform overlaps the eastern part of the shield unconformably and consists of thick Paleozoic and Mesozoic sedimentary layers dipping eastward and reaching 10 km or more in thickness (Power *et al*., 1966; Brown, 1972; Mokhtar *et al*., 2001).

It appears that the Red Sea consists of both oceanic and attenuated/thinned continental crust (Makris and Rhim, 1991; Al-Damegh *et al*., 2004). Neogene and Quaternary volcanics are present along the western part of the Arabian plate (Camp and Roobol, 1992). The Dead Sea fault system is located along the northwestern boundary of the Arabian plate. The fault is left lateral with a minor component of rotation that results in the development of pull-apart basins, such as the Dead Sea rift basin (Garfunkel, 1981). The Mesopotamian foredeep, which is located to the west of the Zagros fold and thrust belt, consists of thick sediments that increase in thickness toward the Zagros belt (Seber *et al*., 1997).

Two large seismic experiments have been conducted in the Arabian shield. A deep refraction line was shot in 1978. More recently a temporary deployment of broadband seismic stations was deployed in central Saudi Arabia. Both of these experiments were primarily focused on the southern part of the shield and ran from near the Red Sea coast to the western portion of the platform. Results from both experiments suggest that the Arabian shield has an average crustal thickness of 40 km, thinning rapidly near the Red Sea coast and gradually increasing toward the platform (Mooney *et al*., 1985; Gettings *et al*., 1986; Sandvol *et al*., 1998b; Kumar *et al*., 2002). Specifically in the Arabian platform, Al-Amri, 1999 and Al-Amri and Gharib, 2000 reported a 46 km thick crust under RIYD station (Figure 2.2) and 51 km near the Arabian/Persian Gulf using teleseismic body wave spectra. In Oman, southeast of RIYD station, the crust is about 41 - 49 km thick (Al-Lazki *et al*., 2002). In the

Figure 2.1. A simplified tectonic map showing the main tectonic features of the Arabian plate and surrounding regions.

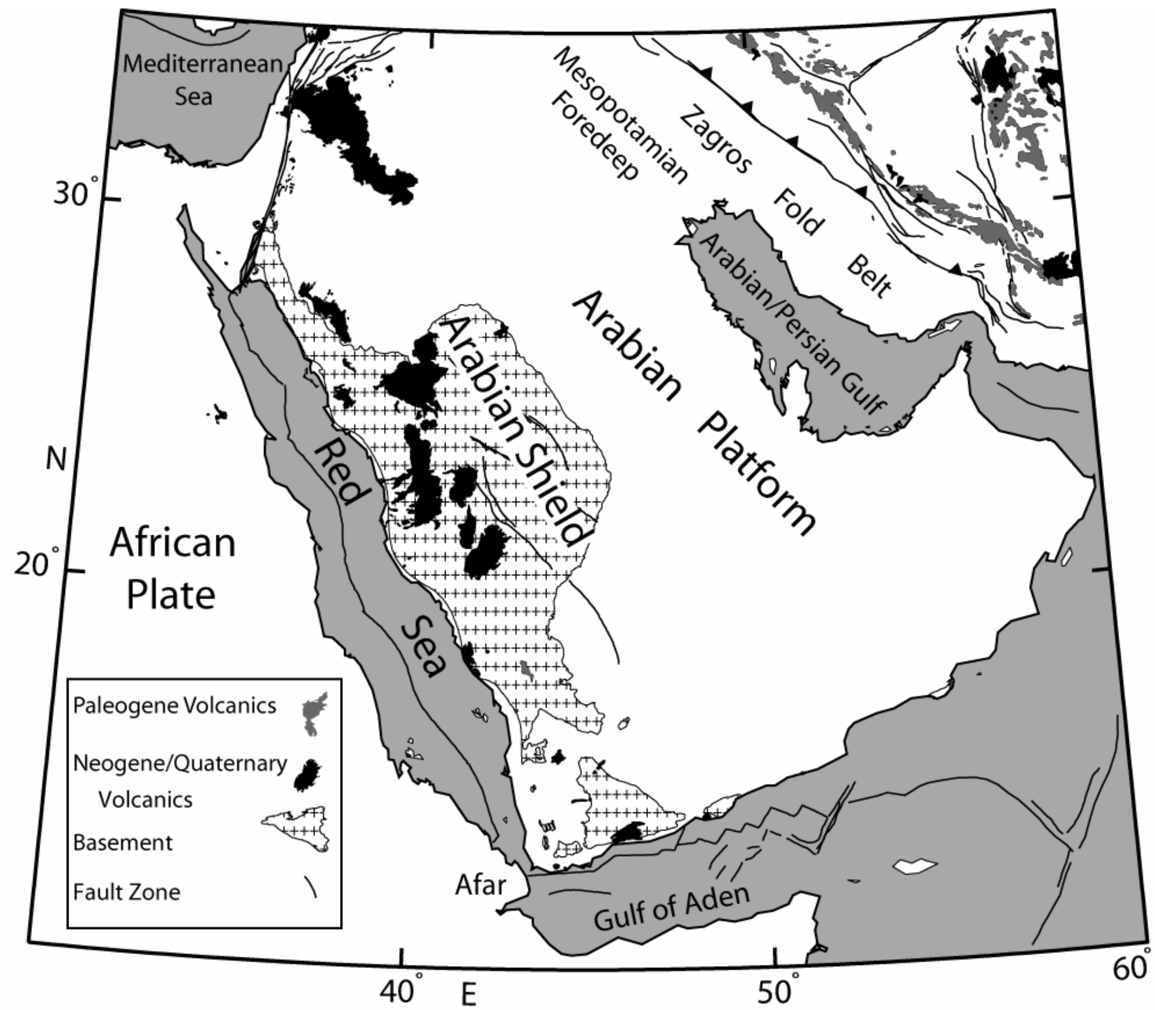

Mediterranean Sea
Mesopotamian Foredeep
Zagros Fold Belt
Arabian/Persian Gulf
Arabian Platform
Arabian Shield
Red Sea
African Plate
Afar
Gulf of Aden
30°
20°
N
40°
E
50°
60°
Paleogene Volcanics
Neogene/Quaternary Volcanics
Basement
Fault Zone

northern and northwestern part of the platform, the crust seems to vary between 33 and 40 km (El-Isa *et al*., 1987; Sandvol *et al*., 1998a; Rodgers *et al*., 2003; Zor *et al*., 2003). Surface waves as well as regional waveform modeling indicate that on average the Arabian shield crust is 40 - 45 km thick, slightly thicker than the average crust for most shields on earth (Seber and Mitchell, 1992; Mokhtar, 1995; Rodgers *et al*., 1999). Also, slower-than-average P and S velocities were found in the uppermost mantle beneath the western part of the shield (Debayle *et al*., 2001; Benoit *et al*., 2003), indicating the upper mantle is anomalously hot and is possibly associated with the uplift of the Arabian shield (Benoit *et al*., 2003; Daradich *et al*., 2003). The low velocity anomaly was found to extend from the Red Sea eastward into the interior of the shield and to be confined to depths shallower than 410 km (Benoit *et al*., 2003).

Seismic receiver functions are typically used to image the depth to major velocity discontinuities in the crust and uppermost mantle. Lateral variation of crustal thickness in a region is an important parameter in understanding the geologic and tectonic processes that have been dominant in the region. This study makes use of a new waveform database produced by a recently established permanent broadband seismic array in Saudi Arabia (Al-Amri and Al-Amri, 1999) as well as 2 intermediate band permanent stations in Jordan (Rodgers *et al*., 2003). This database provided us with the opportunity to use teleseismic receiver functions to map the crustal thickness and crustal Vp/Vs in the Arabian plate.

DATA

The data used in this study consist primarily of teleseismic recordings from 21 broadband permanent stations in Saudi Arabia and 2 intermediate-band temporary stations in Jordan (see Figure 2.2). The broadband stations in Saudi Arabia have been deployed by King Abdulaziz City for Science and Technology (KACST) since mid

Figure 2.2. Map showing the seismic stations used in this study. In addition, the map shows stations in the region for which receiver function results were discussed in the text (squares, stars, and downward triangles). The inset shows stations along or close to the Gulf of Aqaba.

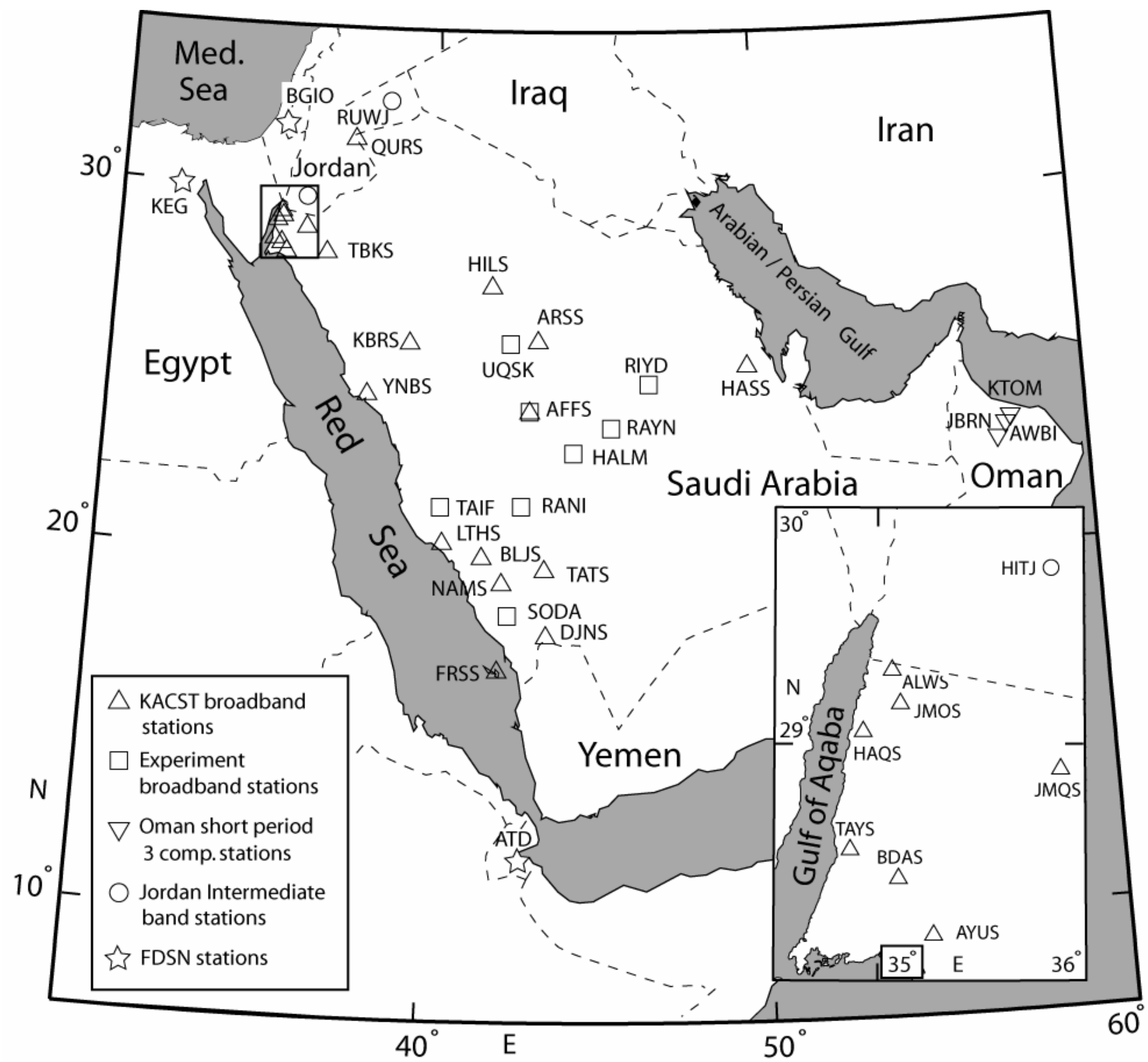
Med. Sea
Iraq
Iran
Jordan
Egypt
Red Sea
Saudi Arabia
Oman
Yemen
Arabian / Persian Gulf
Gulf of Aqaba
BGIO
RUWJ
QURS
KEG
TBKS
HILS
ARSS
KBRS
UQSK
RIYD
HASS
KTOM
JBRN
AWBI
YNBS
AFFS
RAYN
HALM
TAIF
RANI
LTHS
BLJS
TATS
NAMS
SODA
DJNS
FRSS
ATD
HITJ
ALWS
JMOS
HAQS
JMQS
TAYS
BDAS
AYUS
KACST broadband stations
Experiment broadband stations
Oman short period 3 comp. stations
Jordan Intermediate band stations
FDSN stations
30°
20°
10°
29°
35°
36°
40°
50°
60°
N
E

1998, and the data are transmitted to a central station via dedicated phone lines (Al-Amri and Al-Amri, 1999). The data from Jordan span a period of approximately two years and were deployed jointly with the United States Geological Survey (USGS), the Jordan Seismological Observatory (JSO), and the Lawrence Livermore National Laboratory (LLNL) (Rodgers *et al*., 2003). These combined 23 stations span a large region across the western Arabian plate; although a majority are located within the Arabian shield. Table 2.1 lists the location of stations used in this study. Both networks recorded continuously with a high sampling rate (100 Hz for the Saudi stations and 50 Hz for the Jordanian stations). We used the USGS/PDE monthly catalog times to associate and window teleseismic seismograms with distances between 35 and 85 degrees. The first arrival waveforms were windowed and sub-sampled to 20 Hz. We have also included in our study proximal published receiver function results in the region from Sandvol *et al*., 1998a, 1998b, and Al-Lazki *et al*., 2002. These studies utilized seismic data from temporary networks in Saudi Arabia and Oman in addition to permanent GSN stations in the region.

METHODS

P to S converted phases originating from near receiver velocity discontinuities have been used to infer crustal and upper mantle structure for the past 30 years (e.g., Burdick and Langston, 1977; Langston, 1979) (see Figure 2.3). Receiver functions are calculated by de-convolving the vertical from the radial and tangential components and are used to isolate and identify P to S converted phases. The time delay between the first arriving direct wave and the associated converted phases is a function of the depth and velocity structure of the medium. We have calculated receiver functions in this study using both spectral deconvolution (Burdick and Langston, 1977) and time domain methods (Ligorria and Ammon, 1999). We observed very little difference in the receiver functions generated by both methods, indicating that our waveform data are relatively stable. We have applied a Gaussian low pass filter with a corner frequency of 0.5 Hz to all our receiver functions. Using the time difference between the PS_{Moho} phase and the first arrival, the depth to Moho can be estimated based on the following equation:

$$H = t_{ps} /((1/Vs^2-p^2)^{1/2} - (1/Vp^2-p^2)^{1/2}) \quad (2.1)$$

where H is the depth to Moho, t_{ps} is the time delay between the first arrival and the Moho phase, Vs is the S wave velocity, Vp is the P wave velocity, and p is the ray parameter.

However, since the delay time of the S leg is dependent on the shear velocity of the medium, the crustal thickness trades off strongly with the seismic wave velocity (Zhu and Kanamori, 2000). Incorporating multiply reflected phases such as PsPs and PpSs+PsPs (Figure 2.3) helps reduce this trade off significantly. The time delays (t_{PpPs} and $t_{PpSs+PsPs}$) for PsPs and PpSs+PsPs phases and H can be expressed in the following equations:

$$H = t_{PpPs} /((1/Vs^2-p^2)^{1/2} + (1/Vp^2-p^2)^{1/2}) \quad (2.2)$$

$$H = t_{PpSs+PsPs} /2(1/Vs^2-p^2)^{1/2} \quad (2.3)$$

To further enhance the signal/noise ratio and reduce lateral variations, multiple receiver functions are stacked in the time domain. Zhu and Kanamori 2000 developed a straightforward approach that adds the amplitudes of the PS_{Moho} and multiples at the predicted time by varying H (crustal thickness) and the Vp/Vs. This “slant stacking” approach essentially transforms the receiver function stacks from the time domain to the H-Vp/Vs domain. The H-Vp/Vs domain stacking is defined by:

$$S(H,Vp/Vs) = w_1r(t_{ps}) + w_2r(t_{PpPs}) - w_3r(t_{PpSs+PsPs}) \quad (2.4)$$

where the $r(t_{ps})$ is the amplitude of the receiver function at the time t_{ps} and w_1, w_2, and w_3 are the weighting factors that sum to unity. The main advantage of this technique

Table 2.1. A list of the seismic stations used in this study as well as this study's receiver function results. It should be noticed that the errors presented here are based on statistical re-sampling methods (bootstrap) and reflect the consistency in our data. Certainly the actual total error in determining the absolute Moho depth by any geophysical method might exceed these numbers.

	Station	Latitude (N)	Longitude (E)	Elevation (m)	Moho Depth (km) Slant Stack	Vp/Vs	Error in Depth (km)	Error in Vp/Vs
1	AFFS	23.93	43.00	1090	31.9	1.820	1.46	0.056
2	ARSS	25.88	43.24	720	39.5	1.740	1.00	0.038
3	BDAS	28.43	35.10	360	26.9	1.755	2.16	0.072
4	BLJS	19.88	41.60	2060	38.0	1.735	1.78	0.044
5	DJNS	17.71	43.54	2200	43.5	1.830	5.20	0.088
6	FRSS	16.74	42.11	0	14.4	1.760	1.02	0.090
7	HAQS	29.05	34.93	420	26.5	1.755	3.48	0.102
8	HASS	25.19	49.69	200	41.2	1.810	0.52	0.022
9	HILS	27.38	41.79	1080	36.9	1.775	0.70	0.024
10	KBRS	25.79	39.26	780	35.2	1.735	0.74	0.038
11	LTHS	20.27	40.41	180	22.2	1.740	1.94	0.070
12	NAMS	19.17	42.21	2520	41.6	1.690	1.60	0.032
13	QURS	31.39	37.32	491	32.9	1.710	4.50	0.100
14	TATS	19.54	43.48	1100	40.0	1.785	2.44	0.048
15	TBKS	28.22	36.55	820	34.4	1.780	2.14	0.054
16	YNBS	24.34	37.99	80	31.6	1.700	3.42	0.082
17	AYUS	28.19	35.27	0	27.5	1.685	2.04	0.068
18	TAYS	28.55	34.87	0	28.2	1.720	1.84	0.056
19	JMQS	28.89	35.88	0	36.6	1.785	1.52	0.042
20	ALWS	29.31	35.07	0	24.7	1.810	1.64	0.078
21	JMOS	29.17	35.11	0	28.8	1.805	1.18	0.036
22	HITJ	29.74	35.84	1235	36.4	1.730	1.42	0.036
23	RUWJ	32.48	38.40	751	37.2	1.785	0.74	0.016

Figure 2.3. A schematic ray-tracing diagram for hypothetical teleseismic plane P wave incident on a 40 km thick crust. Ps, PpPs, PpSs, and PsPs are abbreviations for the Moho phase and the following multiples that we used in this study to estimate the crustal thickness for the Arabian plate.

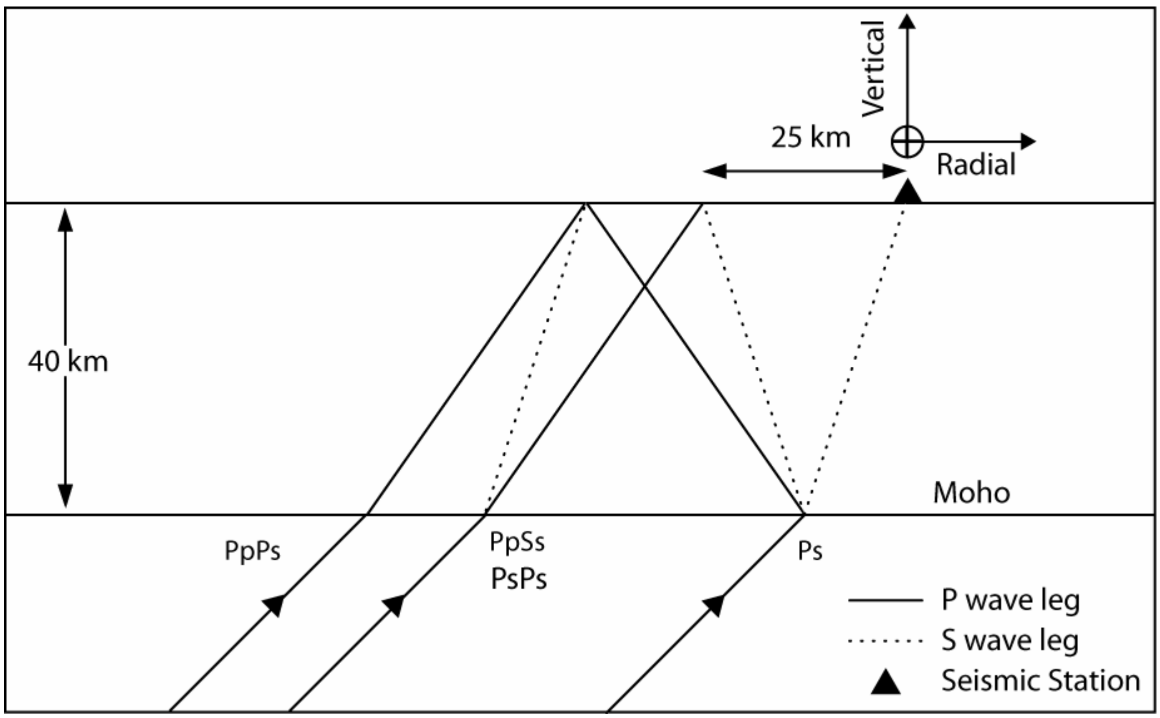
Vertical
25 km
Radial
40 km
Moho
PpPs
PpSs
PsPs
Ps
P wave leg
S wave leg
Seismic Station

is that there is no need to pick the arrival times of the Moho or the multiples, making this technique more objective than having to manually identify these various phases. This approach also removes the effects of different ray parameters (p) on the moveout of the listed P-to-S converted phases. Based on many trials in our slant stacking analysis, we found that the most suitable weighting factors that balance the contribution of each phase were 0.40, 0.35, and 0.25 for w_1, w_2, and w_3, respectively. These weights were proportional to the signal/noise ratios for the three phases. We used the same weighting factors for most of the stations in this study. When certain phases were not observed, we were forced to modify our default weighting factors. In these few cases we used weightings of 0.8, 0.0, 0.2 for w_1, w_2, w_3, respectively. We have documented these special cases in the Results section.

We have used the bootstrap re-sampling technique to test the stability of our slant stacking results. We re-sampled our data by randomly selecting individual receiver functions to create a set of 100 or more bootstrapped receiver function stacks. We used these bootstrapped receiver functions to estimate the 2 standard deviations for H and Vp/Vs for the trials. This approach was used for all 23 stations.

We have also used the grid search waveform modeling technique developed by Sandvol *et al*., 1998a to estimate shear wave velocity structure for seven stations, both to validate our results and to compare the results of the two techniques. The grid search technique searches over a wide range of model parameters in order to find the 1-D velocity model that optimally fits the radial receiver function waveforms. The number of model parameters is limited by assuming a Poisson ratio. This approach requires that a region of model parameter space be chosen for the grid search; typically we began with 2- 4 layers and increased the number of layers when it was required to reasonably fit the waveform. The range of model parameters that were used in the search was based on prior studies of the structure of the region and/or through trial and error. This modeling technique uses a reflectivity synthetic seismogram algorithm, initially developed by Kennett (1984), to generate synthetic receiver functions that are compared with observed stacked receiver functions. The best fit is found by minimizing the least square difference between the observed and the synthetic receiver functions.

In order to test the stability of our grid search solutions, we performed a jackknife data re-sampling for the FRSS, KBRS, and TAYS receiver functions. This technique has the advantage of not requiring the estimation of a noise time series and also has been proven to yield unbiased and robust error estimates for nonlinear inversions (Tichelaar and Ruff, 1989; Efron and Tibshirani, 1991). However, neither of our resampling error estimation techniques is sensitive to systematic errors in the data. One way to overcome this drawback is comparison of our Moho depths with other published results in the region.

RESULTS

We have organized our discussion of our results into four groups based on the tectonic environment and location. These four regions include the Arabian shield (specifically stations KBRS, TBKS, NAMS, HILS, BLJS, DJNS, TATS, ARSS, AFFS), the Gulf of Aqaba (specifically stations AYUS, BDAS, TAYS, HAQS, ALWS, JMQS, JMQS, HITJ), the Arabian platform (stations HASS, RUWJ, QURS), and the Red Sea (stations FRSS, YNBS, LTHS). Our results for all the stations are listed in Table 2.1. We will also show the results for all stations in a special web site.

Stations within the Arabian shield

KBRS: In general, the Arabian shield stations are characterized by lower noise than the other stations in the Arabian Peninsula. We slant stacked 30 receiver functions (Figure 2.4b) in order to find the bulk crustal thickness and crustal Vp/Vs. We observed clear arrivals of PS_{Moho} and multiples at KBRS (Figure 2.4c). We estimated a Moho depth of 35.2 km and a Vp/Vs of 1.75. We have also performed a 4 layer grid search inversion for KBRS and we obtained a 35.5 km (Figure 2.4e) depth for the Moho using the grid search (Figure 2.4d, e). The two values for the Moho depth are extremely close, probably owing to the nearly 1-D velocity structure beneath this station. The 2 standard deviation (STD) for 100 bootstrap error analysis shows ± 1.0 km in Moho depth and ± 0.038 for the Vp/Vs.

TBKS: We have good azimuthal coverage for this station (Figure 2.5a). We observed a clear crossing of Moho phase and multiples from the slant stacking of 32 receiver functions (Figure 2.5b, c). We observed a clear multiple at 8 seconds, labeled as Pxs in Figure 2.5c, for events with a distance range of greater than 60º. This arrival could be associated to a velocity discontinuity at a depth of about 75 km.

NAMS: NAMS is located in the western part of the shield along the 2 km escarpment. From the slant stacking of 42 receiver functions we observed a crustal thickness of 42 ± 2 km with a Vp/Vs of 1.69 ± 0.03 (Figure 2.6). We also noticed a coherent multiple around 2 seconds, labeled Pxs in Figure 2.6c, which could be due to a major mid crustal discontinuity at about 16 km depth.

HILS: This is one of the best stations used in this study. We have been able to utilize 55 receiver functions for the slant stacking approach (Figure 2.7a, b). We estimate the Moho depth to be 36.9 ± 1.0 km with a Vp/Vs of 1.78 ± 0.02 (Figure 2.7c). Although these error values cannot be used as an absolute error in Moho depth, the values reflect the quality and the coherency of the data used. We have also performed grid search inversion over 4 layers for HILS and we obtained a Moho depth of 39.5 km, which is

Figure 2.4. a) A map showing the epicenters (open circles) for the earthquakes corresponding to the slant stacked receiver functions in (b). The recording station KBRS is shown by a solid triangle. b) Receiver functions corresponding to the earthquakes in (a). The two columns represent the distance (Δ) and the azimuth (AZ) in degrees for the corresponding earthquake. c) H vs Vp/Vs plot showing our estimated Moho depth (+) and the bootstrap error analysis results (x). d) The resulting waveform synthetic fit (dashed line) using the grid search technique and the observed stacked receiver functions (solid line). e) Jackknife shear velocity models obtained from re-sampled receiver function stacks. A dark line indicates the mean model. Thin lines indicate the maximum and minimum models. The slant stacking and grid search Moho depth estimates are almost identical.

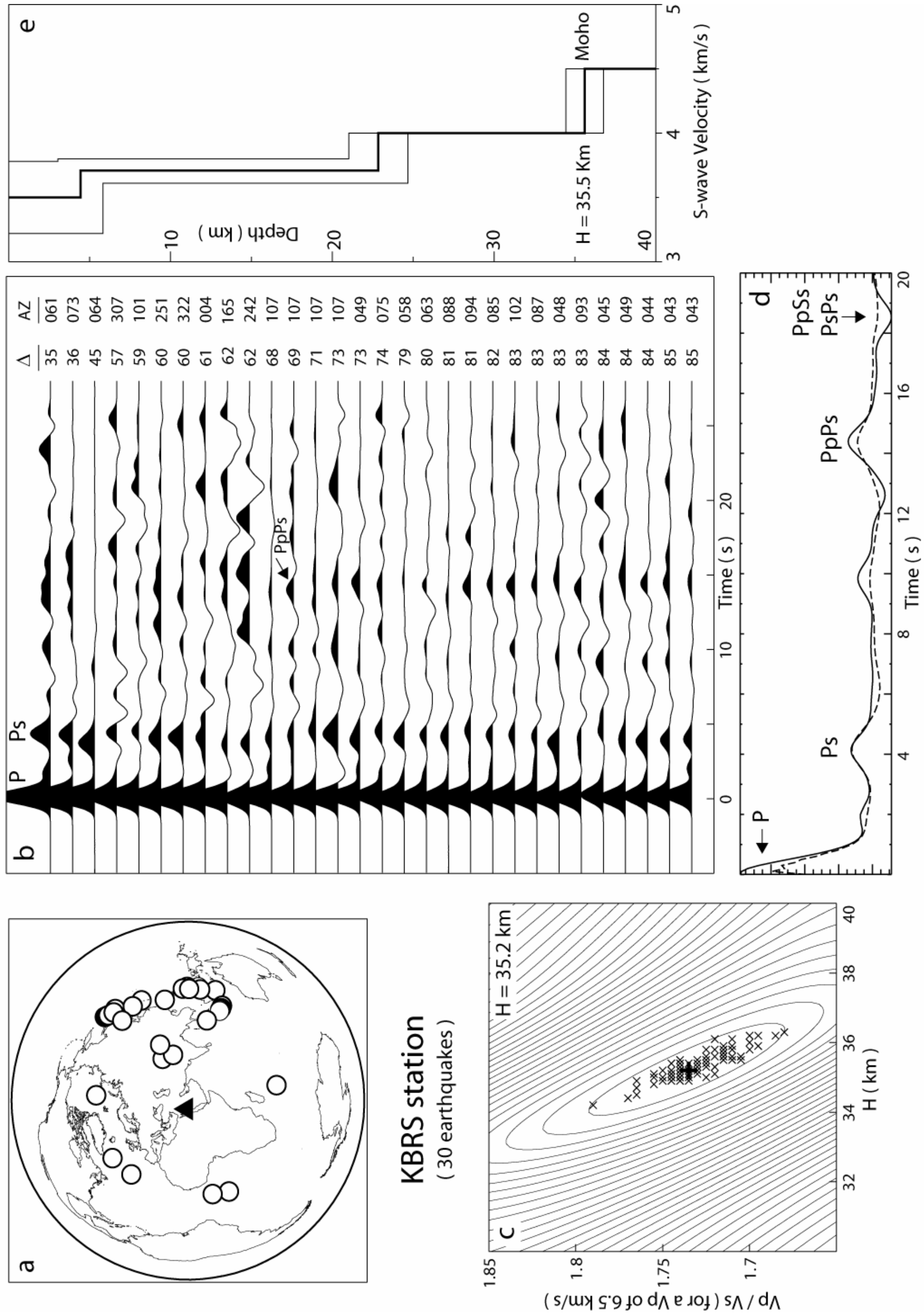
a
KBRS station
(30 earthquakes)
b
P
Ps
PpPs
Δ
AZ
Time (s)
c
H = 35.2 km
H (km)
Vp / Vs (for a Vp of 6.5 km/s)
d
P
Ps
PpPs
PsPs
PpSs
Time (s)
e
Moho
H = 35.5 Km
Depth (km)
S-wave Velocity (km/s)

in very close agreement with our slant stacking result. We expect the difference to be caused by the sampling of the grid search compared to utilizing the whole data set in slant stacking.

Crustal thickness results for other stations in the shield including BLJS, DJNS, TATS, ARSS, and AFFS are listed in Table 2.1 and shown in Figure 2.2 and 2.12. We observed complex receiver function waveforms at DJNS. We applied both slant stacking and grid search techniques to obtain a Moho depth of 44 km and 47 km, respectively. Higher than average Vp/Vs rations of 1.83 for the slant stacking and 1.8 for the grid search were also observed. We suspect that the complexity in the receiver function may be due to the lateral variations in the velocity structure originating from the nearby active volcanic centers. We observed a coherent multiple arriving before the Moho phase (around 2-3 seconds) at TATS. We expect the multiple to be caused by a mid crustal discontinuity beneath TATS. We found a 32 km Moho depth at AFFS. This is inconsistent with prior published results (Sandvol *et al*., 1998b) (see Table 2.2); this may be due to damage, which has occurred to this station.

Stations around the Gulf of Aqaba

TAYS: We have been able to stack 30 receiver functions for TAYS (Figure 2.8a, b). We observed a coherent PS_{Moho} (Figure 2.8b) arrival and based on the slant stacking of the PS_{Moho} and multiples, we estimated a Moho depth of 28.2 ± 1.9 km with a Vp/Vs of 1.72 ± 0.06 for TAYS (Figure 2.8c). Our grid search modeling results (Figure 2.8d, e) indicated a 29.5 ± 2.4 km for the Moho, which is consistent with our slant stacking Moho depth.

Our results for other Gulf of Aqaba stations (ALWS, HAQS, AYUS, BDAS, JMOS, JMQS, and HITJ) are listed in Table 2.1 and shown in Figure 2.2 and 2.12. In the following we briefly highlight some of the more important observations.

Figure 2.5. a) A map showing the epicenters (open circles) for the earthquakes used in the slant stacked receiver functions in (b). The recording station TBKS is shown by a solid triangle. b) Receiver functions corresponding to the earthquakes in (a). The two columns represent the distance (Δ) and the azimuth (AZ) in degrees for the corresponding earthquake. c) H vs Vp/Vs plot showing our estimated Moho depth (+) and the bootstrap error analysis results (x). d) The resulting waveform synthetic fit (dashed line) using the grid search technique and the observed stacked receiver functions (solid line). e) Jackknife shear velocity models obtained from re-sampled receiver function stacks. A dark line indicates the mean model and the thin lines indicate the maximum and minimum models.

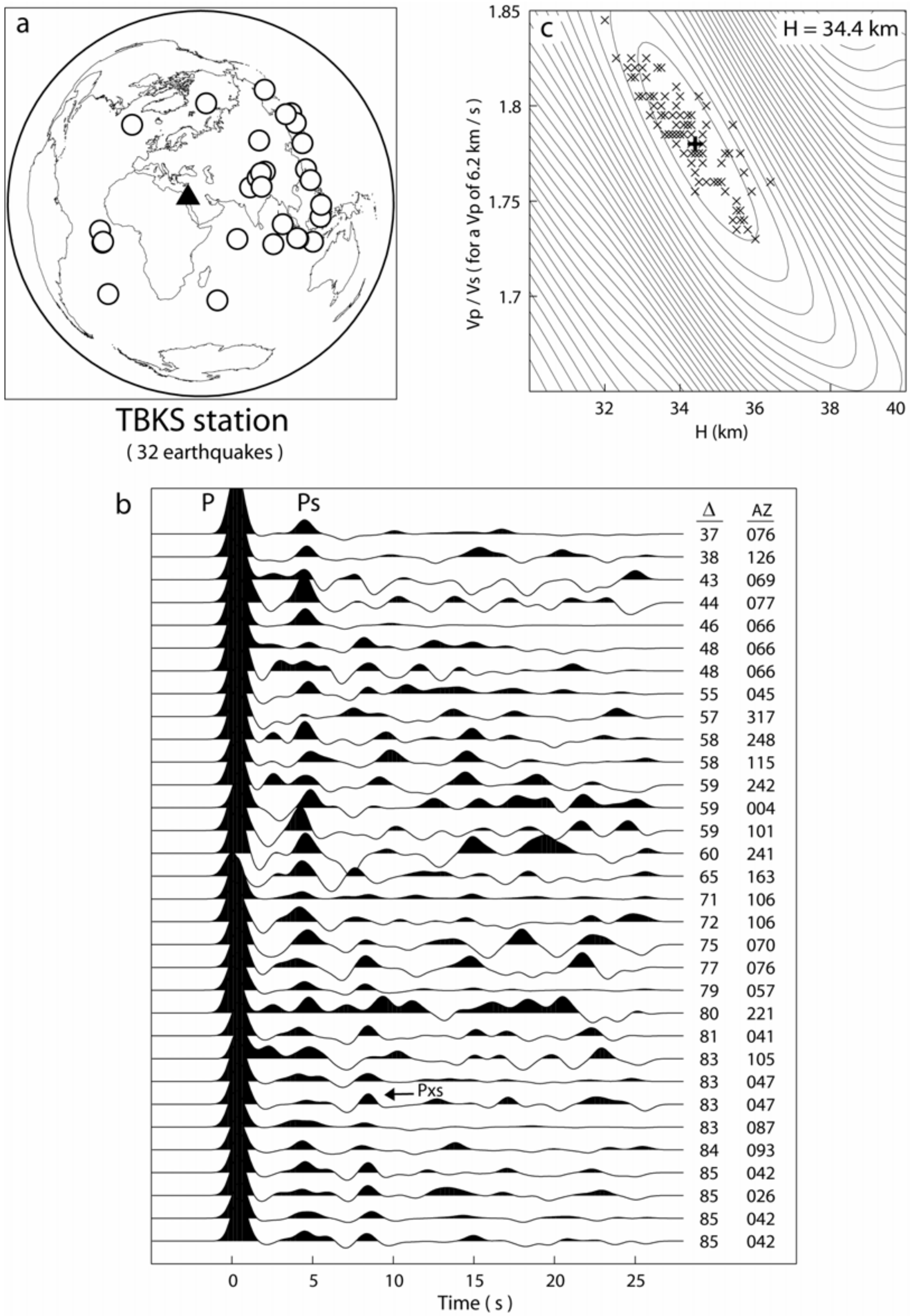
a
TBKS station
(32 earthquakes)
c
H = 34.4 km
Vp / Vs (for a Vp of 6.2 km / s)
H (km)
b
P
Ps
Pxs
Δ
AZ
Time (s)

Figure 2.6. a) A map showing the epicenters (open circles) for the earthquakes used in the slant stacked receiver functions in (b). The recording station NAMS is shown by a solid triangle. b) Receiver functions corresponding to the earthquakes in (a). The two columns represent the distance (Δ) and the azimuth (AZ) in degrees for the corresponding earthquake. A clear and consistent mid-crustal discontinuity is marked by Pxs. c) H vs Vp/Vs plot showing our estimated Moho depth (+) and the bootstrap error analysis results (x). d) The resulting waveform synthetic fit (dashed line) using the grid search technique and the observed stacked receiver functions (solid line). e) Jackknife shear velocity models obtained from re-sampled receiver function stacks. A dark line indicates the mean model and the thin lines indicate the maximum and minimum models. We observed a dramatic change in crustal thickness between FRSS (Figure 2.9) and NAMS.

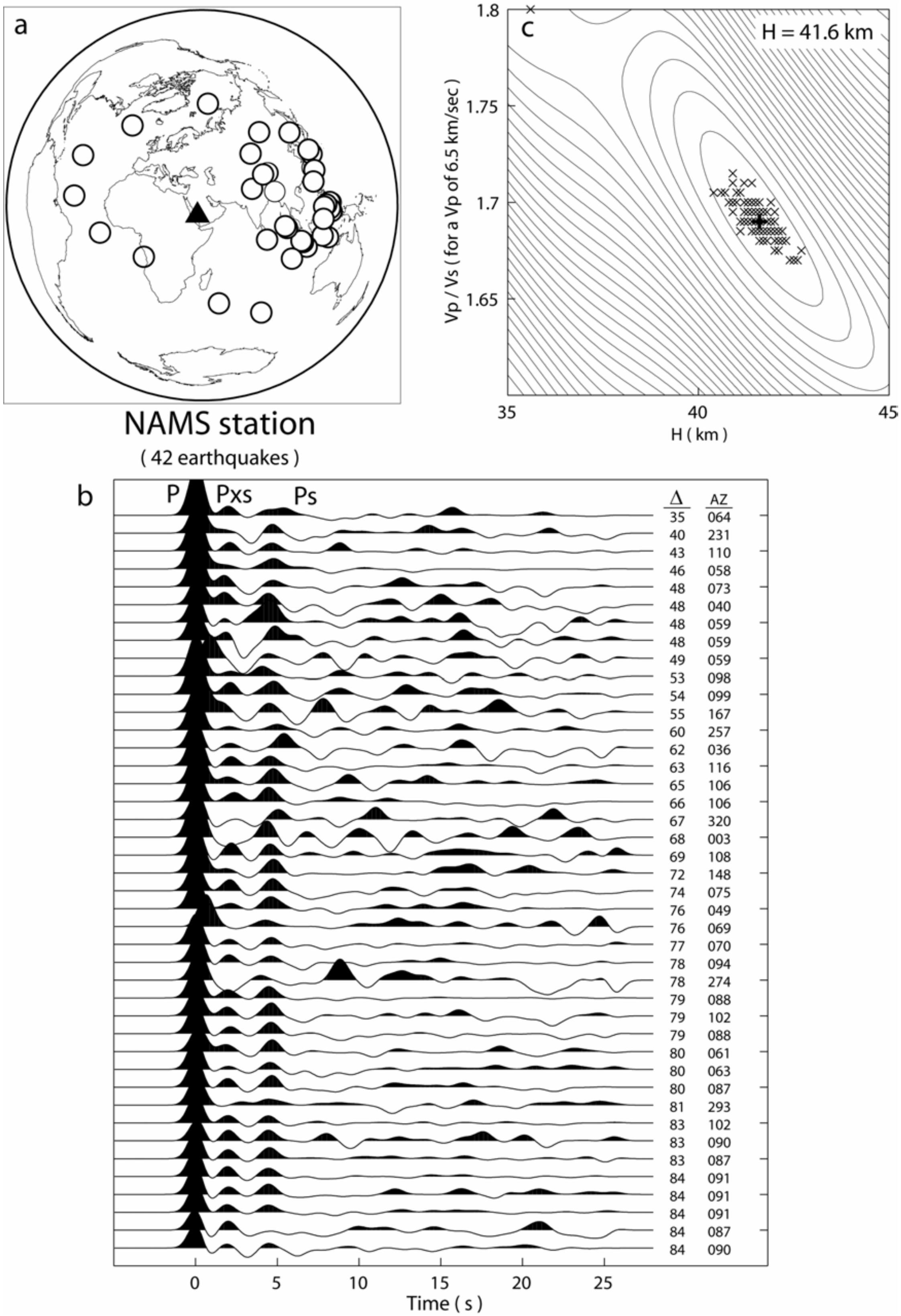

a
NAMS station
(42 earthquakes)
b
P
Pxs
Ps
Δ
AZ
35 064
40 231
43 110
46 058
48 073
48 040
48 059
48 059
49 059
53 098
54 099
55 167
60 257
62 036
63 116
65 106
66 106
67 320
68 003
69 108
72 148
74 075
76 049
76 069
77 070
78 094
78 274
79 088
79 102
79 088
80 061
80 063
80 087
81 293
83 102
83 090
83 087
84 091
84 091
84 091
84 087
84 090
0
5
10
15
20
25
Time (s)
c
H = 41.6 km
Vp / Vs (for a Vp of 6.5 km/sec)
1.8
1.75
1.7
1.65
35
40
45
H (km)

Figure 2.7. a) A map showing the epicenters (open circles) for the earthquakes used in the slant stacked receiver functions in (b). The recording station HILS is shown by a solid triangle. b) Receiver functions corresponding to the earthquakes in (a). The two columns represent the distance (Δ) and the azimuth (AZ) in degrees for the corresponding earthquake. This is a shield station and one of the best stations in terms of noise level and the running time.

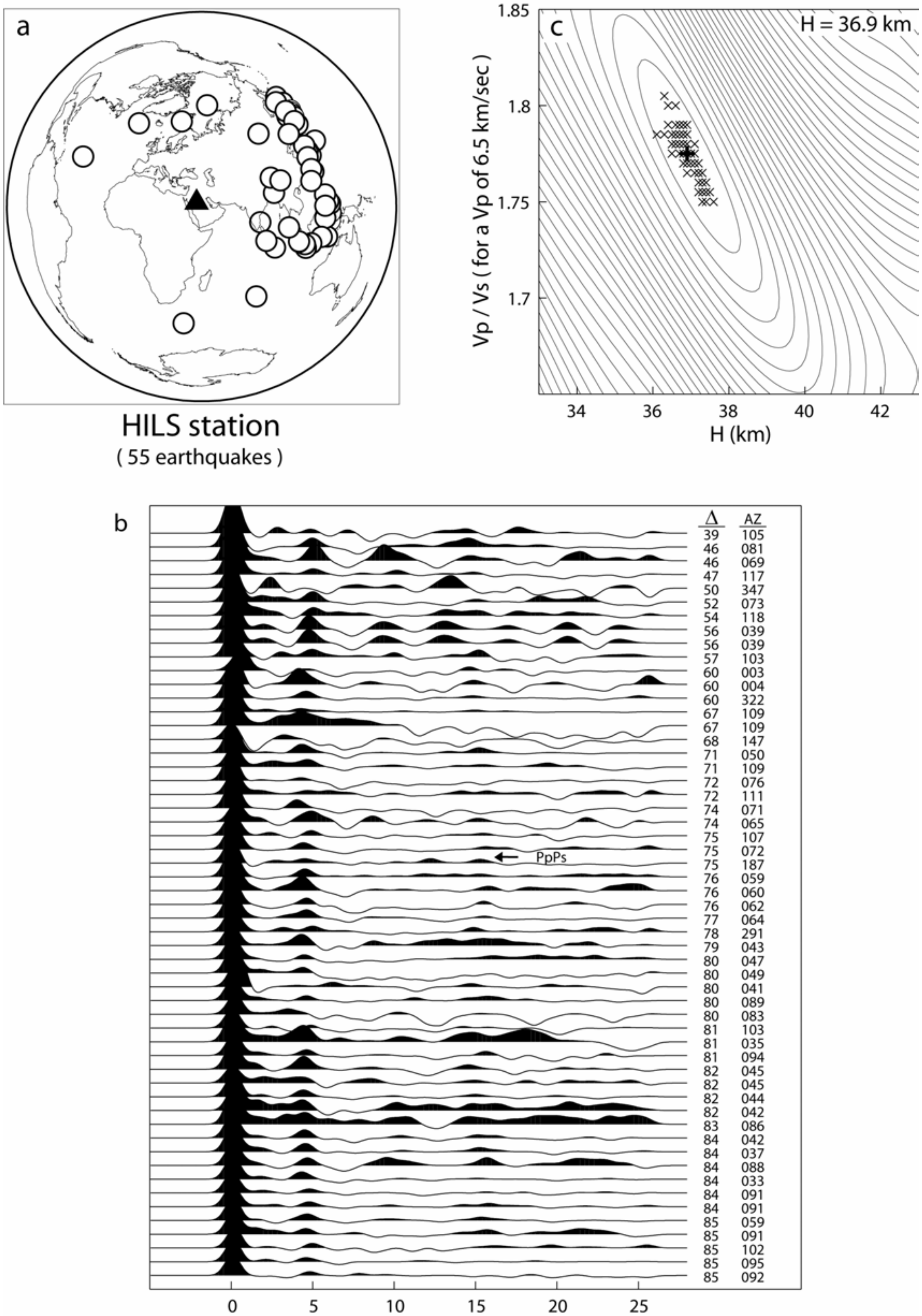
a
HILS station
(55 earthquakes)
c
H = 36.9 km
Vp / Vs (for a Vp of 6.5 km/sec)
H (km)
b
Δ
AZ
PpPs

Figure 2.8. a) Map showing the epicenters (open circles) for the earthquakes used in the slant stacked receiver functions in (b). The recording station TAYS is shown by a solid triangle. b) Receiver functions corresponding to the earthquakes in (a). The two columns represent the distance (Δ) and the azimuth (AZ) in degrees for the corresponding earthquake. c) H vs Vp/Vs plot showing our estimated Moho depth (+) and the bootstrap error analysis results (x). d) The resulting waveform synthetic fit (dashed line) using the grid search technique and the observed stacked receiver functions (solid line). e) Jackknife shear velocity models obtained from re-sampled receiver function stacks. The dark line indicates the mean model and the thin lines indicate the maximum and minimum models. Thinner crust has been observed along Gulf of Aqaba compared to the shield and platform. We observed good agreement in Moho depth between the slant stacking and the grid search results.

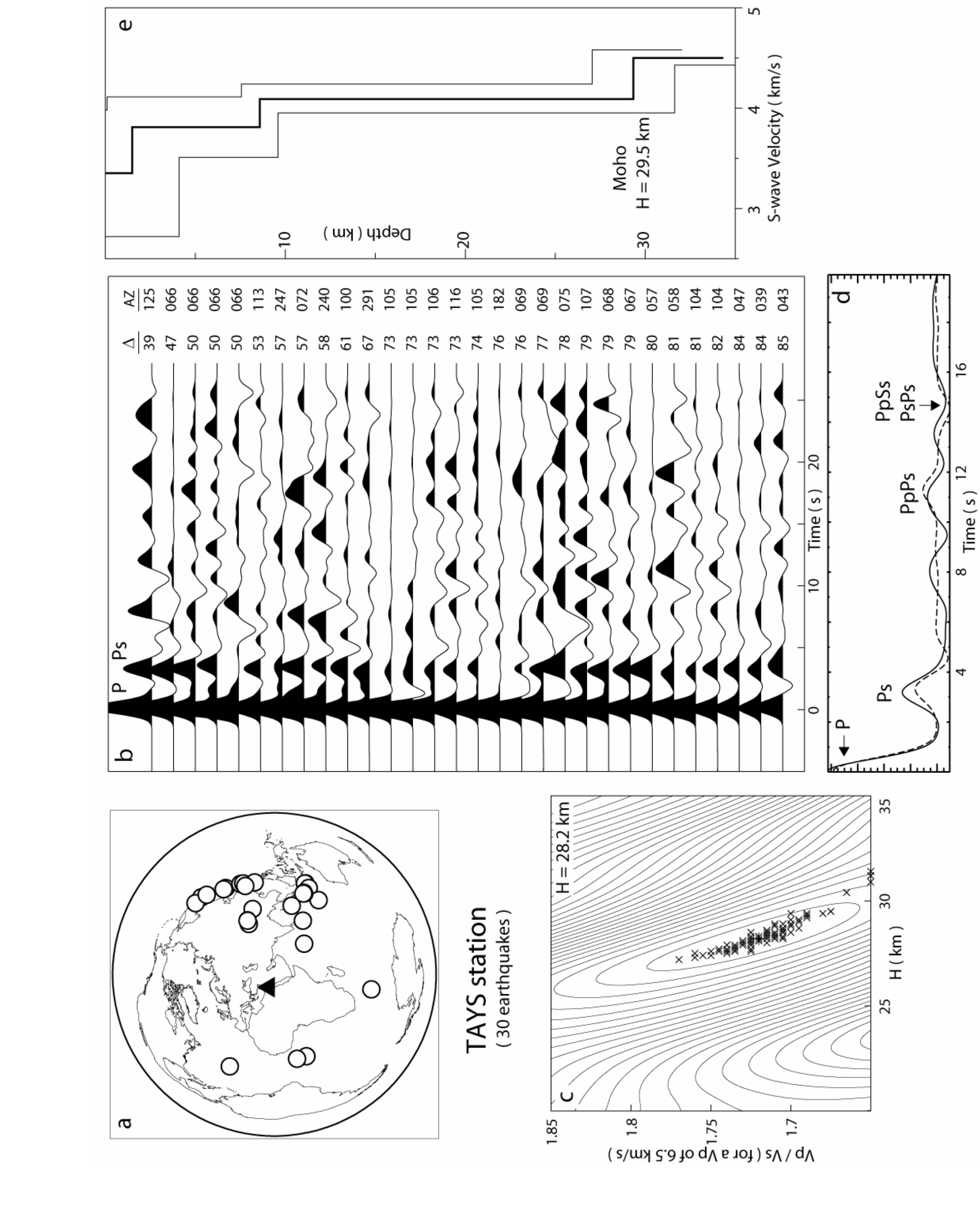
a
TAYS station
(30 earthquakes)
b
P
Ps
Δ
AZ
Time (s)
c
H = 28.2 km
Vp / Vs (for a Vp of 6.5 km/s)
H (km)
d
P
Ps
PpPs
PpSs
PsPs
Time (s)
e
Depth (km)
Moho
H = 29.5 km
S-wave Velocity (km/s)

For example, we observed a coherent multiple around 7-8 seconds regardless of distance or azimuth at ALWS station. Also, our slant stacking result shows less control over Vp/Vs than over Moho depth, which could possibly be due to the thin crust under the station. Due to the high noise level at HAQS station, we were able to only find 11 receiver functions with signal to noise ratios greater than 2. We observed a Moho depth that is consistent with other Gulf of Aqaba stations. We also observed a larger delay in the Moho phase for earthquakes south/southeast of the station, possibly indicating thicker crust in that direction. The Vp/Vs value at AYUS (Table 2.1) is lower than that of other Gulf of Aqaba stations and could be associated with the high level of noise and limited azimuthal coverage at this station. Although our Moho depth result at JMOS is consistent with other Gulf of Aqaba stations, the Vp/Vs value is surprisingly high. This station is close in location to ALWS (Figure 2.2). Both stations have high Vp/Vs values that suggest these results may be reliable. The crust at JMQS station is 36.6 ± 1.5 km. This station is located east of the other Gulf of Aqaba stations (Figure 2.12) and the Moho depth indicates that the crust is thickening to within normal shield or platform crust. We observed a Moho depth of 36.4 ± 1.4 km at HITJ. Similar to JMQS we believe the crustal thickness at HITJ is thickening to within normal platform crust. Rodgers *et al*., 2003 observed a crustal thickness of 36 km for HITJ that is consistent with our results.

Stations along the Red Sea

FRSS: This station is located on a small island near the eastern Red Sea coast (Figure 2.2). The island marks the end point for the deep seismic profile that was interpreted by Mooney *et al*., 1985. We found 24 receiver functions corresponding to events east, southeast, and northwest of the station (Figure 2.9a, b). In our slant stacking we did not observe PS_{Moho} and Moho multiples crossing. Because of that, we stacked the data for PS_{Moho} and PpSs+PsPs phases with weighing of 0.8 and 0.2 respectively. Our slant stacking result is shown in Figure 2.9c. We found a Moho depth of 14± 1 km and a Vp/Vs of 1.7 ± 0.09 for this station. We have also used the grid search technique to model the receiver function stack for this station. Our grid search results are shown in Figure 2.9d, e. We found the best model to consist of 4 layers with a Moho depth of 11 km and an error of 1.2 km. We observed a coherent arrival at 11 seconds, labeled Pxs in Figure 2.9b, that we associated to a velocity discontinuity at about 102 km.

Results for other Red Sea stations (YNBS and LTHS) are listed in Table 2.1 and shown in Figure 2.2 and 2.12. In the following we briefly highlighted the more important results. Trying to estimate the Moho depth for YNBS station, we encountered some problems with both the slant stacking and grid search techniques. In our slant stacking we did not observe PS_{Moho} and Moho multiples crossing. Because of that, we stacked the data for PS_{Moho} and PpSs+PsPs phases with weighting of 0.8 and 0.2, respectively. We estimated the Moho depth and the Vp/Vs to be 31.6 ± 3.42 km and 1.7 ± 0.082, respectively. Using our grid search technique we found the optimal model to consist of 5 layers with a Moho depth of 28 km. Although we encountered problems in both techniques, their Moho depth values are consistent. As for LTHS, our results are consistent with the nearby station YNBS (see above). Similar to YNBS we did not observe PS_{Moho} and Moho multiples crossing and we used similar weights for the slant stacking. We estimated the Moho depth for LTHS to be 22.2 ± 1.9 km with a Vp/Vs of 1.74 ± 0.07.

Stations within the Arabian platform

HASS: This station is located in the eastern part of the Arabian platform close to the

Figure 2.9. a) A map showing the epicenters (open circles) for the earthquakes used in the slant stacked receiver functions in (b). The recording station FRSS is shown by a solid triangle. b) Receiver functions corresponding to the earthquakes in (a). The two columns represent the distance (Δ) and the azimuth (AZ) in degrees for the corresponding earthquake. c) H vs Vp/Vs plot showing our estimated Moho depth (+) and the bootstrap error analysis results (x). d) The resulting waveform synthetic fit (dashed line) using the grid search technique and the observed stacked receiver functions (solid line). e) Jackknife shear velocity models obtained from re-sampled receiver function stacks. The dark line indicates the mean model and the thin lines indicate the maximum and minimum models. The crustal thickness is very thin near the eastern coast of the Red Sea.

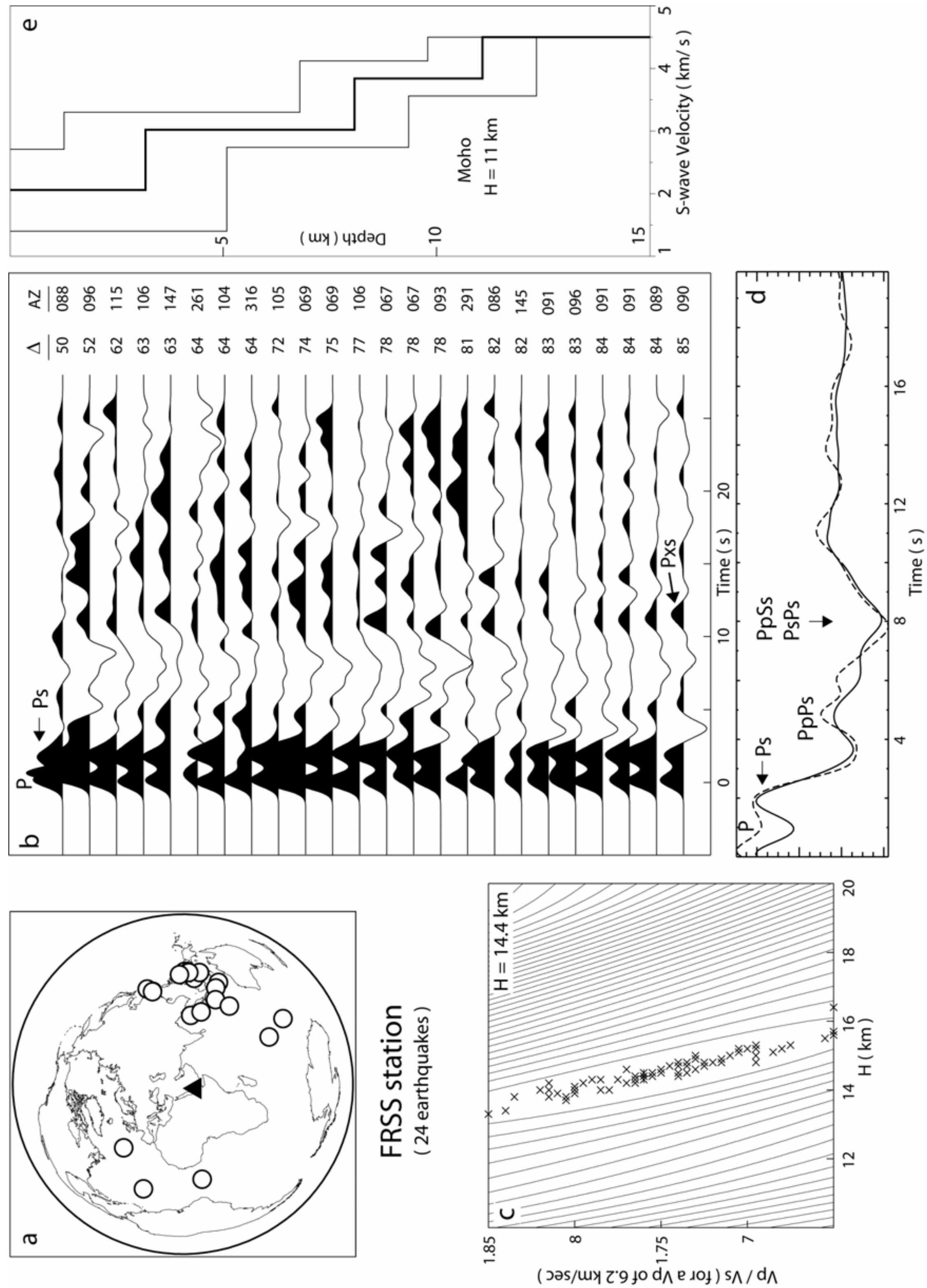

a
FRSS station
(24 earthquakes)
b
P
Ps
Pxs
Time (s)
Δ
AZ
c
H = 14.4 km
H (km)
Vp / Vs (for a Vp of 6.2 km/sec)
d
PpPs
PpSs
PsPs
Time (s)
e
Moho
H = 11 km
Depth (km)
S-wave Velocity (km/ s)

Arabian/Persian Gulf. We observed a near direct P arrival (a secondary arrival that was shifted ~ 0.75 second from the main peak), which we believe can be associated to a relatively thick (~ 8 km) sedimentary layer over the metamorphic basement (see Figure 2.10). Compared to other stations used in this study, HASS receiver functions are complicated. For example, although the Moho phase was coherent and clear, it was longer period than the other phases. Also, later arriving crustal multiples (PpPs and PsPs+PpSs) were sometimes absent or masked by noise. Our slant stacking result for HASS indicated a 41 ± 0.5 km Moho depth with 1.81 ± 0.02 Vp/Vs. Based on PS_{Moho} delay time, regional tectonics, and previous studies we believe that the crust should be thicker and the Vp/Vs value we found is high. In fact when we stacked our data for different distances we came up with an average 5 second PS_{Moho} delay corresponding to 45 – 50 km Moho depth. Although we tested our data for azimuthal and distance variations, we were not able to observe any azimuthal dependence in the receiver function waveforms. We also performed grid search modeling over a large number of model parameters (2 to 6 layers, with both Vp and Vp/Vs varying); we found that the best model to fit HASS waveform data consists of 4 layers of crust with a total thickness of 53 km (Figure 2.10d). We believe that the main reasons for the complicated receiver functions could be the interference of the PS_{Moho} phase with multiples from the sedimentary layer(s).

RUWJ: This station is located in northeast Jordan. We estimated a Moho depth of 37.2 ± 0.8 km for RUWJ with a Vp/Vs of 1.78 ± 0.02 (Figure 2.11). Our observation is consistent with previous seismic and gravity results (El-Isa *et al*., 1987; Sandvol *et al*., 1998a). Although Rodgers *et al*., 2003 were not able to model the receiver function for this station probably due to near-surface site effects and sediments of the northern Arabian platform, we observed a very clear PS_{Moho} and multiples crossing. In fact we believe the station to be one of the best stations used in our slant stack. We also noticed a coherent multiple around 2 seconds, labeled Pxs (Figure 2.11b), which could be due to a mid crustal discontinuity at about 13 km depth.

QURS: We have difficulty in slant stacking events for QURS station. We find a slightly thinner crust and lower Vp/Vs at QURS than at RUWJ. We estimated the depth to Moho at QURS to be around 32.4 km with Vp/Vs of 1.71. Our 2 STD bootstrap errors for the Moho depth and Vp/Vs were ± 4.5 km and ± 0.1, respectively.

We have also included the results of Sandvol *et al*., 1998a, 1998b and Al-Lazki *et al*., 2002 in our study (Table 2.2). All the Moho depth results are shown in Figure 2.12 with the estimated errors. In general, the average crustal thickness for the shield stations is 39 km. Along the escarpment in western Arabia the average Moho depth is 40 km. The average Moho depth for the Gulf of Aqaba stations is 29 km, while along the Red Sea coast it is about 23 km. We observed shallower Moho for stations along the Red Sea and Gulf of Aqaba than in the shield. The change in Moho depth becomes more pronounced when we compare stations LTHS and TAIF or especially FRSS and DJNS (see Figure 2.2 and 2.12) where a change of about 25 km in Moho depth occurs in a distance of less than 200 km. Towards the east we observed a slight thickening of the crust near the platform, where the Moho depth reaches about 44 km. Our observations in the shield are consistent with previous studies of Mooney *et al*., 1985 and Sandvol *et al*., 1998b. In the northern part of the platform, the crust varies from 33 to 37 km; this is less than the average crust of the shield. The observed Moho depths in Oman, which varies between 41-49 km, and HASS station (see Figure 2.2

Figure 2.10. a) A map showing the epicenters (open circles) for the earthquakes used in the slant stacking of receiver functions in (b). The station HASS is shown by a solid triangle. b) Receiver functions corresponding to the earthquakes in (a). c) H vs Vp/Vs plot showing our estimated Moho depth (+) and the bootstrap error analysis results (x). d) The resulting waveform synthetic fit (dashed line) using the grid search technique and the observed stacked receiver functions (solid line). We had difficulty in modeling and slant stacking the receiver function results for station HASS. Both methods give results varying from 41 km to 53 km, with poor fit for the grid search as well as extremely high Vp/Vs values for the slant stack.

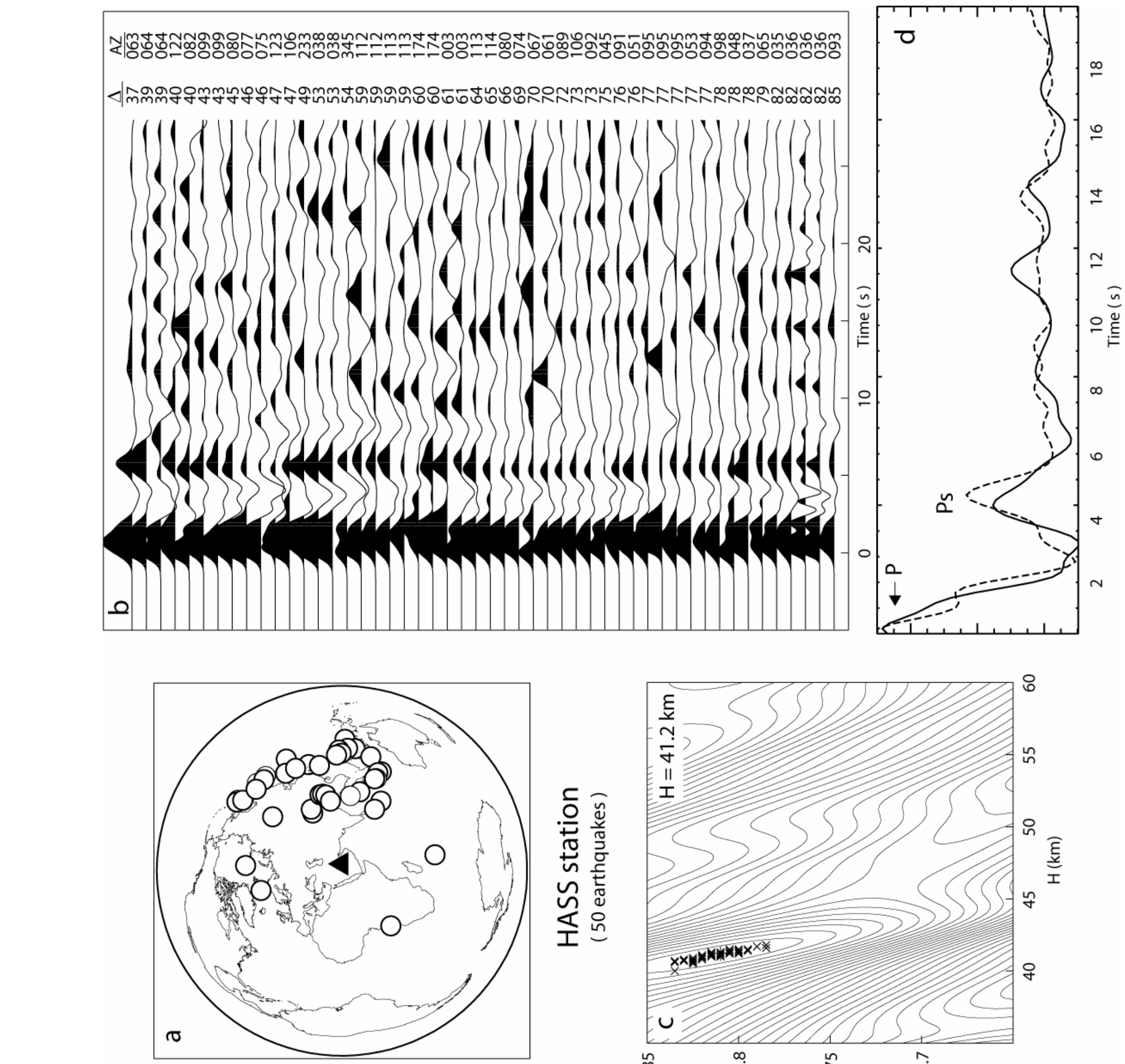
a
HASS station
(50 earthquakes)
b
Δ
AZ
Time (s)
c
H = 41.2 km
H (km)
Vp / Vs (for a Vp of 6.30 km / sec)
d
P
Ps
Time (s)

Figure 2.11. a) A map showing the epicenters (open circles) for the earthquakes used in the slant stacked receiver functions in (b). The recording station RUWJ is shown by a solid triangle. b) Receiver functions corresponding to the earthquakes in (a). The two columns represent the distance (Δ) and the azimuth (AZ) in degrees for the corresponding earthquake. We observed a mid-crustal discontinuity (probably corresponding to the base of the sedimentary layer) shown by Pxs. c) H vs Vp/Vs plot showing our estimated Moho depth (+) and the bootstrap error analysis results (x).

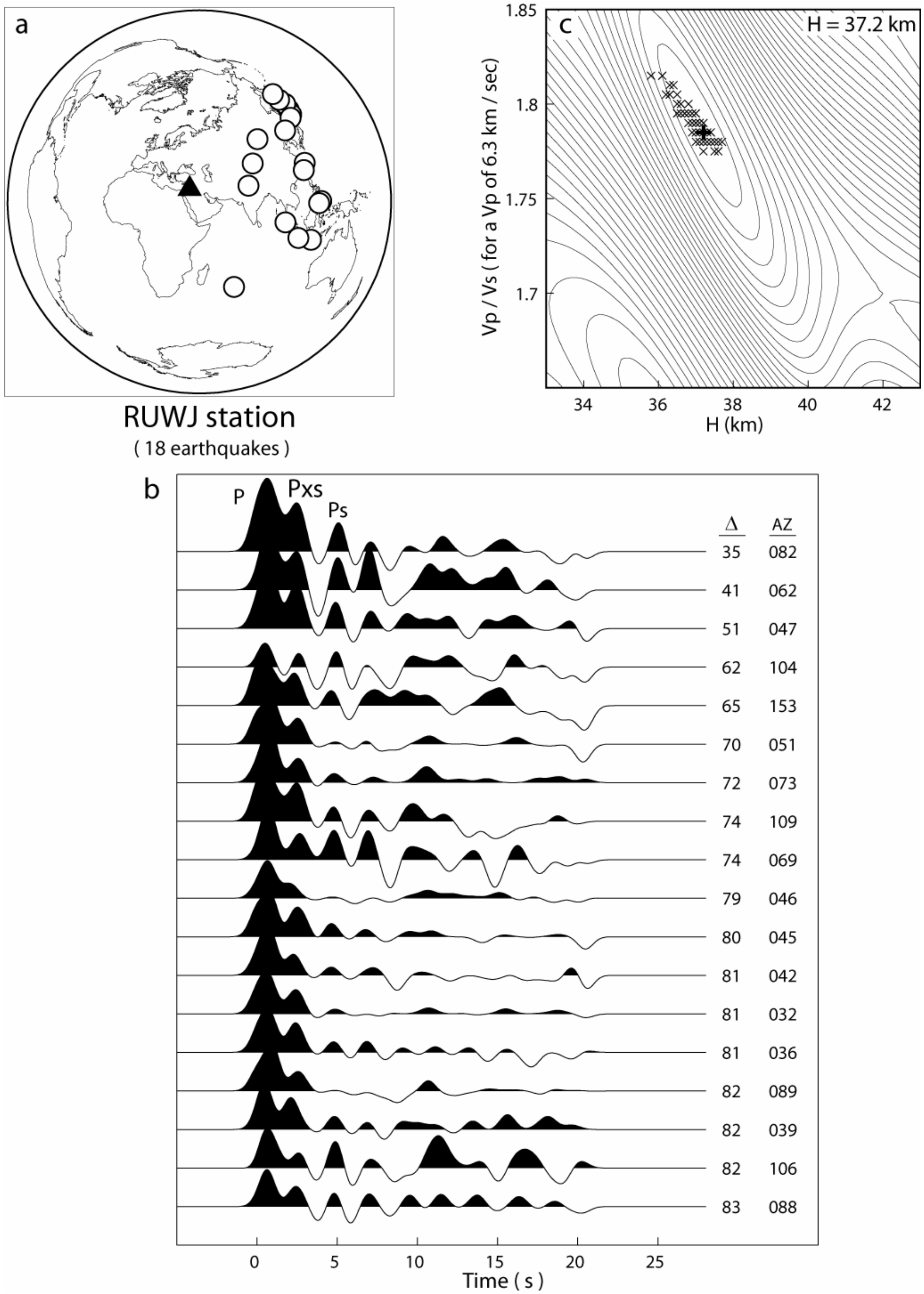
a
RUWJ station
(18 earthquakes)
c
H = 37.2 km
Vp / Vs (for a Vp of 6.3 km / sec)
1.85
1.8
1.75
1.7
34
36
38
40
42
H (km)
b
P
Pxs
Ps
Δ
AZ
35 082
41 062
51 047
62 104
65 153
70 051
72 073
74 109
74 069
79 046
80 045
81 042
81 032
81 036
82 089
82 039
82 106
83 088
0
5
10
15
20
25
Time (s)

Table 2.2. Moho depth estimates for seismic stations in the region based on receiver function results (after Sandvol *et al*., 1998a, 1998b and Al-Lazki *et al*., 2002).

	Station	Latitude (N)	Longitude (E)	Elevation (m)	Moho Depth (km)
1	AFIF	23.93	43.04	1116	39.0 ± 1.0
2	HALM	22.85	44.32	930	40.0 ± 1.0
3	RANI	21.31	42.78	1001	35.0 ± 2.5
4	RAYN	23.52	45.50	792	44.0 ± 2.5
5	RIYD	24.72	46.64	717	45.0 ± 2.0
6	SODA	18.29	42.38	2876	38.0 ± 1.0
7	TAIF	21.28	40.35	2050	40.5 ± 2.5
8	UQSK	25.79	42.36	950	37.0 ± 1.5
9	BGIO	31.72	35.09	752	33.0 ± 3.3
10	ATD	11.53	42.85	610	8.0 ± 1.5
11	KEG	29.93	31.83	460	33.0 ± 4.1
12	KTOM	23.48	57.69	107	41.0 ± 2.0
13	AWBI	23.30	57.53	397	19.0 ± 2.0
14	JBRN	22.91	57.26	552	43.0 ± 2.0

Figure 2.12. Moho depth results with error estimates for the 36 stations shown in Figure 2.2 plotted over a topography map. The thickest crust is along the Arabian shield escarpment. Thinner crust was observed along the Red Sea coast and Gulf of Aqaba. A dramatic change in Moho depth between stations along the Arabian shield escarpment and stations along the Red Sea coastline can be observed.

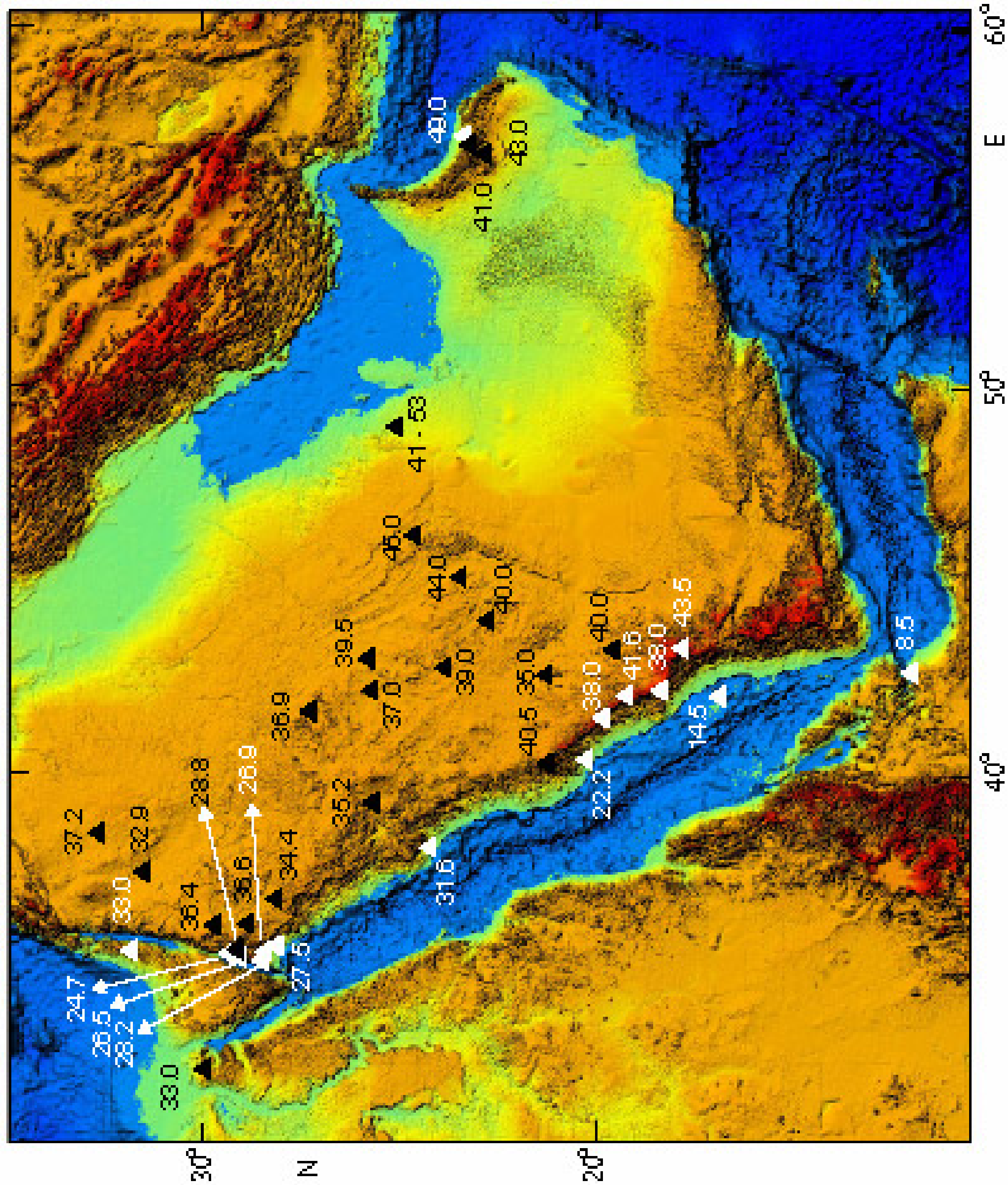
30°
20°
N
40°
50°
60°
E
37.2
32.9
33.0
36.4
35.6
34.4
28.8
26.9
24.7
26.5
28.2
33.0
27.5
35.2
31.6
36.9
39.5
37.0
39.0
45.0
44.0
40.0
41 - 53
35.0
40.5
22.2
38.0
41.6
40.0
43.5
14.5
8.5
41.0
43.0

and 2.12) seem to indicate that the crust in the southern part of the platform is thicker than the northern part. We consistently observed thin crust along the Red Sea and Gulf of Aqaba coasts that increases rapidly in thickness near the escarpment, after which the crustal thickness stabilizes and increases slightly near the eastern part of the shield.

DISCUSSION AND IMPLICATONS

The Moho depth values presented in Figure 2.12 represent the average measurements of crustal thickness under the respective seismic stations. To better visualize the results in a simple way we have contoured our observations. In general, there is not a unique set of contour lines for a given set of measurements, especially when the input data are sparse and/or not evenly distributed. In order to create a more objective Moho map we employed the kriging technique and the contour command available in ARC/INFO tools. Kriging our observations had a number of problems: the software cell size limitation's forced us to use a coarser cell size where the data are sparse; also there were difficulties in quantifying some of the parameters that are significant for contouring, for example, the tectonic history of the region. Since our observations are more dense in the Arabian shield and along the margins of the Red Sea and the Gulf of Aqaba, we limited our contouring only to these regions. To limit the kriging process from extending beyond the Red Sea, we assumed a 5 km Moho depth along the mid-ocean ridge in the central part of the Red Sea. Finally, we contoured the kriging output based on a 10 km interval. We also contoured our results manually by visual inspection taking into account the topography, bathymetry, and the tectonic history of the region. To minimize contouring uncertainties in the hand drawn process we did not require a specific contouring interval or continuous contour lines and, thus, most of the contour lines stop where there are no data.

Figure 2.13. Map showing our Moho depth contouring results. Stations are shown as open triangles. The contour lines based on the kriging approach are shown in gray and the hand drawn contour lines are shown in solid black. The figure shows also the outline of the Arabian shield (open small circles), the escarpment (long dashes), and the Red Sea ridge (small dashes).

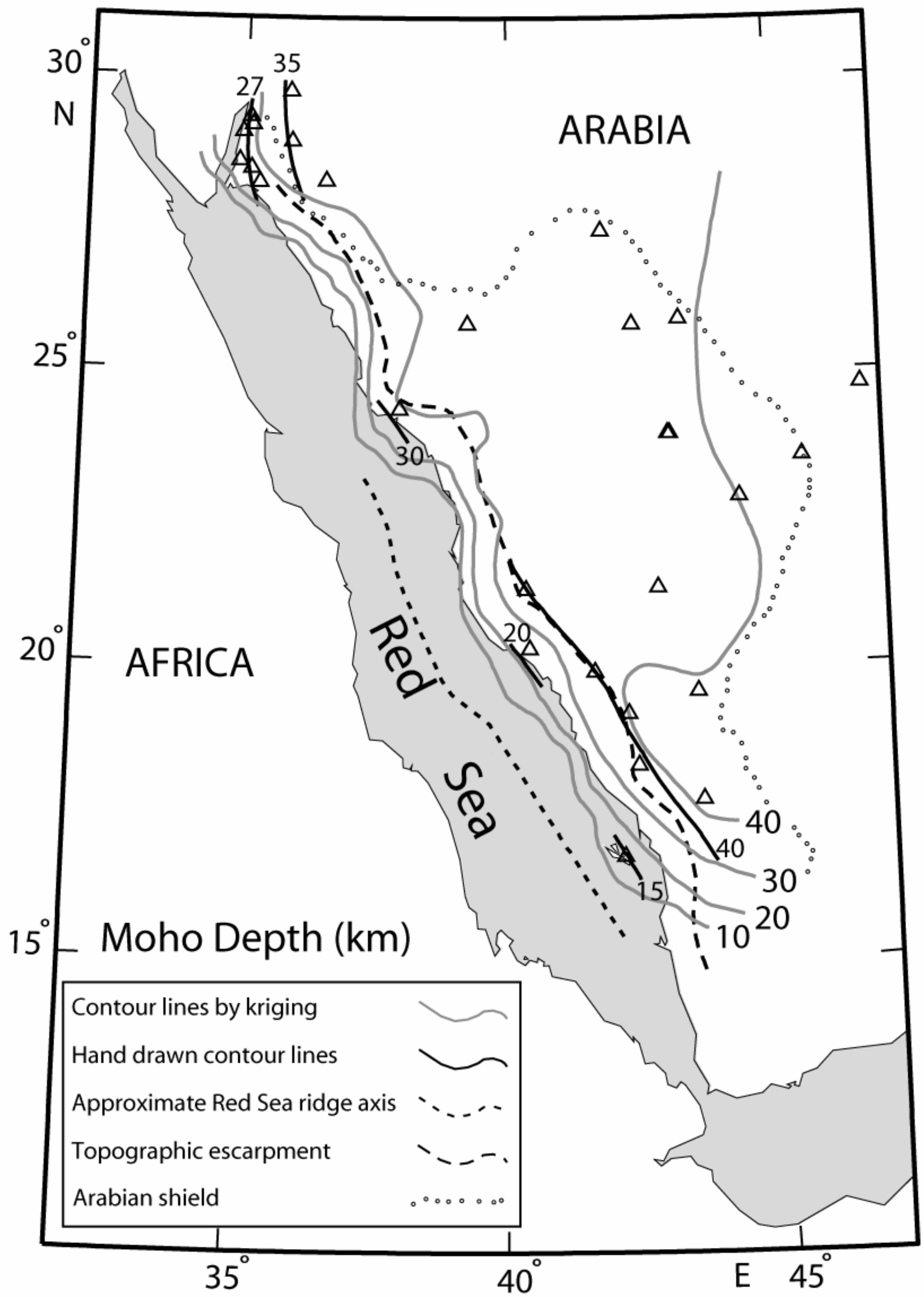
30°
N
25°
20°
15°
35°
40°
E
45°
ARABIA
AFRICA
Red
Sea
35
27
30
20
15
40
40
30
20
10
Moho Depth (km)
Contour lines by kriging
Hand drawn contour lines
Approximate Red Sea ridge axis
Topographic escarpment
Arabian shield

Our contouring results are shown in Figure 2.13. It is encouraging that contours based on the kriging technique are similar to those based on the visual, hand drawn process. However, the 40 km contour line based on the kriging technique deviates toward the interior of the shield because many Moho values are close to 40 km within the shield. The contour lines of both techniques show the dramatic change in crustal thickness between the topographic escarpment along the western margin of the Arabian shield and the shorelines of the Red Sea. On average the distance between the escarpment and the shorelines is approximately 65 km. Based on the contour map and the results in Tables 1 and 2, the Moho depth in the shield is relatively stable, and ranges between 35 and 45 km. The average Moho depth in the Arabian shield is 39 km.

Our results in the Arabian shield provide an excellent opportunity to compare Moho depth determinations for a relatively young, late Proterozoic shield to other determinations for other shield regions on earth. After a careful search of the available literature we identified nine Proterozoic and Archean shield regions that include reasonably well-determined Moho depths (Table 3). Most of these determinations are based on relatively recent research results using receiver functions. However, a few determinations are based on high-quality deep seismic (refraction) soundings (DSS). Crustal receiver function results can be considered an average measurement of Moho depth in proximity of a seismic station (~ 15 km), which is an advantage over the DSS method in which the Moho depth is more of an average over a relatively long path (> 150 km). When the average Moho depth (column 5 in Table 2.3) is not provided by the author(s), we averaged all shield receiver function results, and for the DSS results we averaged the minimum and maximum Moho depth along the seismic line.

We found that the average crustal thickness for all the studies in Table 3 is 39 km, while the average for Proterozoic shields is 40 km, and the average for Archean

Table 2.3. Moho depth and age for the Arabian shield and nine other shield regions collected from different reliable studies. The ages marked by * were obtained from Goodwin 1991. Most results are based on receiver functions (RF) and only a limited number are based on very reliable deep seismic soundings (DSS).

Shield	Survey Method	Age	Moho Depth (km)	Average Moho Depth (km)	Reference
Canada	RF	Archean (Slave) (> 2.6 Ga)	37-40	38	Bank et al., 2000
	RF	Archean (> 2.7 Ga) *	39-46	42	Darbyshire, 2003
	RF	Proterozoic(1.86) *	44	44	Darbyshire, 2003
	DSS	Archean (Slave) (> 2.6 Ga)	33	33	Viejo and Clowes, 2003
	DSS	Proterozoic (1.84 - 2.1 Ga)	32-35	33	Viejo and Clowes, 2003
Greenland	RF	Archean (2.5 - 3.8 Ga)*	40	40	Dahl-Jensen, 2003
	RF	Proterozoic (0.9 - 1.9 Ga)*	37-40	38	
Australia	RF	Archean (2.6 - 3.7 Ga) *	30-41	36	Chevrot and van der Hilst, 2000
	RF	Proterozoic (0.6 - 2.5 Ga) *	39-58	42	Chevrot and van der Hilst, 2000
	RF	Yilgarn Craton (Archean 2.6 - 3.7 Ga)	36-41	39	Reading et al., 2003
	RF	Pilbara Craton (Archean 2.7 - 3.6 Ga)	30-34	32	Reading and Kennett, 2003
Kaapvaal (South Africa)	RF	Archean (3.0 - 3.6 Ga)	37-40	38	Stankiewicz et al., 2003
	RF		35.4	35.4	Niu and James, 2002
	RF		34-44	38	Midzi and Ottemöller, 2001
	RF		35-40	38	Nguuri et al., 2001
West Siberia	DSS	Archean-Proterozoic (1.7 - 3.4 Ga) *	40-43	41	Pavlenkova et al., 2002
Brazil	RF	Archean (2.5 - 3.2 Ga)	37-44	40	Assumpucao, 2002
South India	RF	Archean (2.6 - 3.0 Ga)	36-39	38	Kumar et al., 2001
	DSS		37-40	38	Sarkar et al., 2001
Baltic	RF	Archean (1.9 - 2.9 Ga)	45-50	47	Alinaghi et al., 2002
	DSS		39-41	40	Berzin et al., 2002
North America	RF	Proterozoic (0.8 - 1.5 Ga)	38-49	43	Li et al., 2002
Arabia	RF	Proterozoic (0.7 - 1.2 Ga)	36-44	39	This study
	RF		35-44	39	Sandvol et al., 1998a
	DSS		38-43	40	Mooney et al., 1985

shields is 38 km. The Archean is slightly less thick than the Proterozoic crust. In general, we found that the crustal thickness of a Proterozoic shield to vary between 33 and 44 km, while in Archean shields it varies between 32 and 47 km. Figure 2.14 is a plot of the average Moho depth versus average age for all the studies presented in Table 3. Overall we do not observe a significant trend in the Moho depth with the average age of Precambrian crusts. That is, there is no significant difference between Proterozoic and Archean crustal thickness, and the variations we listed above for Moho depths lie within the margin of errors for these determinations. With the exception of young orogens, several authors have proposed general ascending relationship between crustal thickness and age (e.g., Meissner, 1986; Meissner and Wever, 1989); however, other authors (e.g., Durrheim and Mooney, 1991; Durrheim and Mooney, 1994) argued for thicker Proterozoic crusts in comparison to Archean shields. The results presented in Figure 2.14 are in contrast to the published results that suggest a relationship between the crustal thickness and the age of a given Precambrian crust. It appears that the average thickness of an Archean crust has not changed much relative to a Proterozoic crust, with an average thickness of about 40 km. This suggests that if Archean crust is subjected to deformation and/or magmatic episodes that resulted either in a thicker or thinner crust, then subsequent crustal processes such as crustal flow (e.g., Clark & Royden, 2000), crustal underplating (e.g., Nelson, 1991), or crustal delamination (Kay & Kay, 1993) tend to stabilize the crustal thickness back to about 40 km. Clearly more observations, especially in Proterozoic shields, are needed to draw any more firm conclusions regarding Precambrian crustal thickness.

In addition to contouring our Moho depth observations, we have projected our Moho depths along a cross section (Figure 2.15a) running from the Red Sea ridge to the Arabian/Persian Gulf. We have selected the location of this cross section to span a

Figure 2.14. A plot of average Moho depth results from different shield regions (see Table 1.3) versus the average age of the shield. Different symbols were used for age ranges. Lines connect the minimum and maximum Moho depth and age span.

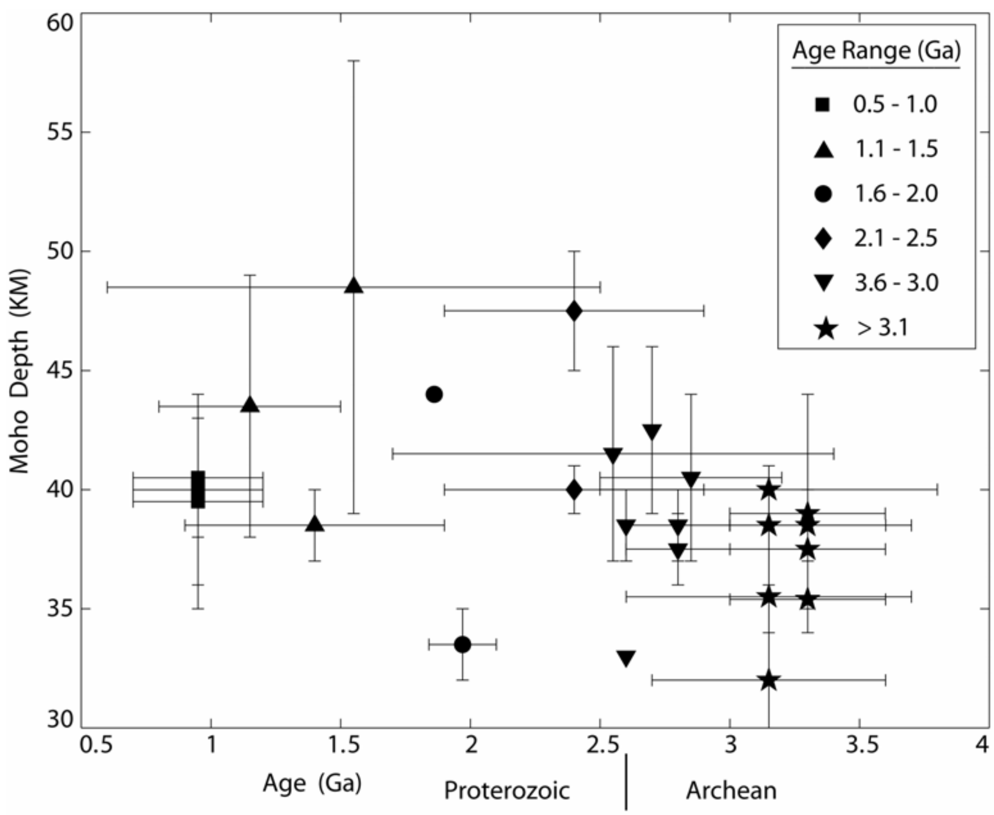

Age Range (Ga)
0.5 - 1.0
1.1 - 1.5
1.6 - 2.0
2.1 - 2.5
3.6 - 3.0
> 3.1
Moho Depth (KM)
60
55
50
45
40
35
30
0.5
1
1.5
2
2.5
3
3.5
4
Age (Ga)
Proterozoic
Archean

relatively dense distribution of observations. The cross section (Figure 2.15b, c) shows a dramatic increase in Moho depth from near the Red Sea coastline to the shield escarpment, after which the change in depth stabilizes and little undulation in the Moho depth can be seen. This dramatic change in crustal thickness occurs over a relatively short distance; for example, the Moho depth at station LTHS along the Red Sea coast (see Figure 2.2 and 2.12) is about 22 km, but at a distance of about 50 km to the east of this station the Moho depth increases to over 40 km.

From the cross section of Figure 2.15, the distance from the Red Sea ridge to the escarpment is about 250 km. The relatively short distance over which the crust changes from oceanic to a typical continental crustal thickness is an important observation. This led us to contrast our observation with a typical Atlantic continental margin. Figure 2.16 clearly shows that the transition from oceanic to continental crust along a typical western Atlantic margin is about 450 km, compared with the observed 250 km along the Red Sea. This suggests that the Red Sea margin is fundamentally different than the Atlantic passive margin. Another speculative scenario is that the observed abruptness of the Red Sea margin is an inherent feature in the rifting process and that over considerable geologic time the abrupt margin evolves into an extended margin.

It is tempting to speculate that the Red Sea opening may be one of the consequences of the presence of a mega plume that extends from the core-mantle boundary into the upper mantle beneath east Africa, the Red Sea, and the western portion of the Arabian plate (Ritsema and van Heijst, 1999; Romanowicz and Gung, 2002). It is possible that this mega plume may have rivaled those that drove the break up of Gondwanaland and Pangea. Based on surface geologic observations and widespread volcanic activity (Camp and Roobol, 1992) it appears that this plume has affected the lithospheric structure over a large distance (> 4000 km) in east Africa and

Figure 2.15. Map and cross-sections showing Moho depth at stations along a profile from the Red Sea to the east coast of Arabia. a) Map showing the location of the profile. b) The cross section without depth exaggeration. c) Same cross section as in (b) with vertical exaggeration. d) Stacked radial receiver functions for distances 70° – 85° for the same stations shown in the cross section (c).

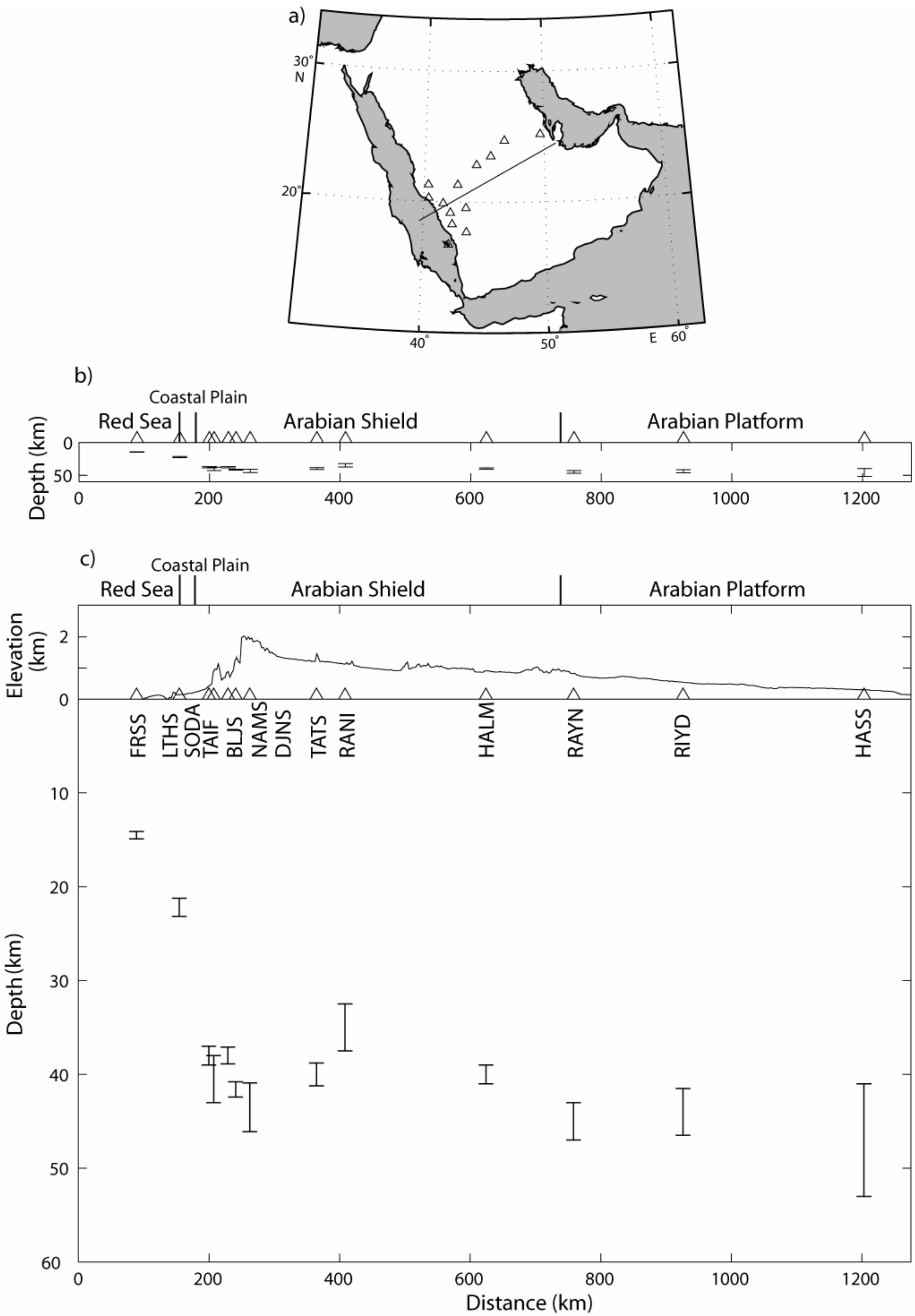
a)
30°
N
20°
40°
50°
E 60°
b)
Coastal Plain
Red Sea
Arabian Shield
Arabian Platform
Depth (km)
0
50
0
200
400
600
800
1000
1200
c)
Coastal Plain
Red Sea
Arabian Shield
Arabian Platform
Elevation (km)
2
1
0
FRSS
LTHS
SODA
TAIF
BLJS
NAMS
DJNS
TATS
RANI
HALM
RAYN
RIYD
HASS
Depth (km)
10
20
30
40
50
60
0
200
400
600
800
1000
1200
Distance (km)

Figure 2.15. (continued)

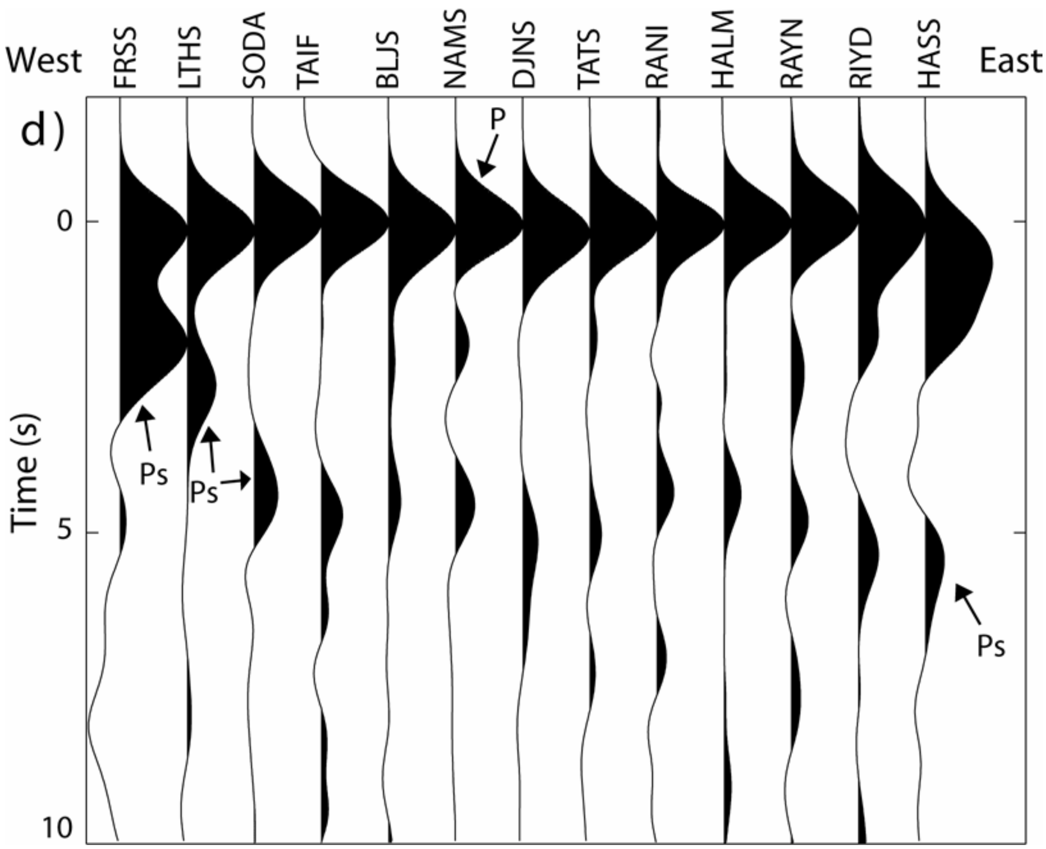

Figure 2.16. A cross section showing the Moho profile contrasting a typical Western Atlantic continental margin (modified from Grow and Sheridan [68]) to the eastern Red Sea margin (based on our results). We used a vertical exaggeration (V.E.) of 200%. The distance between an average continental and oceanic crust in the Red Sea is half of that in the western Atlantic margin. The dotted line is our extrapolation for the oceanic crust.

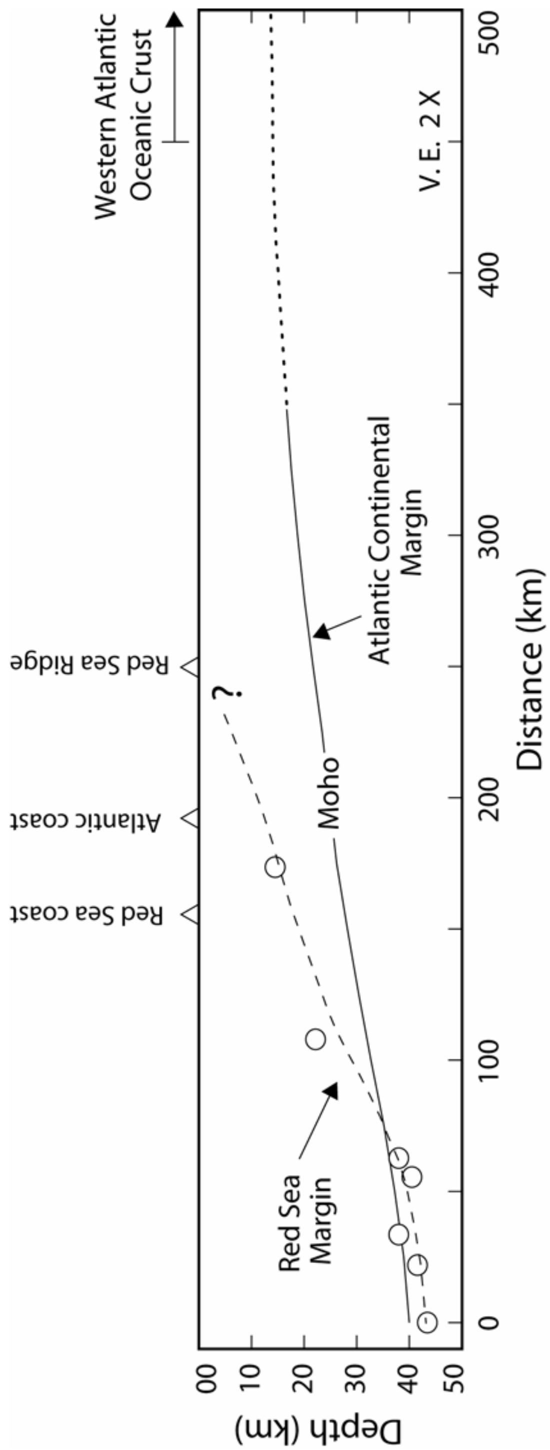
Western Atlantic
Oceanic Crust
V. E. 2 X
Atlantic Continental
Margin
Moho
Red Sea
Margin
?
Red Sea Ridge
Atlantic coast
Red Sea coast
Distance (km)
0
100
200
300
400
500
Depth (km)
00
10
20
30
40
50

western Arabia, and may have resulted in a considerable thinning of the mantle part of the lithosphere. This is partially documented in western Arabia based on the recent tomographic results of high attenuation and low velocity uppermost mantle (Al-Damegh *et al*., 2004; Sandvol *et al*., 2001; Al-Lazki *et al*., 2004). Moreover, the site where the Red Sea sea-floor spreading occurred was a Proterozoic suture and a zone of weakness throughout the lithosphere connecting the proto-Arabian plate and the African plate (Garson and Krs, 1976; Dixon *et al*., 1987). The above observations combined may explain the relatively abrupt breakup of the Arabian plate and the anomalous nature of the Red Sea margin.

ACKNOWLEDGEMENTS

The authors would like to thank King Abdulaziz City for Science and Technology (KACST) for providing us with the digital recordings of the Saudi National Seismic Network and providing a scholarship for the first author. We would like also to thank Lawrence Livermore National Laboratory for providing us with the digital data from stations RUWJ and HITJ. We thank Robert Kay for useful discussions, and C. Sandvol, C. Brindisi, F. Gomez, and S. Gallow for their help in GIS and computer questions. This research is partially supported by the National Science Foundation grants EAR – 9804780 and EAR – 0106238 to Cornell University.

REFERENCES

Al-Amri, A.M., 1999. The crustal and upper-mantle structure of the interior Arabian platform, Geophys. J. Int., **136**, 421-430.

Al-Amri, S.M., and Al-Amri, A.M., 1999. Configuration of the seismographic network in Saudi Arabia, Seismol. Res. Let., **70**, 322-330.

Al-Amri, A.M., and Gahrib, A.A., 2000. Lithospheric seismic structure of the eastern region of the Arabian Peninsula, J. Geody., **29**, 125-139.

AL-Damegh, K., Sandvol, E., Al-Lazki, A., and Barazangi, M., 2004. Regional seismic wave propagation (Lg and Sn) and Pn attenuation in the Arabian plate and surrounding regions, accepted to Geophys. J. Int.

Alinaghi, A., Kind, R., and Bock, G., 2002. Receiver function probing of the crust and the upper mantle underneath north German basin, Scandinavia and the Baltic shields: Evidence of ancient collision zones, AGU abstract.

Al-Lazki, A.I., Seber, D., Sandvol, E., and Barazangi, M., 2002. A crustal transect across the Oman mountains of the eastern margin of Arabia, GeoArabia, **7**, 47-78.

Assumpμção, M., 2002. Crustal thickness in SE Brazilian Shield by receiver function analysis: Implications for isostatic compensation, J. Geophy. Res., **107**, 1-14.

Bank, C.G., Bostock, M.G., Ellis, R.M., and Cassidy, J.F., 2000. A reconnaissance teleseismic study of the upper mantle and transition zone beneath the Archean Slave craton in NW Canada, Tectonophysics, **319**, 151-166.

Benoit, M.H., Nyblade, A.A., VanDecar, J.C., and Gurrola, H., 2003. Upper mantle P wave velocity structure and transition zone thickness beneath the Arabian Shield, Geophys. Res. Lett., **30**, 1-4.

Berzin, R.G., Yurov, Yu.G., and Pavlenkova, N. I., 2002. CDP and DSS data along the Uchta-Kem profile (the Baltic Shield), Tectonophysics, **355**, 187-200.

Brown, G. F., 1972. Tectonic map of the Arabian Peninsula, Saudi Arabian Peninsula Map Ap-2. Saudi Arabian Dir. Gen. Miner. Resour.

Burdick, L.J., and Langston, C.A., 1977. Modeling crustal structure through the use of converted phases in teleseismic body-wave forms, Bull. Geol. Soc. Am., **67**, 677-691.

Camp, V.E., and Roobol, M.J., 1992. Upwelling asthenosphere beneath western Arabia and its regional implications, J. Geophys. Res., **97**, 15255-15271.

Chevrot, S., and van der Hilst, R.D., 2000. The Poisson ratio of the Australian crust: Geologic and geophysical implications, Earth Planet. Sci. Lett., **183**, 121-132.

Clark, M. , and Royden, L., 2000. Topographic ooze: Building the eastern margin of Tibet by lower crustal flow, Geology, **28**, 703-706.

Cochran, J.R, and Martinez, F., 1988. Structure and tectonics of the northern Red Sea: Catching a continental margin between rifting and drifting, Tectonophysics, **150**, 1-32.

Dahl-Jensen, T., Larsen, B., Woelbern, I., Bach, T., Hanka, W., Kind, R., Gregersen, S., Mosegaard, K., Voss, P., and Gudmundsson, O., 2003. Depth to Moho in Greenland: Receiver function analysis suggests two Proterozoic blocks in Greenland, Earth Planet. Sci. Lett., **205**, 379-393.

Daradich, A., Mitrovica, J.X., Pysklywec, R.N., Willett, S.D., and Forte, A.M., 2003. Mantle flow, dynamic topography, and rift-flank uplift of Arabia, Geological Society of America, **31**, 901-904.

Darbyshire, F., 2003. Crustal structure across the Canadian High Arctic region from teleseismic receiver function analysis, Geophys. J. Int., **152**, 372-391.

Debayle, V., Leveque, J., and Cara, M., 2001. Seismic evidence for a deeply rooted low-velocity anomaly in the upper mantle beneath the northeastern Afro/Arabian continent, Earth Planet. Sci. Lett., **193**, 423-436.

Dixon, T.H., Stern, R.J., and Hussein, I.M., 1987. Control of Red Sea rift geometry by Precambrian structures, Tectonics, **6**, 551-571.

Durrheim, R., and Mooney, W., 1991. Archean and Proterozoic crustal evolution: Evidence from crustal seismology, Geology, **19**, 606-609.

Durrheim, R., and Mooney, W., 1994. Evolution of the Precambrian Lithosphere: seismological and geochemical constraints, J. Geophys. Res., **99**, 15359-15374.

Efron, B., and Tibshirani, R., 1991. Statistical analysis in the computer age, Science, **253,** 390-395.

El-Isa, Z.H., Mechie, J., Makris, J., and Rihm, R., 1987. A crustal structure study of Jordan derived from seismic refraction data, Tectonophysics, **138**, 235-253.

Garfunkel, Z., 1981. Internal structure of the Dead Sea leaky transform (rift) in relation to plate kinematics, Tectonophysics, **80,** 81-108.

Garson, M., and KRS, M., 1976. Geophysical and geological evidence of the relationship of Red Sea transverse tectonics to ancient fractures, Bull. Geol. Soc. Am., **87**, 169-181.

Gettings, M., Blank, H., Mooney, W., and Healey, J., 1986.Crustal structure in southwestern Saudi Arabia, J. Geophys. Res., **91**, 6491-6512.

Goodwin, A.M., 1991. Precambrian Geology, Academic Press, New York.

Greenwood, W.R., Anderson, R.E., Fleck, R.J., and Roberts, R.J., 1980. Precambrian eologic history and plate tectonics evolution of the Arabian Shield, Saudi Arabia, Dir. Gen Miner. Resour. Bull. 24-34.

Grow, J.A., and Sheridan, R.E., 1988. U.S. Atlantic continental Margin: A typical Atlantic-type or passive continental margin, in R.E. Sheridan, J.A. Grow (Ed.), The Atlantic Continental Margin: U.S., Geological Society of America, The Geology of North America, pp. 1-7.

Kay, R.W., and S. Kay (1993). Delamination and delamination magmatism, Tectonophysics, **219**, 177-189.

Kennett, B., 1984. Seismic wave propagation in stratified media, Cambridge Univ. Press, New York.

Kumar, M.R., Ramesh, D.S., Saul, J., Sarkar, D., and Kind, R., 2002. Crustal Structure and upper mantle stratigraphy of the Arabian shield, Geophs. Res. Lett., **29,** 1-4.

Kumar, M.R., Saul, J., Sarkar, D., Kind, R., and Shukla, A., 2001. Crustal structure of the Indian shield: New constraints from teleseismic receiver functions, Geophys. Res. Lett., **28**, 1339-1342.

Langston, C.A., 1979. Structure under Mount Rainier, Washington, inferred from teleseismic body waves, J. Geophys. Res., **84**, 4749-4762.

Li, A., Fischer, K., van der Lee, S., and Wysession, M.E., 2002. Crust and upper mantle discontinuity structure beneath eastern North America, J. Geophys. Res., **7**, 1-13.

Ligorria, J.P., and Ammon C.J., 1999. Iterative deconvolution and receiver-function estimation, Bull. Geol. Soc. Am., **89**, 1395-1400.

Makris, M.J., and Rhim, R., 1991. Shear-controlled evolution of the Red Sea: pull-apart model. Tectonophysics, **198**, 441-466.

Meissner, R., 1986. The Continental Crust: A Geophysical Approach, Academic Press, Sand Diego, CA.

Meissner, R., and Wever, T., 1989. Continental crustal structure, in: D.E. James (Ed.), The Encyclopedia of Solid Earth Geophysics, Van Nostrand Reinhold, New York, pp. 75-89.

Midzi, V., and Ottemöller, L., 2001. Receiver function structure beneath three southern Africa seismic broadband stations, Tectonophysics, **339**, 443-454.

Mokhtar, T.A., 1995. Phase velocity of the Arabian Platform and the surface waves attenuation's characteristics by waveform modeling, Journal of King Abul Aziz University, Earth Sci., **8**, 23-45.

Mokhtar, T.A., Ammon, C.A., Herrmann, R.B., and Ghalib, A.A., 2001. Surface wave velocity across Arabia, Pure Appl. Geophys.**158**, 1425-144.

Mooney, W.D., Gettings, M.E., Blank, H.R., and Healy, J.H., 1985. Saudi Arabian seismic-refraction profile: A traveltime interpretation of crustal and upper mantle structure, Tectonophysics, **111**, 173-246.

Nelson, K.D., 1991. A unified view of craton evolution motivated by recent deep seismic reflection and refraction results, Geophys. J. Int., **105**, 25-35.

Nguuri, T.K., Gore, J., James, D.E., Webb, S.J., Wright, C., Zengeni, T.G., Gwavava, O., Snoke, J.A., and Kaapvaal Seismic Group, 2001. Crustal structure beneath southern Africa and its implications for the formation and evolution of the Kaapvaal and Zimbabwe cratons, Geophys. Res. Lett., **28**, 2501-2504.

Niu, F., and James, D., 2002. Fine structure of the lowermost crust beneath the Kaapvaal craton and its implications for crustal formation and evolution, Earth Planet. Sci. Lett., **200**, 121-130.

Nyblade, A.A., Owens, T.J., Gurrola, H., Ritsema, J., and Langston, C.A., 2000. Seismic evidence for a deep upper mantle thermal anomaly beneath east Africa, Geology, **28**, 599-602.

Pavlenkova, G.A., Priestley, K., and Cipar ,J., 2002. 2D model of the crust and uppermost mantle along rift profile Siberian craton, Tectonophysics, **355**, 171-186.

Powers, R.W., Ramirez, L.F., Redmond, C.P., and Elberg, E.L., 1966. Geology of the Arabian Peninsula: Sedimentary geology of Saudi Arabia, U.S. Geol. Surv. Prof. Pap. ,**560-D**, 91-96.

Reading, A.B., and Kennett, B.L.N., 2003. Lithospheric structure of the Pilbara Craton, Capricorn Orogen and northern Yilgran Craton, Western Australia, from teleseismic receiver functions, Austr. J. Earth Sci., **50**, 439-445.

Reading, A.B., Kennett, B.L.N., and Dentith, M.C., 2003. Seismic structure of the Yilgren Carton, Western Australia, Austr. J. Earth Sci., **50,** 427-438.

Ritsema, J., and van Heijst, H.J., 1999. Complex shear wave velocity structure imaged beneath Africa and Iceland, Science, **286**, 1925-1928.

Rodgers, A., Harris, D., Ruppert, S., Lewis, J.P., O'Boyle, J., Pasyanos, M., Abdallah, A.F., Al-Yazjeen, T., Al-Gaso, A., 2003. A broadband seismic deployment in Jordan, Seismol. Res. Lett., **74**, 347-381.

Rodgers, A., Walter, W.R., Mellors, R.J., Al-Amri, A.M., and Zhang, Y, 1999. Lithospheric structure of the Arabian Shield and Platform from complete regional waveform modeling and surface wave group velocities, Geophys. J. Int., **138**, 871-878.

Romanowicz, B., and Gung, Y., 2002. Superplumes from the core-mantle boundary to the lithosphere: Implications for heat flux, Science, **296**, 513-516.

Sandvol, E., Al-Damegh, K., Calvert, A., Seber, D., Barazangi, M., Mohamad, R., Gok, R., Turkelli, N., and Gurbuz, C., 2001. Tomographic imaging of Lg and Sn propagation in the Middle East, Pure appl. Geophys., **158**, 1121-1163.

Sandvol, E., Seber, D., Barazangi, M., Vernon, F., Mellors, R., and Al-Amri, A., 1998b. Lithospheric seismic velocity discontinuities beneath the Arabian Shield, Geophys. Res. Lett., **25**, 2873-2876.

Sandvol, E., Seber, D., Calvert, A., and Barazangi, M., 1998a. Grid search modeling of receiver functions: Implications for crustal structure in the Middle Eat and North Africa, J. Geophys. Res., **103**, 26899-26917.

Sarkar, D., Chandrakala, K., Padmavathi, P., Sridhar, A.R., Sain, K., 2001. Crustal velocity structure of western Dharwar Craton, South India, J. of Geodyn., **31,** 227-241.

Seber, D., and Mitchell, B., 1992. Attenuation of surface waves across the Arabian Peninsula, Tectonophysics, **204**, 137-150.

Seber, D., Vallve, M., Sandvol, E., Steer, D., and Barazangi, M., 1997. Middle East tectonics: Applications of geographic information system (GIS), GSA Today, **7**, 1-6.

Stankiewicz, J., Chevrot, S., van der Hilst, R., and de Wit, M., 2003. Crustal thickness, discontinuity depth, and upper mantle structure beneath southern Africa: Constraints from body wave conversions, Phys. Earth Planet. Inter., **130**, 235-251.

Tichelaar, B., and Ruff, L., 1989. How good are our best models? Jackknifing, bootstrapping, and earthquake depth, Eos Trans. AGU, **70**, 605-606.

Viejo, G.F., and Clowes, R.W., 2003. Lithospheric structure beneath the Archaean Slave province and Proterozoic Wopmay orogen, northwestern Canada, from a

LITHOPROBE refraction/wide-angle reflection survey, Geophys. J. Int., **153**, 1-19.

Zhu, I., and Kanamori, H., 2000. Moho depth variation in southern California from teleseismic receiver functions, J. Geophys. Res., **105**, 2969-2980.

Zor, E., Sandvol, E., Gürbüz, C., Türkelli, N., Seber, D., and Barazangi, M, 2003. The crustal structure of the East Anatolian plateau (Turkey) from receiver functions, Geophys. Res. Lett., **30**, 8044.